

CZECH UNIVERSITY OF LIFE SCIENCES PRAGUE

Faculty of Tropical AgriSciences



**Faculty of Tropical
AgriSciences**

**The Assimilation of Synthetic Aperture Radar Satellite Data
into the Simulation of Crop Model**

DISSERTATION THESIS

Prague 2022

Author: Ing. Lukáš Tůma
Chief supervisor: doc. Ing. Vladimír Krepl, CSc.
Second (specialist) supervisor: doc. Ing. Bc. Tatiana Ivanova, Ph.D.

Declaration

I Lukáš Tůma hereby declare that I have written this thesis entitled “The Assimilation of Synthetic Aperture Radar Satellite Data into the Simulation of Crop Model” on my own, all texts in this thesis are original, and all the sources have been quoted and acknowledged by means of complete references and according to Citation rules of the FTA.

In Prague January 7th 2022

.....

Lukáš Tůma

Acknowledgments

I would like to thank all people helping me during the research, thesis writing, and through my Ph.D. study.

Firstly, I would like to express my deep gratitude to my supervisor doc. Ing. Vladimír Krepl, CSc. for his patience, significant help, and guidance throughout my study. Without his academic support, it would be very difficult to finish my studies.

Special thanks go to doc. Ing. Bc. Tatiana Ivanova, Ph.D. for her kindness, management of my research, recommendations, and encouragement.

My gratitude also belongs to Mgr. Pavel Juruš, Ph.D. from the Institute of Computer Science of The Czech Academy of Sciences for his technical advice, support, and consultation of the used research methods.

Special thanks also go to doc. Mgr. Jitka Kumhálová, Ph.D. and prof. Dr. Ing. František Kumhála from Faculty of Engineering CZU for the opportunity to work with them during the research activities and their irreplaceable technical advice and support.

I am grateful to Taher Kahil, the Research Group Leader and Research Scholar in the International Institute for Applied Systems Analysis in Austria that he provided me an opportunity to work with great scientists of this institute during my internship in the scope of Erasmus Traineeship.

Finally, I express gratitude to my family, especially to my parents, who were patient with me during the whole Ph.D. studies and supported me in each of my academic aims.

This research was supported by the Internal Grant Agency of the Faculty of Tropical AgriSciences, Czech University of Life Sciences Prague [grant numbers 20205012 and 20213108].

Abstract

The crop growth modelling represents an important tool for researchers investigating environmental processes and food security issues. The WO^rld FO^od Studies (WOFOST) simulation model was used to examine crop growth frequently. One development pathway of crop modelling is data assimilation (DA). This method is used for decreasing the uncertainty of models by updating them with data obtained from observations. Sentinel-1 SAR satellite provides radar data able to monitor environmental processes with high frequency; however, its usage was so far limited in DA methods.

Wheat fields of an agricultural cooperative in the Czech Republic were investigated between 2015 and 2019. In order to increase the accuracy of winter wheat forecasting by the WOFOST, this research tried to utilize Sentinel-1 (S1) data jointly with Sentinel-2 (S2) for Ensemble Kalman Filter (EnKF). The relation between Normalized Difference Vegetation Index (NDVI) and Radar Vegetation Index (RVI) timeseries was established by examination of different Sentinel-1's Relative orbits and platforms used during the analysis. The temporal development of RVI was heavily affected by noise caused by monitoring from different Relative orbits and platforms. Using imagery according to the Relative orbit provided results more like the phenological curve. Linear regression between NDVI and single Relative orbit use of RVI slightly increased the goodness of fit. The best correlation between RVI and NDVI was 0.39. The RVI data was cleaned by Savitzky-Golay (S-G) filter. The Leaf Area Index (LAI) was estimated from S2 data. The correlation between LAI and RVI was 0.69. The Random Forest Regression (RFR) was trained between the S1 RVI and S2 LAI, and radar LAI (R-LAI) was predicted. The measured model fit accuracy was 0.52. Finally, The WOFOST model was runned open-loop, with EnKF S2 LAI DA and EnKF S1 R-LAI DA with root mean square results (RMSE) of 4.23, 3.43, and 3.66 t.ha⁻¹. The mean absolute error was then 3.79, 3.07, and 3.31 t.ha⁻¹. The research results demonstrated that S1 DA to WOFOST can increase the accuracy of the model, however not so much as S2 optical data does. More research needs to be conducted in the S1 LAI data prediction and assimilation.

Key words: crop modelling, simulation, forecasting, remote sensing, satellite data, Sentinel-1 Sentinel-2, biomass, yield, data assimilation, crop, wheat

Table of contents

1. Introduction	1
2. Literature review	4
2.1 Crop modelling	4
2.2 The WOFOST	9
2.2.1 Introduction to the WOFOST modelling	9
2.2.2 The WOFOST simulation processes	11
2.2.3 The WOFOST input/output data and calibration	16
2.2.4 Python Crop Simulation Environment	17
2.2.5 Research activities and practical use of the WOFOST	18
2.3 Remote Sensing	22
2.3.1 Optical Vegetation Indices	23
2.3.2 Radar Vegetation Index	24
2.4 Assimilation of remotely sensed data	27
3. Aims of the thesis	32
4. Hypotheses / Research questions	33
4.1 Hypothesis 1	33
4.2 Hypothesis 2	33
5. Methodology	34
5.1 Fields and Data	34
5.1.1 Research sites	34
5.1.2 Wheat fields monitoring and measurements	35
5.1.3 Remote sensing data	40
5.1.4 Climate data	43
5.1.5 Soil data	44
5.2 Remote sensing data processing and analysis	46
5.2.1 Sentinel-2 data processing and analysis	46
5.2.2 Sentinel-1 data processing and analysis	48
5.3 Machine learning prediction of Leaf Area Index	50
5.3.1 Preparation of data	50
5.3.2 Random Forest Regression	51
5.4 WOFOST - Crop growth modelling	54
5.4.1 Calibration and run of crop growth model	54
5.4.2 Assimilation of satellite data to the WOFOST	56
5.5 Statistical assessment of crop modelling accuracy	59
5.6 Software and data processing tools	60

6. Results and Discussion	62
6.1 NDVI and RVI results.....	62
6.1.1 NDVI results	62
6.1.2 RVI results	63
6.1.3 Correlation of Radar Vegetation Index with Normalized Difference Vegetation Index	68
6.2 Radar Vegetation Index filtering and adjustment	69
6.3 Leaf Area Index estimation from Sentinel-2.....	76
6.4 Leaf Area Index prediction from Sentinel-1 by Machine Learning.....	80
6.4.1 Data composition	80
6.4.2 Random Forest Regression – results	82
6.5 Wheat – crop growth modelling.....	84
6.6 Assimilation of satellite data into the crop model.....	88
6.6.1 Ensemble Kalman Filter – Sentinel-2’s Leaf Area Index assimilation	88
6.6.2 Ensemble Kalman Filter – Sentinel-1’s Leaf Area Index assimilation	92
6.6.3 Final evaluation and discussion of data assimilation methods.....	95
7. Conclusions	100
8. Recommendations for further research	102
9. References	104
10. Author Bibliography.....	133
11. Annex.....	I

List of Figures

Figure 1. Descriptive, mechanistic and statistical approach for crop growth modelling. (Source: Vazquez et al. 2010; Basso et al. 2013)	5
Figure 2. Theoretical production levels. (Source: van Ittersum & Rabbinge 1997)	8
Figure 3. Time development of main crop models. (Source: Jin et al. 2018)	9
Figure 4. Overview of the WOFOST main processes and their relations. (Source: de Wit et al. 2018)	12
Figure 5. Variable block and their minimum sums of weighting points required for each quality class. (Source: Kersebaum et al. 2015)	17
Figure 6. PCSE programming workflow in Visual Studio Code.	18
Figure 7. MARS-Crop Yield Forecasting System workflow. (Source: van der Velde et al. 2018)	20
Figure 8. Sentinel-1 (left) and Sentinel-2 (right). (Source: Copernicus Not dated - c; AIRBUS 2020)	23
Figure 9. MARS-Crop Yield Forecasting System workflow. (Source: Yamaguchi et al. 2021)	24
Figure 10. The ComRAD Microwave Instrument System – measuring the RVI. (Source: Srivastava et al. 2015).....	26
Figure 11. Schematic for assimilation of remote sensing data into crop models. (Source: Pan et al. 2017).....	28
Figure 12. Main elements of data assimilation. (Source: Tupin et al. 2014)	30
Figure 13. Location of the Research area and Relative orbits over the area. (Source: Tůma et al. 2021)	35
Figure 14. Cultivated wheat fields in main vegetation seasons (2015/2016, 2016/2017, 2017/2018 and 2018/2019) with Field ID	37
Figure 15. Wheat field; year 2017, Field ID - 5	40
Figure 16. The European Community medium soil's (EC2-medium) parameters.....	46
Figure 17. Sentinel-1 Ground Range Detected (GRD) pre-processing and processing workflow. (Source: adjusted from Filipponi 2019)	48
Figure 18. Final structure of dataframe; Tail of data; Shapefile is unique ID for wheat field, date of record is date of Sentinel-2 monitoring.....	51
Figure 19. EnKF data assimilation – general overview.	59
Figure 20. Normalized difference vegetation indices for investigated wheat fields throughout the 2015 – 2018 growing seasons. (Source: Tůma et al. 2021).....	63
Figure 21. Radar Vegetation Index visualization of monitored wheat (red) fields and its graininess – a) 5.5.2016; b) 3.5.2017; c) 2.5.2018; d) 2.5.2019; Different relative orbits; white – high values, black – low values.....	65

Figure 22. The average Radar Vegetation Indices for monitored rapeseed and wheat fields throughout the 2015 – 2019 vegetation seasons (Source: adjusted from Tůma et al. 2021).....	66
Figure 23. Illustrative timeseries of wheat RVI for field 1 through the vegetation seasons of 2015 – 2018. The dash line represents images from all Relative orbits (22; 73; 124), while the dotted-dash line shows only results from Relative orbit 22. The full line considers only Relative orbit 22 for the Sentinel-1 platform A. (Source: Tůma et al. 2021).....	67
Figure 24. Scatterplots of RVI and NDVI for wheat with simple Linear regression and R-squared. Comparison of all data used, single platform and Relative orbit used. (Source: Tůma et al. 2021).....	68
Figure 25. Average RVI unfiltered (left) and filtered (right) values (2016 -2019) – development through vegetation season; basic interpolation (red line).....	70
Figure 26. Histogram for RVI values – year 2019; unfiltered values.	72
Figure 27. Histogram for RVI values – year 2019; unfiltered values.	73
Figure 28. Comparison of five RVI images from season 2019 (3.3.2019, 2.4.2019, 2.5.2019, 1.6.2019 and 1.7.2019) before the filtering (left) and after the Savitzky–Golay filtering (right); Wheat fields 1, 2, 3.	75
Figure 29. Visualization of LAI products (2016 -2019); wheat fields – red delineation; a) 27.3.2016, b) 1.4.2017, c) 31.5.2018, d) 1.5.2019.	77
Figure 30. LAI development through vegetation season (2016 – 2019); Wheat fields – mean; basic interpolation (red line).	78
Figure 31. Histogram – wheat’s LAI [$m^2.m^{-2}$]; vegetation seasons (2016 – 2019).....	79
Figure 32. Scatterplots of annual RVI and LAI values for wheat (2016 – 2019); blue – March, green – April, yellow – May, orange – June, red – July.	82
Figure 33. Line charts of R-LAI results for years 2016 – 2019 with single wheat field development.	84
Figure 34. Final yield for wheat growth modelling (2015 – 2019).....	87
Figure 35. LAI development, simulation of WOFOST (2015 – 2019).....	88
Figure 36. LAI development, Wheat field ID 1; Model Ensemble (transparent lines), Model Ensemble Mean (red line), LAI observations from Sentinel-2 with 10 % error (black circles)..	90
Figure 37. Final yield for wheat growth modelling after the LAI data assimilation from Sentinel-2 (2015 – 2019).....	91
Figure 38. LAI development, Wheat field ID 1; Model Ensemble (transparent lines), Model Ensemble Mean (red line), LAI observations from Sentinel-1 with 20 % error (black circles)..	93
Figure 39. Final yield for wheat growth modelling after the LAI data assimilation from Sentinel-1 (2015 – 2019).....	94

List of Tables

Table 1. Overview of Research area and Satellite images scenes (Source: Tuma et al. 2021) ...	35
Table 2. Vegetation season 2015/2016 - Overview of wheat fields; variety; area and average yield.....	37
Table 3. Vegetation season 2016/2017 - Overview of wheat fields; variety; area and average yield.....	38
Table 4. Vegetation season 2017/2018 - Overview of wheat fields; variety; area and average yield.....	38
Table 5. Vegetation season 2018/2019 - Overview of wheat fields; variety; area and average yield.....	39
Table 6. Sentinel-2 band characteristics – resolution and spectral bands. (Source: ESA 2015).	42
Table 7. Weather input data for the WOFOST model. (Source: Kraalingen et al. 1997)	44
Table 8. Overview of used vegetation indices in this study. (Source: adjusted from Tuma et al. 2021)	49
Table 9. Randomized search and Grid search for optimal hyperparameters of the Random Forest Regression	53
Table 10. WOFOST’s crop specific parameter values used for calibration.....	55
Table 11. WOFOST’s structure of daily outcomes from crop simulation.	56
Table 12. Linear regression results for NDVI and RVI values of observed wheat fields. Different Relative orbit utilization; Platform A.	69
Table 13. Match tables for finding the closest Sentinel-1 and Sentinel-2 dates of observations.	80
Table 14. 2016 - Comparison of observed yield, crop modelling and crop modelling with EnKF assimilation methods.	96
Table 15. 2017 - Comparison of observed yield, crop modelling and crop modelling with EnKF assimilation methods.	96
Table 16. 2018 - Comparison of observed yield, crop modelling and crop modelling with EnKF assimilation methods.	97
Table 17. 2019 - Comparison of observed yield, crop modelling and crop modelling with EnKF assimilation methods.	97
Table 18. RMSE and MAE for observed yield and crop modelling methods.....	98

List of the abbreviations used in the thesis

3DVAR - Three-Dimensional Variational Data Assimilation

4DVAR - Four-Dimensional Variational Data Assimilation

° - Degree

°C - Degrees Celsius

θ_t - Actual moisture content of the root zone at time step t

Δt - Time step

ARD - Increase of the rooting depth

ΔW - Growth rate

ΔW_i - Dry matter growth rate of organ i

ΔW_{nlv} - Net dry matter growth of leaves at time step t

ΔW_{rt} - Dry matter growth rate for roots

ΔW_{sh} - Dry matter growth rate to shoots

δSS_t - Surface storage

μm – Micrometer

σ^0 - Sigma nought backscatter

AFGEN - Arbitrary Function GENERator

API - Application programming interface

ANN - Artificial neural networks

ARVI - Atmospherically Resistant Vegetation Index

BACROS - BAsic CROp growth Simulator

BBCH - Biologische Bundesanstalt, Bundessortenamt and Chemical industry

BOA - Bottom-Of-Atmosphere

CDS - Copernicus' Climate Data Store

CFET - Crop coefficient (correction factor)

CGMS - Crop Growth Monitoring System

CpRVI - Compact polarimetric Radar Vegetation Index

cm – Centimetres

cm³.cm⁻³ - Centimer per centimeter

cm.d⁻¹ - Centimeters per day

CR - Rate of capillary rise

CSV - Comma-separated values

CWSI - Crop Water Stress Index

d – Day

DpRVI - Dual-pol Radar Vegetation Index

DPSVI - Dual Polarization SAR Vegetation Index

DVI - Difference Vegetation Index

DVR - Daily development rate

E0_s - Potential bare soil evaporation

E0_w - Potential evaporation rate from a water surface

EC - European Community

ELCROS - ELementary CROp simulator

EnKF - Ensemble Kalman Filter

ESA - European Space Agency

E_s - Soil evaporation rate

E_{s,max} - Maximum evaporation of a bare soil

$E_{w,max}$ - Maximum evaporation of a water surface

ET₀ - Reference crop evapotranspiration rate

ET_c - Evapotranspiration rate of a cropped field

FAO - Food and Agriculture organization

FLAASH - Fast Line-of-Sight Atmospheric Analysis of Hypercubes

GDAL - Geospatial Data Abstraction Library

GIS - Geographic Information System

GRD - Ground Range Detected Interferometric

GRVI - Generalized volume scattering model-based Radar Vegetation Index

h – Hours

ha – Hectare

ha.ha⁻¹.d⁻¹ - Hectare per hectare per day

HBM - Hierarchical Bayesian Method

I_e - Effective daily irrigation

IN_{low} - Rate of net influx through the lower root zone boundary

IN_{up} - Rate of net influx through the upper root zone boundary

ISRIC - International Soil Reference and Information Centre

IW - Wide mode

KF - Kalman Filter

K_{gb} - Rxtinction coefficient for global radiation

kg.ha⁻¹ - Kilograms per hectares

kg.ha⁻¹.d⁻¹ - Kilograms per hectare per day

kg.m⁻² – Kilograms per square meters

kJ.m⁻².d⁻¹ - Kilojoule per square meter per day

kPa - Kilopascal

LAI - Leaf Area Index

L_{Exp,t} - Growth rate of the leaf area index at time step t

LIDAR - Light Detection and Ranging

L_{Sc,t} - Growth rate of the leaf area index at time step t

LAI_t - Leaf area index at time step t

LUT - Look-Up Table

m².m⁻² - Square meters per square meters

m – Meters

MAE - Mean absolute error

MARS - monitoring Agriculture with Remote Sensing

MCYFS - MARS Crop Yield Forecasting System

MERRA-2 - Modern Era Retrospective-Analysis for Research and Applications

mm – millimeters

mm.d⁻¹ - millimeters per day

m.s⁻¹ - meters per second

MODIS - Moderate Resolution Imaging Spectroradiometer

NDVI - Normalized Difference Vegetation Index

NDWI - Normalized Difference Water Index

NPK - Nitrogen, phosphorus and potassium

NumPy - Numerical Python

P - precipitation rate

PF - Particle Filter

pc_i - partitioning factor of organ i

pc_{rt} - partitioning factor of roots

PCSE - Python Crop Simulation Environment

Perc - percolation rate

PRI - Photochemical Reflectance Index

PRVI - Polarimetric radar vegetation index

PVI - Perpendicular Vegetation Index

R-LAI - Predicted Leaf Area Index from Radar Vegetation Index

RD - Actual rooting depth

RDMSOL - Maximum soil rootable depth

RD_t - Rooting depth at time step t

RF - Random forest

RFR - Random Forest Regression

RGB - Red green blue

RGRLAI - Maximum relative increase in leaf area index

RL - Maximum relative increase of leaf area index and it is a function of effective temperature

RMSE - Root mean square error

RR_{max} - Maximum daily increase in rooting depth

RVI - Radar Vegetation Index

RVI 2 - Ratio Vegetation Index

S1 - Sentinel-1

S2 - Sentinel-2

SAR - Synthetic-aperture radar

SAVI - Soil-Adjusted Vegetation Index

SciHub - Copernicus Open Access Hub

SciPy - Scientific Python

S-G - Savitzky-Golay

S_{la} - Specific leaf area at time step t

SMAP - Soil Moisture Active Passive

SMFCF - Field capacity of the soil

SPAN - Life span of leaves growing at an average temperature of 35 °C

SR - Fate of surface runoff

SUCROS - Simple and Universal CROp growth Simulator

SVM - Support vector machines

t.ha⁻¹ – Tonnes per hectare

T_a - Actual transpiration rate of crop

TAGP - Total above-ground production

TBASE - Lower threshold temperature for physiological ageing of leaves

T_e - Daily effective temperature

TDWI - Initial total crop dry weight

T_{max} - Maximum crop transpiration rate

TOC - Top of canopy reflectances

TWSO - Total dry weight of storage organs

UAV - Unmanned Aerial Vehicle

VH - Vertical Horizontal

VV - Vertical Vertical

VS - Vegetation season

VWC - Vegetation water content

WAV - Initial soil water content

WOFOST - WOrld FOod Studies

ZD Vendolí - Vendolí agricultural
cooperative

1. Introduction

The modelling of crop growth and yield forecasting has become an important concern of many scientists involved in Food security and environmental degradation debates. To face the issues of sustainable agriculture, the development of different crop models took place. These modelling approaches can simulate short to long time crop growth development and status according to growth environment for different regions, plants, and management (Di Paola et al. 2015; Jin et al. 2018). There are various types of crop models, but mostly applied are mechanistic models, which attempt to describe relations between parameters and simulated variables, but also the mechanism of processes (Palosuo et al. 2011). Such one of up-to-date models is the WOFOST (WOrld FOod Studies) from the Dutch 'school of de Wit', which has produced many other models (e.g., BACROS; SUCROS, MACROS, LINTUL, and ORYZA). The WOFOST model is widely used around the world, and it has been implemented into MARS crop yield forecasting system, which is used for crop monitoring and yield forecasting activities in Europe. The WOFOST is originally written in programming language called FORTRAN, but there is also a version written in Python language and included in PCSE (Python Crop Simulation Environment) (Bouman et al. 1996; European Commission 2021; Jin et al. 2018; Wit A. 2018). The models like the WOFOST enable crop growth simulations of various crops under different conditions and on a different scale, but spatial variation can cause large errors in simulations and crop yield estimations, especially when inputs like soil moisture, nitrogen content, or meteorological data are uncertain. However, the quite rapid development of remote sensing technologies offers new possibilities in these issues and the potential for more accurate and reliable crop modelling (Jin et al., 2018).

Remote sensing for vegetation canopies analysis started rising in 1960's, and after the launch of the first LANDSAT mission in 1972, the Normalized Difference Vegetation Index (NDVI) was introduced into the field of vegetation monitoring and categorization. It became the most observable satellite metric for photosynthetic activity and plant cover on the Earth. Since then, many indices and algorithms have been introduced for study of the Earth's surface (IJAE OG 2015; Deepak 2015). One of the most essential indices became the Leaf Area Index (LAI) due to its ability to determine the total one-sided leaf area per ground surface area. It governs canopy processes and is related to crucial variables such as chlorophyll content, photosynthesis rate, transpiration,

evapotranspiration, and dry matter accumulation. Therefore, LAI is the key indicator for potential grain yield (Darvishzadeh et al. 2008; Gupta et al. 2000, Herrmann et al. 2011; Huang et al. 2016 - a). There are multiple methods to determine LAI; however, two main categories are recognized - direct and indirect LAI measurements. While in situ research consists of both direct and indirect measurements (e.g., leaf collection by harvesting; non-harvesting litter traps; indirect contact or non-contact LAI measurement methods - Plant Canopy Analyzer), remote sensing consists only of indirect measurement methods by passive or active sensors. Passive sensors are utilized to measure LAI whether it is used an airborne or satellite multispectral/hyperspectral camera, and several methods of determination have been proposed. Also, extensive work has been done on the usage of airborne-based active sensors called Light Detection and Ranging (LIDAR) in the forestry sector. On the other hand, the usage of satellite-based LIDAR sensors in LAI measurements is not yet so explored due to its limited availability. However active sensor called Synthetic-aperture radar (SAR) has already been successfully used for LAI estimation (e.g., for sugar beet, maize, and winter wheat). It can be expected that with the rapid development of radar satellites (ENVISAT, Sentinel-1, ALOS, ALOS-2, RADARSAT-2, TERRASAR-X, and COSMO), more opportunities to estimate crop canopy variables or soil properties will arise (Jin et al. 2018; Zheng & Moskal 2009; Jonckheere et al. 2004; Weiss et al. 2004; Beriaux et al. 2011; Tao et al. 2016; Stankevich et al. 2017; NASA 2020). This development in SAR remote sensing is promising and provides new possibilities for SAR data assimilation into crop models.

One solution, in order to improve crop modelling and avert large errors, is the assimilation of biophysical variables (obtained from remote sensing data) into crop models. There are three distinguishable assimilation strategies: calibration, forcing, and updating method. While the calibration method tries to find optimal consistency between remote sensing data and simulated data of crop model, the forcing method replaces the simulated data of crop model with the remote sensing data. On the other hand, updating method sequentially updates simulated data of crop model within growing season based on remote sensing data and improves the accuracy of the simulation data at succeeding days. The most utilized variable in data assimilation of remote sensing and crop models seems to be LAI. So far, there is a great deal of works based on data assimilation from optical satellites into crop models, but nearly no research works exploring possibilities of SAR data

assimilation into crop models (Jin et al. 2018; Silvestro et al. 2017; Huang et al. 2016 - a). Hence, the purpose of this research is to provide new insight into this actual topic and find possibilities for SAR data utilization in the crop modelling.

2. Literature review

2.1 Crop modelling

The crop modelling nowadays represents a significant tool for monitoring food security and environmental processes under the needs of growing population and pressure of sustainable agriculture and climate change. It has been considerably developed during the last four decades from the easy simulation of crop growth to a complex quantitative simulation of the growth process. And although models cannot simulate all the bio-physical processes, it is important for well-timed estimation of crop yields at a different scale, for different crop management and weather conditions. This has prime importance for government agencies, commodity companies, farmers, or scientific communities in the process of decision making and management of agricultural lands, the establishment of food prices and trading policies, or estimation of production volumes. (Di Paola et al. 2015; Jin et al. 2018; Curnel et al. 2011).

The models can be divided according to their complexity or group and type. The level of complexity is determined by the purpose of crop models, and it ranges from simple models mostly used for yield estimation for larger areas based on statistical information with combination of climate and historical data of yields, to more complex mechanistic models providing explanations of interactions between soil, plant and atmosphere. Another classification divide crop models into two groups – deterministic and stochastic. While the first one produces a result for a given set of conditions, assuming uniformity of input data, the second one – stochastic produces results that take into account uncertainty arising from the variability of input data (e.g., spatial variability). The crop growth systems are generally more stochastic because of heterogeneity; however, this approach has not been developed for operational use, unlike the deterministic approach. Models using the determinist approach can be distinguished into three types of models – Statistical, Mechanistic, and Functional (or descriptive) model as shown in **Figure 1**. (Basso & Liu 2018; Basso et al. 2013; Vazques-Cruz et al. 2010).

Statistical models (or sometimes empirical) were the first models used for large-scale yield simulations. They usually use historical data about crop yields and simplified measurements of weather (e.g., average temperature and precipitation) to calibrate

regression equations. This is a common alternative approach to process-based models, which requires crop parameters of cultivar, soil conditions, and management as input data.

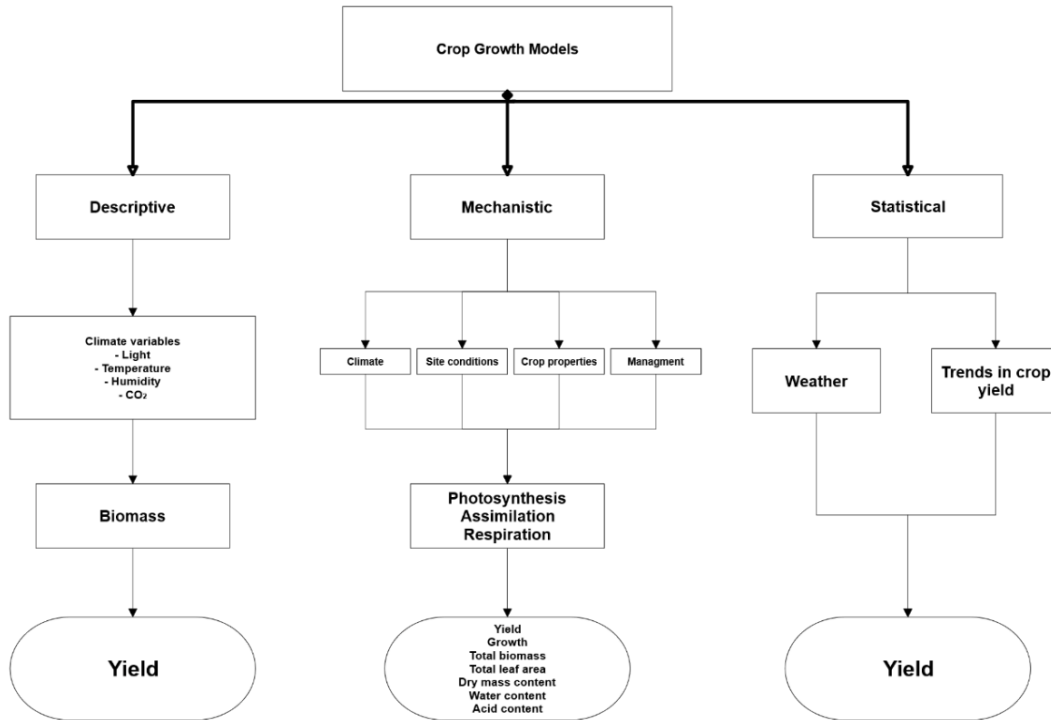


Figure 1. Descriptive, mechanistic and statistical approach for crop growth modelling.
(Source: Vazquez et al. 2010; Basso et al. 2013)

According to Lobell & Burke (2010), three types of statistical models can be distinguished: firstly, models based on timeseries data from a single point or area (timeseries method); secondly, those models based on spatial variability (panel method); and finally, models based on space and time variability (cross-section methods). Every type has different advantages. While Timeseries models can more easily describe the behavior of inspected area, panel and cross-section methods have to assume the same parameter values for all chosen locations. Nevertheless, Timeseries models are sometimes limited by data, whereas panel and cross-section statistical models can combine data from multiple research sites. The main advantage of statistical models seems to be their low dependence on local input (calibration data); on the other hand, these models suffer from co-linearity issues (Basso & Liu 2018; Basso et al. 2013; Lobell & Burke 2010; Wenjiao et al. 2013). The diverse approaches can be found in the literature. Manjunath et al. (2010) used the precipitation values and normalized difference vegetation index (NDVI) in the

statistical multiple linear regression to forecast the wheat yields in various locations in India. Qian et al. (2009) used a similar approach, which applied daily water use and soil water contents for empirical linear regression for yield forecasting. A yield regression model with Vegetation Index timeseries and Historic Crop Statistics was used by Dempewolf et al. (2014) for wheat yield forecasting. Recently, Nagy et al. (2018) regressed the wheat and maize yields from MODIS NDVI and gathered yield values. Many other authors employed the statistics based on remote sensing data or some other data source – Standardized precipitation index, the combination of temperature and precipitation or minimum and maximum temperatures with relative humidity (Quader et al. 2018; Raja et al. 2014; Guo & Xue 2014; Galaktionov et al. 2009; Ayyoob & Krishnadas 2013). More reviews of statistical modelling of yields can be found in Basso & Liu (2018).

Descriptive models, sometimes called **hybrid, functional** or **semi-mechanistic**, are models using simplified mechanisms to describe complex processes. These models are not time-consuming and use only a few state variables to describe relationships between them and response, usually in the form of total biomass and economic yield. These models apply much less input data, and they are comprehensible for those who are not familiar with biophysical processes. The underlying processes are more related to curve fitting and regression; however, these models can simulate aspects of plant functions such as resource acquisition, growth, and its limitations or storage, allocation, and suppression, or phenological changes such as triggering of fruiting (Basso et al. 2013; Renton et al. 2005; Vazquez-Cruz et al. 2010). Domijan et al. (2006) presented the semi-mechanistic model for yield forecasting via estimates of potential yields and the sum of squares. The Mirschel et al. (2004) used a plant-physiology based model with the aid of artificial neural networks models to predict above-ground biomass.

The last and the most complex type of crop modelling is the **mechanistic** approach (or process-oriented). This approach uses fundamental mechanisms of plant-soil-atmosphere such as photosynthesis, assimilation of CO₂, or respiration. These models thoroughly describe processes of plant development, light interception, CO₂ assimilation, respiration, or development of plant organs and their growth with a focus on one or more biophysical components. Mechanistic models are able to run the simulation of crop growth and rates of plant processes in short time intervals and reflect quick-time changes during the day,

such as photosynthetic and transpiration processes related to the radiation and temperature conditions. However, such a high level of simulation details is dearly paid for by the required large amount of input data. Primarily, weather conditions like minimum and maximum temperatures, solar radiation, wind speed, actual water pressure, and precipitation are needed, but also parameters of phenological stages of chosen crops or soil conditions are required for more accurate measurements. Moreover, the estimations of crop growth are related to large uncertainties regarding the spatial variation of soil properties, but also meteorological data, management practices, and crop parameters. Overall, this level of detail is increasing model complexity, and calculation time of software; however development in computer science and programming language are offering new possibilities in the level of detail and shortened calculation time (Basso et al. 2013; Curnel et al. 2011; Di Paola et al. 2015; Vazquez-Cruz et al. 2010). Despite the fact that the mechanistic approach can provide diverse outputs, its main purpose remains in crop yield estimation, which can reach different levels of potential, attainable or actual yield, as can be seen in **Figure 2**. These levels can be distinguished by growth-defining, growth-limiting, and growth-reducing factors. The first factors determine potential growth and potential volume of production by combining optimum of all-important inputs such as the plant parameters, temperature, solar radiation, season, and time of growing. Second factors – limiting factors are composed of water and nutrients factors, which are important abiotic resources. Limiting factors are reducing potential yield and growth from the potential of crops. The third group of factors – reducing attainable yield to actual yield by biotic problems such as weeds, diseases or pests; and by abiotic factors such as pollutants. Most models can simulate crop growth in the following levels of production: potential production; water-limited production, and nutrient-limited production; however they can also differ by estimation of the final obtained yield. Some models estimate yield according to total above-ground biomass; some models by harvest index and others by allocation of assimilated resources during the reproduction phase (van Ittersum & Rabbinge 1997; Pohanková 2016).

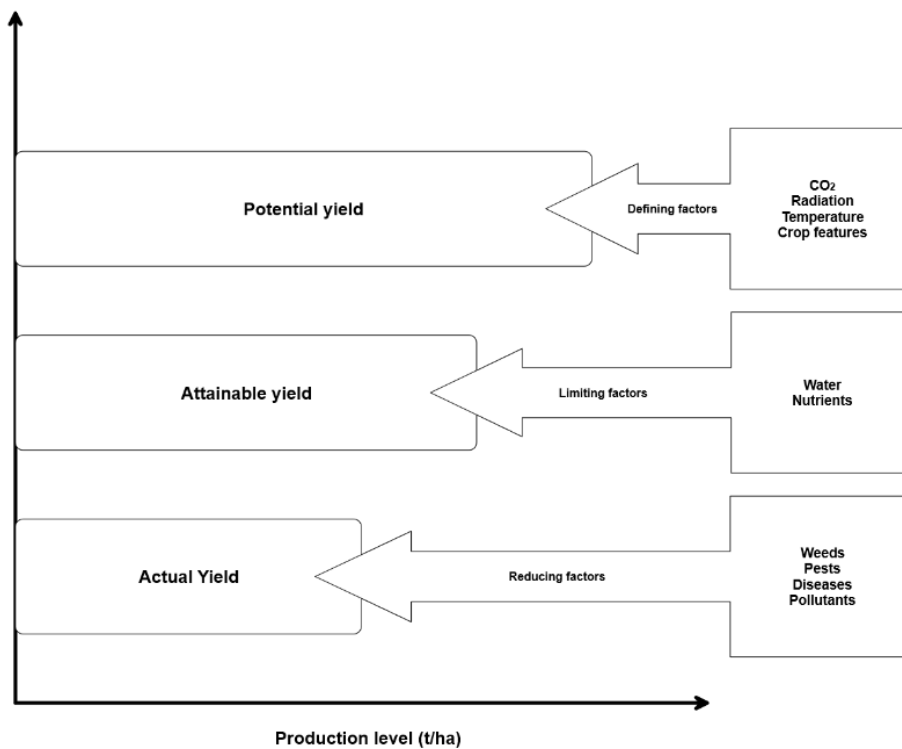


Figure 2. Theoretical production levels. (Source: van Ittersum & Rabbinge 1997)

Due to the focus of the research on mechanistic crop models, the thesis provides knowledge only on this type of model further in the text. The beginning of crop modelling dates to the 1960s, when one of the pioneers of agricultural system modelling – physicist C.T. de Wit from Wageningen University believed that agricultural systems can be modelled by combining physical and biological principles. Another pioneer – chemical engineer W. G. Duncan started to design the first crop-specific simulation models for corn, cotton, and peanut. After that, many scientists and engineers followed in their footsteps and worked on the development of these models. Such a project was a development of a production system for increasing cotton production in the year 1969. Later, in 1972, the new research program was launched to create a crop model for monitoring the production of major crops around the world. The CERES-Wheat and CERES-Maize crop models were developed by the research team in Texas, the United States of America, and later evolved and transformed into DSSAT suite of crop models. Either, Wageningen University was developing the former work of C.T. de Wit and trained many agricultural crop modelers, and create several models with different purpose like ORYZA rice crop model or the WOFOST. Another model was developed in Australia and called APSIM by the first fully funded multidisciplinary crop modelling-

oriented research group (Jones et al. 2016). **Figure 3** shows other models created worldwide and their development through the course of time. The STICS model developed at French National Institute for Agricultural Research since the year 1996; A successor of HERMES model – a processed-based agro-ecosystem model named MONICA developed for simulating crop growth and soil processes in Central Europe; The Danish model called DAISY used for simulation of water and nitrogen dynamics and crop growth in agro-ecosystems and AquaCrop model developed by Food and Agriculture Organization (FAO) for lowly detailed input data (Abrahamsen & Hansen, 2000; Brisson N et al. 2003; Foster et al. 2017; Jin et al. 2018; Specka et al. 2015).

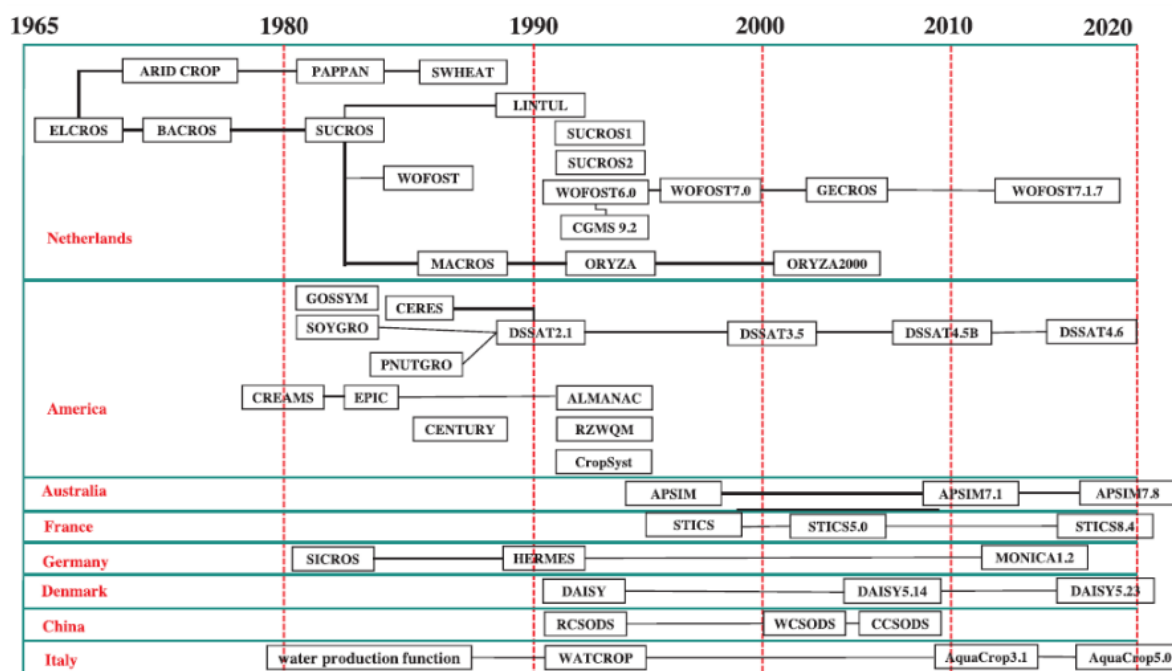


Figure 3. Time development of main crop models. (Source: Jin et al. 2018)

2.2 The WOFOST

2.2.1 Introduction to the WOFOST modelling

The Wofost is the mechanistic model developed at Wageningen University & Research that simulates annual crop growth according to specific soil, weather conditions, and crop management on the basis of biophysical processes such as phenological development, leaf development, and light interception, root growth, CO₂ assimilation, transpiration, respiration, and distribution (partitioning) of assimilates to the different crop organs resulting in biomass production (e.g., total above-ground production – TAGP; total dry

weight of storage organs - TWSO). Potential and two levels of attainable (water-limited and nutrient-limited) production can be obtained (**Figure 2**); nevertheless, reducing factors such as weeds or pollutants are not taken into account (Boogaard et al. 2014; Wageningen University & Research not dated, de Wit et al. 2018).

The simulation mechanisms used by the WOFOST originate from ‘School of de Wit’, which draws the inspiration from the published work of C. T. de Witt on modelling photosynthesis of leaf canopies in the year 1965. In the 1960s, computer science has made sufficient progress, which allows to start building first simulation models using mathematical equations to describe crop behaviour by underlying physiological mechanisms. In addition, the need of advisory systems and decision-making tools for farmers and policy-makers stimulate further development of simulation models. In the Netherlands, At Wageningen University & Research, C.T. Witt and his co-workers have started to develop crop growth models, and since then, many crop models have emerged. The characteristics of these models were determined by already mentioned production levels according to the research goal and aims. Most models of ‘School of de Wit’ have similar key characteristics such as dynamic approach, hierarchical approach, state-variable based model, explanatory model and deterministic model. Photosynthesis of leaf canopies has remained the main core of the ‘School of de Wit’ models, and they are all photosynthesis-driven. The first significant crop growth simulator was ELCROS (ELementary CROp simulator), and its purpose was to explore the potential productions levels of crops under various conditions. In the following years, the ELCROS evolved into the model, which was able to quantify energy requirements for growth and maintenance, but also into the MICROWEATHER model, which provided detailed information about crop micrometeorology. The model BACROS was (BASic CROp growth Simulator) was another important step in ‘School of de Wit’. The model was able to simulate crop growth and transpiration through the whole season under the potential production conditions. Water-limited production was introduced in the next model called ARID CROP and used in the Mediterranean region. In the next important stage during the years 1980 – 1990, the researchers ‘School of de Wit’ started to focus more towards practical application instead of understanding and explaining. In these years, SUCROS, WOFOST, MACROS, and ORYZA were presented. While SUCROS (Simple and Universal CROp growth Simulator) was still a more research-oriented model, the

WOFOST was one of the first application-oriented models. It was derived from SUCROS, and emphasis was on practical application. The model itself focuses on yield forecasting for regions, impacts of climate change, or inter-annual yield variation. Another difference was version control, proper documentation, and open-source code of model (Bouman et al. 1996; de Wit et al. 2018).

2.2.2 The WOFOST simulation processes

The article – *25 years of the WOFOST cropping systems models* (2018) and manuals - *System description of the WOFOST 6.0 crop simulation model implemented in CGMS. Volume 1: Theory and Algorithms* (1994) and *System description of the WOFOST 7.2 cropping systems model* (2020) present almost all-important simulation processes, which were implemented in the WOFOST during the development, and the last version of all processes can be seen in **Figure 4**. Firstly, **Phenological development** serves as an operating mechanism for plant growth. It is expressed by the development stage value, which starts at - 0.1 or 0.0 (sowing or crop emergence) and goes through 1.0 (flowering or anthesis), and ends at 2.0 (physiological maturity). The phenological development is based on the calculation of development increment of a plant is based on daily development rate obtained by:

$$DVR = \frac{F_v * F_p * T_{eff}}{TSUM_{req}} \quad (2.01)$$

Where $TSUM_{req}$ is temperature sum required to complete stage and go to the next stage, while T_{eff} is effective temperature based on difference between the daily average temperature and a base temperature below development of plant doesn't occur. F_v and F_p are factors reducing the development due to vernalisation and Photoperiodism (Boogaard et al. 2014; Supit et al. 1994; de Wit et al. 2018).

Secondly and thirdly, the gross **CO₂ assimilation rate** of the canopy is calculated with the assistance of the **respiration** process. This rate is related to radiation energy absorbed by the canopy and calculated from incoming radiation and crop leaf area. The daily rate of CO₂ assimilation of the crop is then determined by the calculated absorbed energy and photosynthetic characteristics of a single leaf. The growth rate is calculated as follows:

$$\Delta W = C_e * (A - R_m) \quad (2.02)$$

Here, ΔW is growth rate [$\text{kg}\cdot\text{ha}^{-1}\cdot\text{d}^{-1}$], which is determined from the assimilation rate (A) defined by conversion of carbohydrates to biomass. The negative impact on growth rate has maintenance respiration rate (R_m), which is defined by the energy needed for the maintenance of the already formed biomass. In the conversion process, some of the weight is lost due to growth respiration (C_e) (Supit et al. 1994). However, (de Wit et al. 2018) notes that the WOFOST is able to reduce CO_2 assimilation rate by daily minimum temperature. During the low temperatures, the assimilates are not able to convert themselves to structural biomass, and the assimilation rate decreases and even stops.

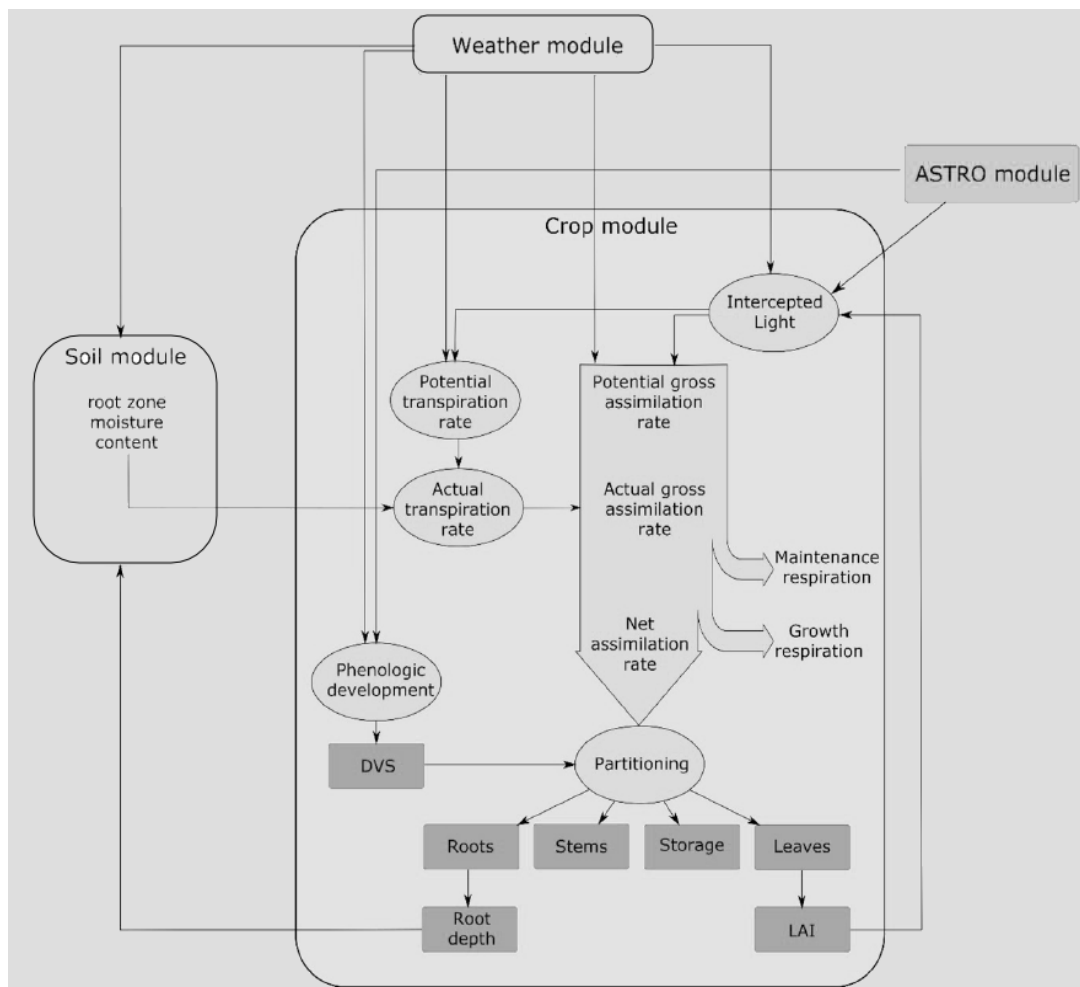


Figure 4. Overview of the WOFOST main processes and their relations. (Source: de Wit et al. 2018)

Fourthly, **partitioning** or distribution of assimilates to different plant organs (e.g., leaves, roots, stems, storage organs) is not run separately, but it is related to the actual development stage of simulated plant (**Figure 4**). The different partitioning tables with

values describing the distribution of assimilates to the plant organs are selected according to the actual development stage of the crop, and increments of dry matters in organs are calculated and recorded. Firstly, dry matter is distributed between shoots and roots as follows:

$$\Delta W_{rt} = pc_{rt} * \Delta W \quad (2.03)$$

$$\Delta W_{sh} = (1 - pc_{rt}) * \Delta W \quad (2.04)$$

Where ΔW is dry matter growth rate total crop [$\text{kg} \cdot \text{ha}^{-1} \cdot \text{d}^{-1}$], ΔW_{rt} is dry matter growth rate for roots, ΔW_{sh} is dry matter growth rate to shoots, and pc_{rt} is partitioning factor of roots. After this fraction, the growth rate of leaves, stems, and storage organs are calculated from dry matter intended for shoots (ΔW_{sh}) as follows:

$$\Delta W_i = pc_i * \Delta W_{sh} \quad (2.05)$$

Where ΔW_i is dry matter growth rate of organ i [$\text{kg} \cdot \text{ha}^{-1} \cdot \text{d}^{-1}$] and pc_i is partitioning factor of organ i and i is calculated organ i.e, leaves, storage organs, or stems. As it has been said, the partitioning depends on the development stage, which is projected by pc_i according to the Arbitrary Function GENERator (AFGEN) tables. It should also be noted that the partitioning factor of leaves, storage organs, and stems should equal to 1, otherwise, simulation will be stopped (Supit et al. 1994; de Wit et al. 2018; de Wit et al. 2020; Wolf & de Wit 2010).

Fifthly, **leaves**, **stems**, and **storage organs** are important components of the WOFOST processes. While storage organs or stems are not so much important in simulation, and there are not so many biophysical processes related to these organs (both organs can contribute to the crop photosynthetic active area), the leaves are important organs because they can determine light absorption and photosynthesis of the crop. The WOFOST simulates the leaf information with a high level of detail according to the temperature and by intake of assimilates. While during the early stages is the temperature important factor for leaf development, during later stages, leaf area expansion is determined by the intake of assimilates. The equation for growth rate in early stage is as follows:

$$L_{Exp,t} = LAI_t * RL * T_e \quad (2.06)$$

Where $L_{Exp,t}$ is growth rate of the leaf area index at time step t ; LAI_t is leaf area index at time step t ; RL is a maximum relative increase of Leaf Area Index and it is a function of effective temperature; and T_e is daily effective temperature. The equation for the later growth stage is as follows:

$$L_{Sc,t} = \Delta W n_{lv} * S_{la} (2.07)$$

Where $L_{Sc,t}$ is growth rate of the leaf area index at time step t ; ΔW_{nlv} is the net dry matter growth of leaves at time step t , and S_{la} is specific leaf area at time step t . The accumulated leaf area index at a specific time of growth is then calculated as follows:

$$LAI_t = LAI_{t-1} + L_{Sc,t} \Delta t (2.08)$$

Where LAI_t is leaf area index at specific time, Δt is a time step (Supit et al. 1994; de Wit et al. 2018, de Wit et al. 2020).

Sixthly, the roots are important in the WOFOST processes from the point of view of rooting depth and biomass increments. The growth of roots is based on the same principles as the growth of other plant organs. The roots absorb a certain amount of the net daily assimilates based on the rate of fraction for roots in a specific time. The root's death material formation is driven by the development stage via a relative death rate. This factor causes that a certain amount of roots die after the specific development stage. The formula for the root growth is as follows:

$$\Delta RD = RR_{max} * \Delta t (2.09)$$

Where ΔRD is the increase of the rooting depth [cm], RR_{max} is the maximum daily increase in rooting depth [$cm \cdot d^{-1}$], and Δt is a time step [days]. The rooting depth is then as follows:

$$RD_t = RD_{t-1} + \Delta RD (2.10)$$

Where RD_t rooting depth at time step t [cm] (Supit et al. 1994; de Wit et al. 2018, de Wit et al. 2020).

The other important part of the WOFOST processes is **transpiration** and **evaporation**. The processes of transpiration and evaporation are expressed by the evapotranspiration rate of a cropped field ET_c :

$$ET_t = T_{max} + E_{s,max} + E_{w,max} \quad (2.11)$$

Where T_{max} is maximum crop transpiration rate [cm.d^{-1}], $E_{s,max}$ is maximum evaporation of a bare soil [cm.d^{-1}] and $E_{w,max}$ is maximum evaporation of a water surface [cm.d^{-1}]. ET_c value defines the need of the crop to compensate water losses due to transpiration by water uptake from the soil. The maximum crop transpiration rate is then defined by the reference evapotranspiration rate and the crop LAI. The correction factor is also presented in the formula because of different crop transpiration rates. The equation is as follows:

$$T_{max} = ET0 * CFET * (1 - e^{-K_{gb}LAI}) \quad (2.12)$$

Where $ET0$ is reference crop evapotranspiration rate [cm.d^{-1}], $CFET$ is crop coefficient (correction factor). K_{gb} is extinction coefficient for global radiation [-], and LAI is leaf area index [ha ha^{-1}]. The maximum evaporation of bare soil is calculated as follows:

$$E_{s,max} = E0_s * e^{-K_{gb}LAI} \quad (2.13)$$

Where $E0_s$ is potential bare soil evaporation [cm.d^{-1}]. The maximum evaporation of a water surface ($E_{w,max}$) is this:

$$E_{w,max} = E0_w * e^{-K_{gb}LAI} \quad (2.14)$$

Where $E0_w$ is potential evaporation rate from a water surface (Supit et al. 1994; de Wit et al. 2018, de Wit et al. 2020).

The last important part is the **soil moisture**. The WOFOST is able to simulate the soil water balance. This is important for the assessment of the crop's capability to replenish depleted water from soil moisture. The actual root zone soil moisture can be calculated as follows:

$$\theta_t = \theta_{t-1} + \frac{IN_{up} + IN_{low} - T_a}{RD} \Delta t \quad (2.15)$$

Where θ_t is actual moisture content of the root zone at time step t [$\text{cm}^3.\text{cm}^{-3}$], IN_{up} is rate of net influx through the upper root zone boundary, IN_{low} is rate of net influx through the lower root zone boundary, T_a is actual transpiration rate of crop [cm.d^{-1}], RD is actual rooting depth [cm], Δt is time step [days]. IN_{up} and IN_{low} is then calculated as follows:

$$IN_{up} = P + I_e - E_s + \frac{\delta SS_t}{\Delta t} - SR \quad (2.16)$$

$$IN_{low} = CR - Perc \quad (2.17)$$

Where P is precipitation rate [cm.d⁻¹], I_e is effective daily irrigation [cm.d⁻¹], E_s is soil evaporation rate [cm.d⁻¹], δSS_t is surface storage [cm], SR is rate of surface runoff [cm], CR is rate of capillary rise [cm d⁻¹] and Perc is the percolation rate [cm.d⁻¹] (Supit et al. 1994; de Wit et al. 2018, de Wit et al. 2020).

2.2.3 The WOFOST input/output data and calibration

The input data are an important part for the setup of WOFOST and the whole process of simulation. Generally, it can be distinguished according to soil-crop-atmosphere interactions on general data, crop data, weather data, timer data, soil data, and nutrients data. Several decades of development brought several changes of input parameters; however, the basic structure remains the same (Boogaard et al. 2014; van Diepen et al. 1989).

The general data provides information about the production level of the crop model. The WOFOST contains three scenarios – simulation of potential crop growth, simulation of water-limited growth, and simulation of nutrient-limited crop growth. The crop data are datasets of parameters and attributes of crops necessary for the simulation of crop growth. These datasets can be calibrated for different crops and their varieties according to the experimental field data and reviewing the literature. The calibration of the model, in this case, means adaptations of parameters or relations according to the environment for a good fit between results and measured variables (Boogaard et al. 2014; Kersebaum et al. 2015; Ma et al. 2013a). The weather data are essential input data and can have a large impact on the simulation of crop growth and final yield. Mishra et al. (2015) stated that sunshine hours can increase the yield and *vice versa*, while an increase of maximum temperature by 5 °C can reduce the yield forecasting significantly. The set of weather data usually comprises maximum and minimum temperatures, rainfall/precipitation, wind speed, water vapor pressure, global radiation, and evapotranspiration (van Diepen et al. 2004; van Goot et al. 2013; Kersebaum et al. 2015). The timer data consist of all critical data about the start of simulation, duration, and end of the simulation. The soil and nutrients data determine the soil type, hydrological characteristics, and fertility of the soil (Boogaard et al. 2014).

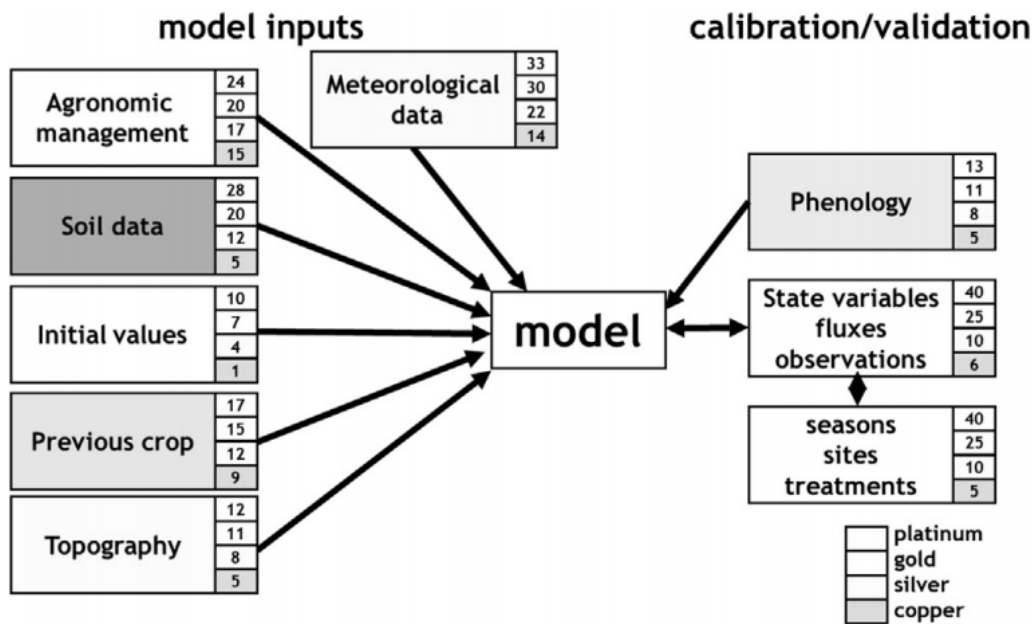


Figure 5. Variable block and their minimum sums of weighting points required for each quality class. (Source: Kersebaum et al. 2015)

Kersebaum et al. (2015) highlighted the differences in many processes due to spatial and temporal variability. The variation in conditions can be significant within small distances, and it can increase the uncertainty of simulation over the large areas. That's why it is desired to have high-quality data from experimental field measurements. The quality of necessary field experimental measurement can be classified into four classes - "copper", "silver", "gold" and "platinum. While copper (the lowest) rating criteria represents fair quality of observed data and some variety trials, the platinum (the highest) criteria suppose high-quality data for model calibration and in-season and end-of-season measurements. The necessary input data and requirements of weighting points can be seen in **Figure 5** (Boote et al. 2016; Kersebaum et al. 2015).

2.2.4 Python Crop Simulation Environment

The Python Crop Simulation Environment (PCSE) is a package for a Python programming language and is intended as a software architecture for crop simulation models. It also contains the tools for processing weather, soil, and crop management data and other vital components for the simulation of important biophysical processes. The PCSE also contains the LINTUL3 and the WOFOST, already described in the previous chapter. The PCSE was created because of development in computer science, which made

usage of the WOFOST in FORTRAN programming language outdated (de Wit 2018). On the other hand, Python is the important programming language for scientific purposes, and it has a better option to integrate it with other different tools (e.g., databases, programming environments, websites). It also offers optional scientific and numerical libraries (e.g., NumPy, SciPy, Pandas) (**Figure 6**), and moreover, it was used for many environmental modelling (Knox et al. 2018; de Wit 2018; Wohlstadter et al. 2018).

```

for index, row in sowing_dates.iterrows():
    # sowing date Load
    print(row['sowing_date'])
    sowing = row['sowing_date']
    sowing = sowing.to_pydatetime().date()
    offset_date = sowing + relativedelta(years = 1)
    cropdata = YAMLCropDataProvider(data_dir)
    # Crop data
    cropdata.set_active_crop('wheat', 'Wheat_Vendoli_calibrated_2016_2019')
    # Site parameters
    sitedata = WOFOST71SiteDataProvider(WAV=29.5, CO2=360)
    soilfile = os.path.join(data_dir, 'EC2_soil')
    soildata = CABOFileReader(soilfile)
    # ALL parameters
    parameters = ParameterProvider(cropdata=cropdata, sitedata=sitedata, soildata=soildata)
    # Building agromanagement file
    filename = "{crop_type}_agro_onfly.agro".format(crop_type = crop_type)
    with open(filename, 'wt') as f:
        f.write(template.format(start=sowing, end=offset_date,
                                crop_start_type = "sowing", crop_end_type = "maturity",
                                max_duration = 500, crop_type = crop_type,
                                crop_variety = crop_variety))
    f.close()
    agromanagement_file = os.path.join(data_dir, "{crop_type}_agro_onfly.agro".format(crop_type = crop_type))
    agromanagement = YAMLAgroManagementReader(agromanagement_file)
    print(agromanagement)
    # Loading weather/climate data
    weatherdataprovder = wdp
    # WOFOST simulation
    wofsim = Wofost71_WLP_FD(parameters, weatherdataprovder, agromanagement)
    wofsim.run_till_terminate()
    # Getting results
    output = wofsim.get_output()
    df = pd.DataFrame(output)
    df.to_excel(f"Wheat_{sowing}_{row['ID_pole']}_{row['year']}.xls")
    sumout = wofsim.get_summary_output()
    print(sumout)
print('Simulations done')

```

Figure 6. PCSE programming workflow in Visual Studio Code.

2.2.5 Research activities and practical use of the WOFOST

The WOFOST crop growth model is used by various research and governmental/intergovernmental institutions. The following chapter will describe the most significant development and practical utilization of the WOFOST. On the governmental/intergovernmental level, the WOFOST is used by the Joint Research Centre of the European Commission for Monitoring Agriculture with Remote Sensing (MARS) in a unit called Mars Crop Yield Forecasting System (MCYFS). The MARS forms a

technical and scientific unit for support of European Union agriculture and Food Security policies. MCYFS mission is the crop yield forecasting for the staple crops applied in Europe and neighbouring countries. This is helpful for the stabilization of the agricultural market and preventing fluctuations in prices. The forecasts are published in the so-called MARS Bulletins. The main structure of MCYFS (**Figure 7**) includes several interconnected software tools, including Crop Growth Monitoring System (CGMS). The CGMS is based on the gridded run of the WOFOST at a large scale. The WOFOST forecasts soft wheat, durum wheat, barley, rye, rapeseed, potatoes, and sugar beet. The outputs of the model are used as decadal predictors in statistical analysis on the national level (). A similar utilization of the WOFOST was implemented in Belgium, China, and Morocco. The Belgian Crop Growth Monitoring System provides a forecast for six staple crops on the national and regional level with a spatial resolution of 1 km, 5 km, and 10 km. The core of the crop growth modelling is built up with the WOFOST supported by remote sensing methods. The China-CGMS is also partially driven by crop modelling with the WOFOST reaching an accuracy of 88%. However, this system also contains other models – CROPWAT and ORYZA2000. Similar to Belgium, Morocco has implemented an adapted, and improved version of CGMS called CGMS-MAROC. The Moroccan system is also built up with the use of the WOFOST; however, it also uses statistical models based on measurement of NDVI for forecasting the cereals (Bernardi et al. 2016).

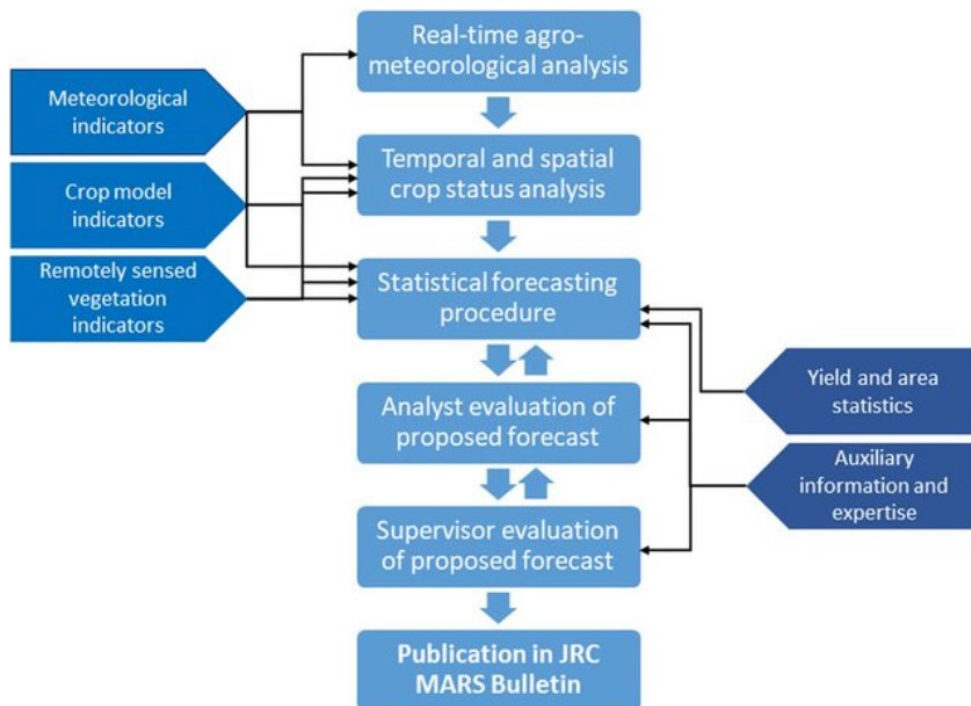


Figure 7. MARS-Crop Yield Forecasting System workflow. (Source: van der Velde et al. 2018)

The following paragraph presents a review of recent literature on the WOFOST crop growth modelling. As it was described earlier, the WOFOST crop model can be used for crop growth forecasting and biomass (crop yield) estimation. The yield forecasting for various crops has been examined by many authors. Wheat, rice, maize seems to be the most analyzed crops by the WOFOST according to the Google scholar search results; however, the barley, rapeseed, potato, sorghum, millet, sugar beet, sunflower, and other crops can be found too (Google Scholar, Not dated). For example, Ceglár et al. (2019) were proposed improvements of modelling with increased accuracy of wheat anthesis and yield forecasting by examination of calibrated phenological modelling. Hensawang et al. (2021) were predicting the rice production in Central Thailand with 16 % discrepancy. Eweys et al. (2017) integrated the WOFOST with Noah Land Surface Model in order to obtain precise simulations of maize growth resulted in 11 % discrepancy. Concerning the other crops, Kulig et al. (2020) performed the crop modelling of potatoes. Wang et al. (2018) used the WOFOST for assessing the scope for potato production in China with the

conclusion that potatoes have better potential to sustain food security and self-sufficiency compared to cereal crops. Spring barley yield was examined by Rötter et al. (2012) in Northern and Central Europe by nine crop growth models. They concluded that the WOFOST provided the best estimates together with HERMES and MONICA. Gilardelli et al. (2016) developed the WOFOST-GTC for simulation of winter rapeseed production and oil quality with an accuracy of R^2 of 0.86 and 0.78 for above-ground biomass and photosynthetic area index. Sayyahi et al. (2020) recently evaluated WOFOST together with AquaCrop for simulation of Sugar Beet. They concluded that the simulation of the WOFOST was worse than AquaCrop; however, with decent performance. The sunflower yield was forecasted in Inner Mongolia, China by Zhu et al. (2018) with the highly accurate prediction (RMSE of $56 \text{ kg}\cdot\text{ha}^{-1}$).

Although the main goal of WOFOST crop modelling is the simulation of crop growth and forecasting of yield, the scientific utilization can be quite diverse. The literature review shows that the WOFOST can be used for monitoring the climate change impacts, tracking the impacts of water or oxygen stresses, revealing the production potentials, using the model for assessment of yields in saline soils, and many others. Bassu et al. (2021) recently tried to use the WOFOST for the prediction of maize yields in 2041–2060 under future climate conditions with resulted in 14 % - 17 % average yield reduction. The extreme weather events were analyzed via WOFOST to assess the impact on crop production by Gilardelli et al. 2018. It was found that crop yield forecasting on a European level is limited in the prediction of climate shock's impacts on yield formations. The authors proposed new modelling solutions for weather extreme situations for increasing efficiency. Yan (2015) evaluated the influence of water and oxygen stress on potato yield in the Netherlands, concluding that yield reduction could be explained by the water limitation; however, the yield reductions cannot be explained properly by oxygen stress. The impact of soil salinity on crop yields was described by Zhu et al. (2018) via adjusted WOFOST. The authors concluded that the adjusted model is able to reflect environmental stresses such as salinity. The nitrogen-limited production crop growth was successfully tested by Groenendijk et al. (2016) with SWAP/WOFOST joint model. The cadmium stress affecting rice production was assessed by Liu et al. (2015) via an improved WOFOST model resulted in a successful method of crop growth simulation under the cadmium stress. The WOFOST is very often used jointly with remote sensing techniques;

however, since this research addresses this topic, this technique will be more thoroughly described in chapter 2.4.

2.3 Remote Sensing

Remote sensing has many definitions, but generally, it can be said that it is the acquisition of information about an object without the need for direct contact or touch. The history of remote sensing starts in the year 1858, when Gaspard-Félix Tournachon (1829-1910) acquired the first aerial photo from a balloon in France. Since then, the development of remote sensing gone through aerial reconnaissance to launch of first Landsat 1 in the year 1972. After this year, advances in remote sensing and digital image processing bring new possibilities in monitoring Earth's surface. New possibilities how to monitor the Earth's surface through the optical, radar, lidar sensors, and other Unmanned Aerial Vehicle (UAV) were revealed with different vegetation indices or polarimetry and interferometry (Kasampalis et al. 2017; Cambell et al. 2011).

Last decade, several missions from the European Copernicus programme were started with the goal to monitor the Earth's surface. Among them, Sentinel-1 and Sentinel-2 (**Figure 8**) are important for agricultural monitoring. The Sentinel-1 contains a constellation of two satellites with C-band SAR (Synthetic-aperture radar; 5.405 GHz) instrument on its board able to obtain data in dual-polarization (Vertical Horizontal [VH] + Vertical Vertical [VV]) with operational modes Interferometric wide-swath mode at 250 km and 5×20 m resolution; Wave-mode images of 20×20 km and 5×5 m resolution (at 100 km intervals); Strip map mode at 80 km swath and 5×5 m resolution; Extra wide-swath mode of 400 km and 20×40 m resolution. The revisit period is 6 days with two satellite platform constellations (ESA Not dated - a; Potin et al. 2016). The Sentinel-2 satellites are also part of the European Copernicus programme. There are two identical satellites providing multi-spectral observations at global coverage of the Earth's land surface. Multispectral imager is able to provide images at 13 spectral bands (443 nm–2190 nm) with a swath width of 290 km. Spatial resolution is 10 m for 4 visible and near-infrared bands, 20 m for 6 red-edge/shortwave-infrared bands) and 60 m for 3 atmospheric correction bands. The revisit period is up to five days. The orbit is polar and sun-synchronous at the altitude of 786 km (ESA 2011; ESA Not dated - b; Koetz et al. 2021; de Kok et al. 2017).

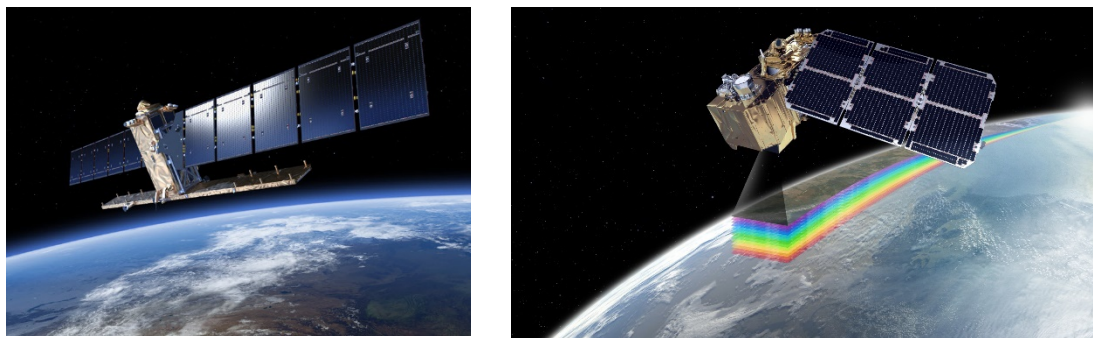


Figure 8. Sentinel-1 (left) and Sentinel-2 (right). (Source: Copernicus Not dated - c; AIRBUS 2020)

2.3.1 Optical Vegetation Indices

One of the most essential activities of optical remote sensing is vegetation monitoring. There are lots of indices used for the determination of vegetation cover. Probably the most common one is the Normalized Difference Vegetation Index (NDVI) used by many ecologists and agriculturalists. Rouse et al. (1974) presented this index in 1974. The NDVI estimates green biomass and vegetation cover and is defined as the difference between the Near Infrared and Visible bands divided by their sum (Fan & Liu 2016; Fern et al. 2018; Rouse et al. 1974; Gao 1996). Other optical vegetations indices include the Ratio Vegetation Index (RVI 2), the Difference Vegetation Index (DVI), the Perpendicular Vegetation Index (PVI), the Atmospherically Resistant Vegetation Index (ARVI), Soil-Adjusted Vegetation Index (SAVI), the Crop Water Stress Index (CWSI), the Photochemical Reflectance Index (PRI), the Normalized Difference Water Index (NDWI) (Xue & Su 2017; Gao 1996).

Another important index for measuring vegetation characteristics by remote sensing is LAI. The LAI is the ratio of leaf area per ground surface area. The LAI can provide important information related to photosynthesis or transpiration and carbon fluxes. It is also a good indicator for growth stages of crops and yield estimations (Herrmann et al. 2011; Kappas & Propastin 2011; Zheng & Moskal 2009). Since the LAI is an essential aspect of this work, it is important to provide some development of current research using the optical data. A series of recent studies showed that estimation of LAI by optical remote sensing can be diverse - from forest monitoring (Tillack et al. 2014) to the estimation of LAI for wheat (Li et al. 2018; De Peppo et al. 2021; Afrasiabian et al. 2021), maize (Manzane et al. 2018) to grazing pastures (Wang et al. 2019). Cited research

suggests that statistics and machine learning methods are commonly used for the prediction of LAI. Several other authors also used machine learning for the prediction of LAI. For example, Houborg et al. (2018) used random forests (RF) decision trees for promising estimation of LAI. Omer et al. (2016) used support vector machines (SVM) and artificial neural networks (ANN) for empirical prediction of LAI of Endangered Tree Species. The ANN was also used by Bochenek et al. (2017) for the estimation of wheat LAI in western Poland. Deep learning was used by Yamaguchi et al. (2021) for the analysis of RGB images obtained from Drone’s (Unmanned Aerial Vehicle) optical camera for LAI estimation for rice. The pipeline for such a method can be seen in **Figure 9**. As can be seen, the labeled RGB images with direct LAI measurements are necessary for the Deep learning model setup. Such a model can then predict LAI with the accuracy of $R^2 = 0.963$ and $RMSE = 0.334$.

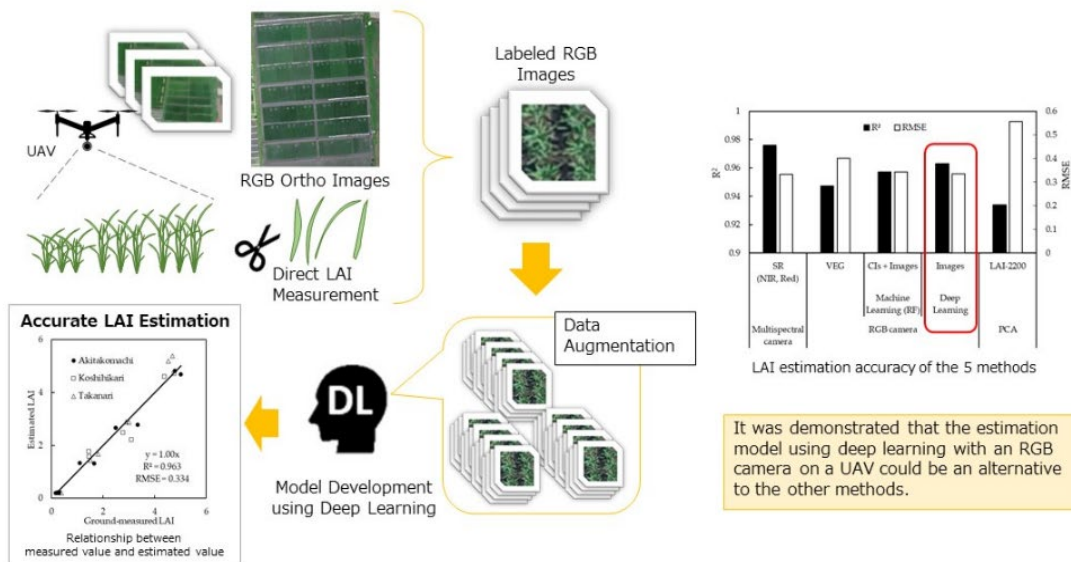


Figure 9. MARS-Crop Yield Forecasting System workflow. (Source: Yamaguchi et al. 2021)

2.3.2 Radar Vegetation Index

The SAR satellites represent active remote sensing, which is able to transmit energy at microwave wavelengths toward the object of interest from beaming instruments and measure the reflected energy (backscatter). At the same time, the data acquisition is not influenced by cloud cover or daytime. This represents the advantage for monitoring the Earth’s surface compared to the optical remote sensing. Therefore, changes in soil and

crop conditions in agricultural fields can be observed more frequently. Moreover, SAR monitoring can be crucial for various agricultural activities, which are time-fixed (Musa et al. 2015; McNairn & Brisco 2004, Kim et al. 2012, Jiao et al. 2014). Kim et al. (2012) pointed out that microwave remote sensing has potential to complement the other remote sensing methods (e.g., optical) in the monitoring of crops. Many other scientists came to a similar conclusion (Malenovský et al. 2012; Fieuzal et al. 2013; Jin et al. 2015; Baghdadi et al. 2011).

The Radar Vegetation Index (RVI) was proposed as an indicator of vegetation growth obtainable from co-polarized and cross-polarized backscatter radar signal (Kim & van Zyl, 2004; Kim & van Zyl 2009). The RVI estimates the randomness of scattering and generally ranges from 0 (smooth bare surfaces) and increases with vegetation content to 1 (Kim et al. 2014 - b). A number of authors has recognized that strength of backscatter is the function of vegetation canopy characteristics and phenological development (orientation of the canopy parts, shape and amount of canopy, or dielectric properties) and SAR instrument configuration (band, polarization, or incidence angle) (Koppe et al. 2013; Jiao et al. 2014). Moreover, the backscatter seems to have the most significant and relative results in ratios (e.g., HV/VV or HH/VV) (Sánchez et al. 2016; Blaes et al. 2006). The ratios were used during the crop classification by Inglada et al. (2016) or Denize et al. (2019) but also during the phenological development monitoring (McNairn et al. 2018; Wang et al. 2019, Canisius et al. 2018).

RVI retrieved from different satellites for monitoring crops as an alternative to NDVI was examined by Kumar et al. (2013) or Gonenc et al. (2019). Kumar et al. (2013) found out that seasonal monitoring of crops by RVI can be effectively used. Moreover, the RVI seems to not experience the saturation as NDVI does. Nevertheless, the RVI cannot simply replace the NDVI, and more research on establishing the biophysical parameters needs to be done. Kim et al. (2012, 2014 - a) examined retrieval of RVI with the use of L-, C-, X-band from multifrequency polarimetric scatterometer over the wheat, rice, and soybean fields and Huang et al. (2016- b) through the Soil Moisture Active Passive (SMAP) mission of the National Aeronautics and Space Administration. Both investigations analyzed the RVI results with vegetation water content (VWC), and while the scatterometer revealed a perfect correlation between the RVI and VWC (also the fresh weight), the SMAP was not so successful, and only a moderate positive correlation was

found. In 2012, The ComRAD system measurement (**Figure 10**) was conducted over the maize and soybean fields with the aim to measure RVI and compare it with VWC. A correlation of 0.58 (moderate positive correlation) was obtained (Srivastava et al. 2015).



Figure 10. The ComRAD Microwave Instrument System – measuring the RVI.
(Source: Srivastava et al. 2015)

A series of recent studies have examined RVI from different perspectives. Haldar et al. (2020) found out a potential application of using the truncated equation of RVI for estimation of cotton VWC with 30 – 35 % error above 4 kg.m^{-2} biomasses and 20–25% error in lower ranges using the RISAT-1 data. Mustard and wheat phenology was examined by Haldar et al. (2021) using Sentinel-1 data and machine learning methods for predictions of phenophases. The machine learning model was able to predict the initial to medium part of mustard and medium to late part of the wheat-crop cycle. The modified RVIs were presented for efficient monitoring of the Earth's surface. Szigarski et al. (2018) was testing the SMAP L-band radar data globally and proposed changes to RVI for the obtainment of a normalized value range. The soil scattering would be suppressed by subtract of attenuated soil scattering contribution from the measured backscattering signals. The RVII and RVIII were proposed with lower dependence on soil roughness and soil moisture. Dual Polarization SAR Vegetation Index (DPSVI) was proposed by

Periasamy (2018) based on analysing SAR data clouds of backscattering coefficient. A positive correlation was obtained between RVIs and VWC or LAI. Another adjusted RVI was proposed by Chang et al. (2018) for measuring the shrublands biomass by PALSAR full and dual-polarization L-band and Sentinel-1 dual-polarization C-band. The polarimetric radar vegetation index (PRVI) was tested and compared to RVI. The biomass prediction from PRVI indicates better performance than RVI predictions (RMSE of 0.329 kg.m⁻² vs. 0.439 kg.m⁻²). Compact polarimetric SAR data were used for a new vegetation index called CpRVI by Mandal et al. (2019). The tests proved that CpRVI correlates better with Plant Area Index and WVC than RVI. Also, Mandal et al. (2020 - b) investigated the use of a Generalized volume scattering model-based Radar Vegetation Index (GRVI) for monitoring rice growth at different phenological stages. They found out that GRVI outperformed the RVI in the temporal monitoring of crop biophysical parameters. In the same year, Mandal et al. (2020 - a) presented the dual-pol Radar Vegetation Index (DpRVI) with the aim to utilize the eigenvalue spectrum. The subsequent investigation over the canola, soybean, and wheat field showed that the DpRVI outperformed compared indices (cross, co-pol ratio, RVI, PRVI, DPSVI) in correlation results. The proposed indices were already used in several studies. Pearl millet/bajra crop was assessed by Selvaraj et al. (2021) by both polarimetric Radarsat-2 and dual-polarized Sentinel-1 datasets. DPSVI was modified by dos Santos et al. (2021) during the monitoring of tropical regions and used for monitoring of Atlantic Forest fragments. DpRVI, PRVI and RVI were appraised with Sentinel-1 (C - band) and ALOS-2 (L - band) satellite data over the wheat, barley, and mustered fields in Rabi season and rice in Kharif season by Yadav et al. (2021). All the used indices show the highest correlation and low RMSE at L – band measurement. The DpRVI has the best results for the L – band.

2.4 Assimilation of remotely sensed data

Data assimilation is a crucial method frequently used for atmosphere, ocean, and land surface examination. The combination of observation/measurement and the system's dynamical principles provides a more accurate state of the system than obtained just using observation/measurement data or model prediction. In previous years, many deterministic models were developed for simulation of environmental processes how it was indicated in **chapter 2.1**. These models are mathematically describing biophysical processes that

govern the functioning of land surfaces, however with some uncertainty (errors; heterogeneity). The development of Remote Sensing has allowed monitoring the Earth's surface and provides important information on temporal and spatial variability. This information can be turned to important biophysical characteristics such as soil moisture, leaf area, or evapotranspiration. And although Remote Sensing has lots of limitations, it can provide a good source of data for deterministic modelling. Primarily, the advantage of spatial variability can be used for improved yield forecasting and crop monitoring. The idea of assimilation of remotely sensed data into the crop models is based on repetitive screening of earth surface and on simulation of models to provide the best possible estimation of surface characteristics. The assimilation methods can have many forms; however, there are three main methods of combining remotely sensed data with crop models. The first method is an indirect approach of adjustment of crop models by remotely sensed data. The second method – forcing method replaces the simulated data of crop models by remote sensed data. The third method is using the recalibration method to adjust model parameters based on remote sensing data. The basic concept described above can be seen in **Figure 11** (Kasampalis et al. 2017; Tupin et al. 2014; Zhang & Moore 2015).

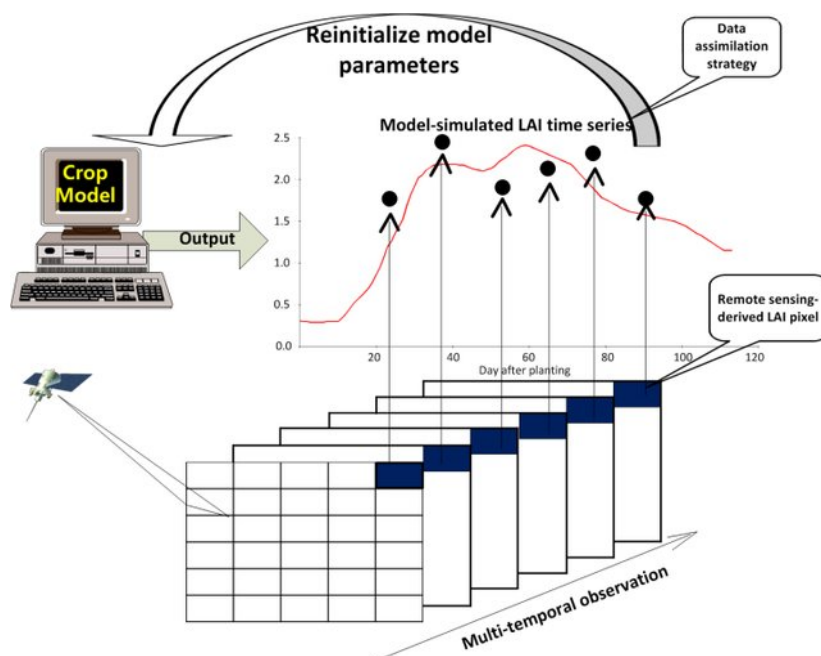


Figure 11. Schematic for assimilation of remote sensing data into crop models.

(Source: Pan et al. 2017)

Since the remote sensing techniques started to offer more reliable quantifications of vegetation canopy or soil properties such as LAI, canopy cover, biomass, evapotranspiration, or soil moisture, the crop growth modelers used these estimations for crop modelling (Jin et al. 2018). Several previous studies used remote sensing for the estimation of canopy state variables and integrated them into the crop models. Bouman 1995 indicated approaches for integration of remote sensing data to crop models. Fang et al. (2008; 2011) used the assimilation method to CERES model for the prediction of maize. Then other authors continued with data assimilation methods (de Wit & van Diepen CA 2007.; Huang et al. 2015; Jiang et al. 2014). The basic concept of data assimilation can be seen in **Figure 12**. In practice, the dynamic crop growth model, as described previously, generally consider vertical column with soil and the vegetation canopy level. The model space x gives a vector of variables in a specific location (grid) which can differ from the satellite data grid (observation space y) at a specific time. State variables (*prognostic variables*) as soil moisture, temperature, or LAI are principal for the system at a specific time and can be corrected via data assimilation. As it was described in previous chapters 2.3.1 and 2.3.2, remote sensing can predict these chapters from measurements of back-scatter, reflectance, or brightness temperature. Both the model of the system and remote sensing observations are uncertain to a certain degree. There are several types of uncertainty. Firstly, the uncertainty is linked to the initial conditions of a simulated variable. Secondly, the errors originated from forcing variables (energy, water and/or carbon balance equations) generally impacting the state variables. Thirdly, there are uncertainties related to parameters of dynamic growth model such as hydrological parameters. Fourthly, uncertainties rise also from remote sensing observations of state variables that originate from errors of measuring instruments. Fifthly, the uncertainties in the process of modelling. These uncertainties are needed to be expressed by error distribution (mostly by Gaussian form assumption). Then the assimilation process can be carried out (Tupin et al. 2014).

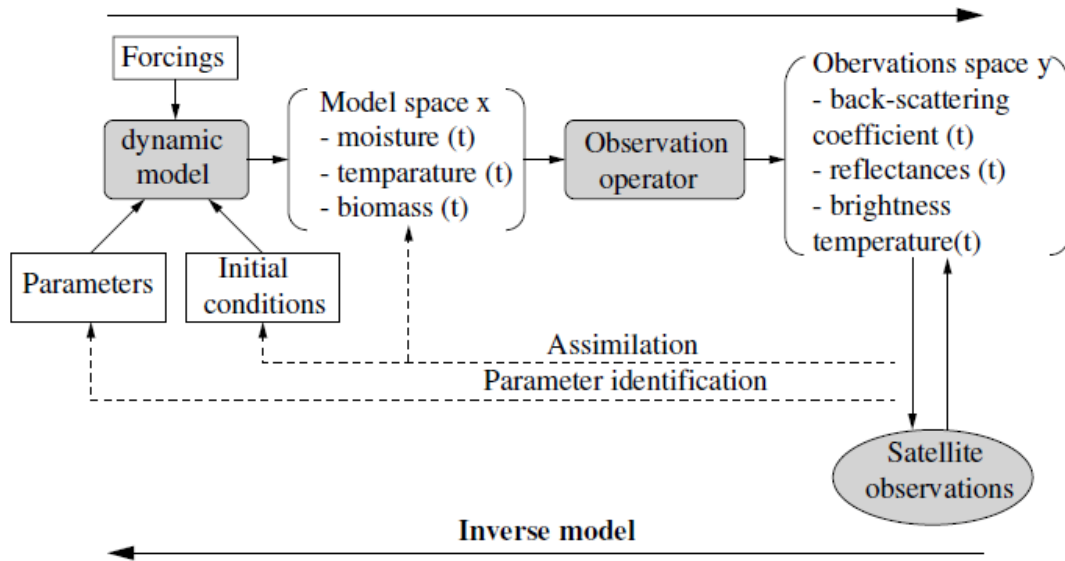


Figure 12. Main elements of data assimilation. (Source: Tupin et al. 2014)

Jin et al. 2018 presented main (updating) assimilation methods in crop modelling - Kalman Filter (KF), Ensemble Kalman Filter (EnKF), Three-Dimensional Variational Data Assimilation (3DVAR), Four-Dimensional Variational Data Assimilation (4DVAR), Particle Filter (PF), and Hierarchical Bayesian Method (HBM). While 3DVAR and 4DVAR were mainly used during the weather forecasting, the EnKF (and KF) were successfully used for data assimilation of remote sensing data into crop models. Many authors used this method in the past in crop modelling with different purposes (Hadria et al. 2006; de Wit & van Diepen 2007; Bolten et al., 2010; Li et al. 2011; Nearing et al., 2012; Ines et al. 2013; Chakrabarti et al. 2014, Hu et al. 2018).

Concerning the WOFOST and EnKF, several studies were performed. De Wit & van Diepen (2007) examined the use of EnKF in the WOFOST for crop yield forecast of winter wheat and maize in Spain, France, Italy, and Germany for the period 1992–2000. 66% of winter wheat regions improved the forecasting compared to statics. Only 56 % of regions with maize recorded the improvement (probably due to irrigation exclusion from the model). Curnel et al. (2011) suggested the potential improvement by assimilation of LAI to the WOFOST based upon the Observing System Simulation Experiment (OSSE) over the wheat fields. However, this research concluded that EnKF is not suitable for LAI data assimilation in the WOFOST due to the increased error of the final yield forecast. In the same year, Wu et al. (2011) investigated the possibility of using MODIS-LAI as a source for data assimilation into the WOFOST. They concluded that EnKF assimilation

method has great potential in regional crop production forecasting. Ma et al. (2013) used NDVI timeseries as the data source for assimilation into the WOFOST with partial success in the improvement of yield forecasting accuracy. Zhao et al. (2013) also examined the use of MODIS-LAI for EnKF data assimilation for simulation of maize growth in the WOFOST and found that assimilation improved the accuracy of the model. Other MODIS data assimilation was examined by Liu et al. (2014), which adjusted the LAI timeseries by Savitzky–Golay filter and assimilated into the WOFOST by EnKF resulted in higher accuracy and smaller errors. Huang et al. (2016 - a) used the MODIS and Landsat images for the creation of synthetic LAI and assimilated these data to the WOFOST by EnKF. The adjusted simulation of wheat with 1-km resolution was improved significantly. Two research activities recently examined the use of Sentinel-1 and Sentinel-2 for data assimilation into the WOFOST. The first one, performed by Zhuo et al. (2018, 2019), presented the possibility to adjust the WOFOST by remotely sensed soil moisture from SAR and optical sensor by so-called joint assimilation. They presented that they are able to decrease the error of simulation significantly. The second one was conducted by Pan et al. (2019), which also used a similar approach; however, the LAI and soil moisture were correcting the WOFOST model. The results show that simulation with joint assimilation of soil moisture and LAI can improve the model better than the model using only one of these state variables. Recently, Wu et al. (2020) presented the EnKF assimilation of LAI obtained from Sentinel-2 to the WOFOST with a good improvement of accuracy.

To our knowledge, no prior studies have examined the prediction of LAI from RVI data derived from Sentinel-1 according to the LAI products obtained from Sentinel-2 imagery. There are some potentially open questions about the validity of this approach, and therefore it is needed to examine the relation of RVI and optical indices and use them during the data assimilation to the crop model.

3. Aims of the thesis

The main objective of the research was to explore the possibilities of assimilation methods for the simulation of crop growth with the utilization of synthetic aperture radar data and to provide more accurate and reliable quantitative estimates of crop attributes.

To achieve this objective, the following research activities have been defined as follows:

- To calibrate crop parameters and the attributes of the crop model;
- To set up soil and other initial values of crop model;
- To input weather data into the crop model;
- To retrieve Leaf Area Index from optical satellites and SAR satellites;
- To assimilate Leaf Area Index into crop model by different methods;
- To compare estimations from different simulations using optical or radar data with actual results.

4. Hypotheses / Research questions

The research of this thesis was carried out under the certain hypotheses, based on gained experience, literature review, and observations obtained during past studies and research.

4.1 Hypothesis 1

Assimilation of Synthetic-aperture radar data into the simulation of crop growth can avert errors of simulation process and provide smaller errors than the assimilation of optical data.

4.2 Hypothesis 2

Availability and regularity of Synthetic-aperture radar data can have a positive impact on the sequential update method and affect the simulation of crop growth more fluently than optical data.

5. Methodology

5.1 Fields and Data

5.1.1 Research sites

The Research site can be found in the surroundings of the village of Vendolí in the eastern part of Bohemia. The coordinates for the village are 49°44'21.7"N latitude and 16°25'24.6"E longitude (**Figure 13**). Research agriculture fields belong to the Vendolí agricultural cooperative (ZD Vendolí). The total agricultural area of ZD Vendolí's agricultural fields is 1168 ha. The number of observed fields were 10 fields for the year 2016, 12 fields for 2017, 11 for 2018, and 19 for 2019 (**Figure 14; Table 1**). The agronomical vegetation season generally starts around end of March and ends in the middle of August (154 days). The NASA POWER database was used as a source for average meteorological characteristics, with records from 1983 until now (Sparks 2018). The precipitation volume during the vegetative period is 354.3 mm, while daily air temperature is 14.1 °C with the daily minimum temperature reaching 8.7 °C and the daily maximum temperature reaching 19.1 °C. Estimated Penman-Monteith potential evapotranspiration from a crop canopy is 0.318 mm per day. The sum of active temperatures (more than 10 °C) is, on average, 1957.5 °C (Tůma et al. 2021).

The landscape is hilly, with an average elevation reaching 497 meters above global mean sea level (Baltic) and an average slope of 4.5 %. The soil is generally classified as modal cambisols; however, in higher parts, there is the calcareous sandstone. Several areas with sloped terrain are heavily eroded. Also, a large number of mineral skeletons (rock fragments bigger than 2 mm) can be found on the upper parts of the agricultural fields (Tůma et al. 2021).

The agriculture cooperative uses conventional arable soil tillage technologies based on ploughing. The agricultural system can be classified as sustainable with organic and mineral fertilization. A minimum of synthetic fertilizers is used according to agronomical signaling and predictions. The fertilization phases are regenerative during the formation of a crop's side shoots (tillering), productive during the shoot development, and qualitative in time of heading and flowering. The crop rotation system in agricultural

cooperate crop systems in the Czech Republic – that is usually based on altering of wheat, oilseed rape, barley, maize, peas, and clover crops (Tůma et al. 2021).

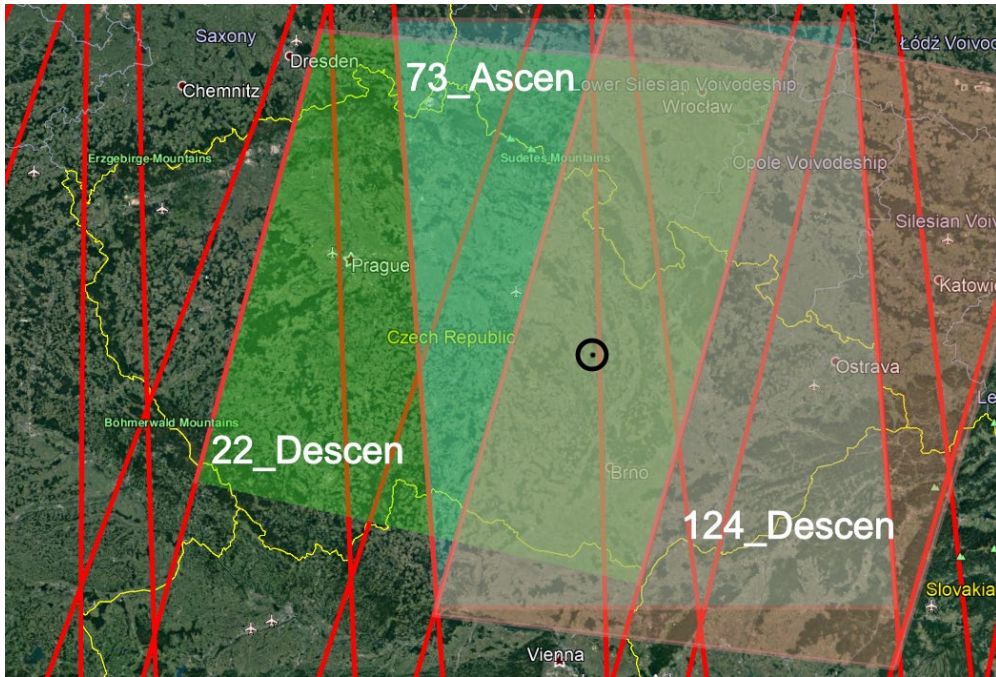


Figure 13. Location of the Research area and Relative orbits over the area. (Source: Tůma et al. 2021)

Table 1. Overview of Research area and Satellite images scenes (Source: Tůma et al. 2021)

Year	Total num. of Sentinel-2 images	Total num. of Sentinel-1 images	Number of observed fields	Total area [ha]	Average yield [t.ha ⁻¹]
2016	3	44	10	256.47	6.24
2017	5	92	12	236.39	8.07
2018	2	87	11	286.40	7.57
2019	8	89	19	248.40	6.78

5.1.2 Wheat fields monitoring and measurements

Wheat and rape seed were monitored in the scope of the research activities, which resulted in the scientific paper - *The Noise-reduction Potential of Radar Vegetation Index for Crop*

Management in the Czech Republic (Tůma et al. 2021). However, to achieve the goals of this thesis, only wheat monitoring methodology and results were used.

The wheat field was monitored in 4 vegetation seasons (VS), i.e., 2015/2016, 2016/2017, 2017/2018, and 2018/2019. However, the main part of the analysis was performed in the main vegetation season – from March (BBCH 20 / tillering for cereals / formation of side shoots for oilseed rape) to a stage when the phenological phase BBCH 89 begins (usually July / Fully ripening). **Figure 14** provides delineations of cultivated wheat fields in the surroundings of Vendolí. Due to the classical crop rotation system, the wheat was cultivated in different locations each season. **Table 2, 3, 4, and 5** provide the basis information about the wheat cultivation characteristics in the ZD Vendolí. Sowing dates range from 26.9.2015 until 11.10.2015 in VS 2015/2016; from 22.9.2016 until 17.10.2016 in VS 2016/2017; from 28.9.2017 until 16.10.2017 in VS 2017/2018 and from 19.9.2018 until 27.9.2018 in VS 2018/2019. The utilized varieties also differ each season. For VS 2015/2016 were mostly used the varieties of Matchboll and Bohemia, while Balitus and Bohemia were mostly used in VE 2016/2017. The VS 2017/2018 mostly recorded the Grizzly and Balitus varieties. In the last season – VS 2018/2019 were mostly used varieties of Balitus, Elixer, and Bohemia. The wheat fields' total area was 256.47, 236.39, 286.4, and 248.4 hectares for vegetation seasons successively. The average yield ranged from 5.12 to 7.58 t.ha⁻¹ in VS 2015/2016, while for VS 2016/2017, it was from 4.82 to 10.97 t.ha⁻¹, for VS 2017/2018 it was from 6.5 to 9.18 t.ha⁻¹ and for VS 2017/2018 it ranged from 4.0 to 8.68 t.ha⁻¹.

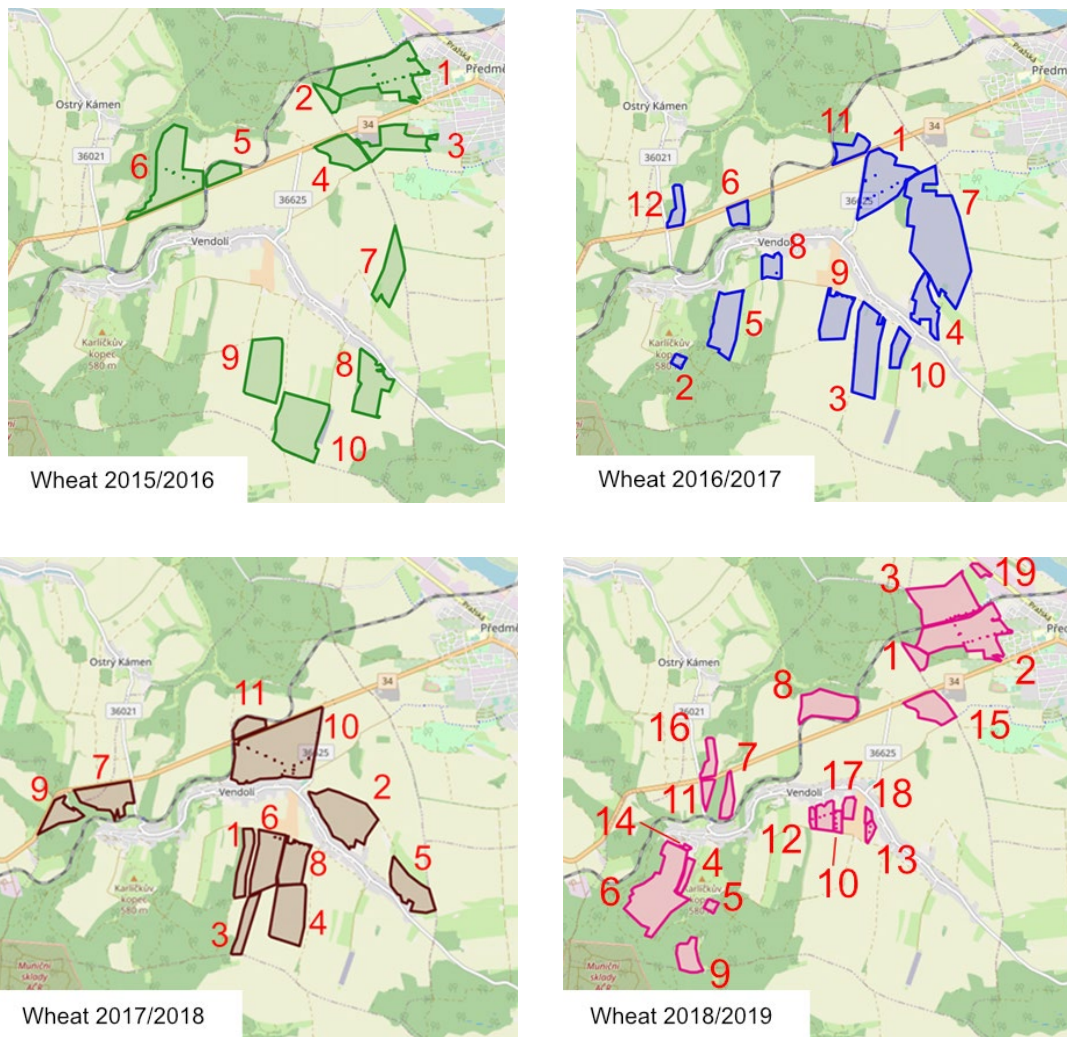


Figure 14. Cultivated wheat fields in main vegetation seasons (2015/2016, 2016/2017, 2017/2018 and 2018/2019) with Field ID

Table 2. Vegetation season 2015/2016 - Overview of wheat fields; variety; area and average yield

Field ID	Sowing date	Variety	Area [ha]	Avg. yield [t.ha ⁻¹]
1	7/10/2015	Matchboll	49.02	5.84
2	7/10/2015	Matchboll	6.09	5.84
3	2/10/2015	Bohemia	19.81	5.12
4	2/10/2015	Bohemia	17.47	6.89
5	4/10/2015	Bohemia	8.88	6.14
6	4/10/2015	Bohemia	42.55	6.35
7	11/10/2015	Matchboll	13.93	5.12
8	26/9/2015	Johny	24.36	6.63
9	8/10/2015	Matchboll	31.67	7.58
10	8/10/2015	Matchboll	42.69	7.36

Table 3. Vegetation season 2016/2017 - Overview of wheat fields; variety; area and average yield

Field ID	Sowing date	Variety	Area [ha]	Avg. yield [t.ha⁻¹]
1	25/9/2016	Balitus	35.79	8.13
2	7/10/2016	Balitus	2.29	4.82
3	11/10/2016	Bohemia	34.29	8.10
4	17/10/2016	Balitus	14.86	8.46
5	17/10/2016	Bohemia	24.69	8.42
6	7/10/2016	Balitus	6.40	7.76
7	26/9/2016	Fabius	68.06	8.03
8	15/10/2016	Bohemia	7.22	7.92
9	22/9/2016	Balitus	18.98	7.83
10	15/10/2016	Bohemia	7.84	10.97
11	8/10/2016	Bohemia	8.77	8.24
12	8/10/2016	Bohemia	7.20	8.11

Table 4. Vegetation season 2017/2018 - Overview of wheat fields; variety; area and average yield

Field ID	Sowing date	Variety	Area [ha]	Avg. yield [t.ha⁻¹]
1	2/10/2017	Grizzly	12.10	8.33
2	30/9/2017	Balitus	40.63	8.73
3	2/10/2017	Grizzly	11.78	7.55
4	1/10/2017	Balitus	31.67	8.05
5	28/9/2017	Balitus	21.44	9.18
6	2/10/2017	Grizzly	26.36	8.33
7	15/10/2017	Premiant	23.36	6.50
8	16/10/2017	Sacramento	18.98	6.56
9	15/10/2017	KWS Santiago	11.96	6.50
10	30/9/2017	Bohemia	79.29	6.71
11	30/9/2017	Balitus	8.83	6.82

Table 5. Vegetation season 2018/2019 - Overview of wheat fields; variety; area and average yield

Field ID	Sowing date	Variety	Area [ha]	Avg. yield [t.ha ⁻¹]
1	19/9/2018	Balitus	6.09	5.67
2	19/9/2018	Balitus	49.54	8.61
3	20/9/2018	Balitus	37.94	8.54
4	26/9/2018	Elixer	4.07	6.00
5	26/9/2018	Elixer	2.29	4.00
6	23/9/2018	Grizzly	51.92	6.40
7	27/9/2018	Elixer	7.41	5.38
8	21/9/2018	Bohemia	24.34	7.60
9	22/9/2018	Amandus	10.94	6.00
10	22/9/2018	Bohemia	3.33	7.00
11	27/9/2018	Elixer	4.48	8.68
12	21/9/2018	Bohemia	9.89	7.48
13	21/9/2018	Bohemia	2.49	6.77
14	26/9/2018	Elixer	0.77	6.40
15	20/9/2018	Bohemia	17.47	8.59
16	21/9/2018	Bohemia	7.19	5.26
17	21/9/2018	Bohemia	4.21	5.26
18	21/9/2018	Bohemia	1.70	6.77
19	20/9/2018	Balitus	2.44	8.54

The field measurements were carried out by ZD Vendolí's agronomist during the vegetation season (**Figure 15**). Data about the sowing, anthesis (flowering), and maturity of wheat on monitored fields were of the main interest. However, another phenological assessment of wheat canopy was carried out for calibration of the WOFOST crop model (**Table 10**). The values for sowing are displayed in **Tables 2, 3, 4,** and **5**. All other phenological phases were recorded by BBCH (Biologische Bundesanstalt, Bundessortenamt and Chemical industry). The standard phenological development of wheat is following:

- **BBCH 0–19:** September 30th - March 31st
- **BBCH 20–29:** April 1st - May 1st
- **BBCH 30–59:** May 1st - June 15th
- **BBCH 60–89:** June 16th – August 8th

Where 0 is dry seed sowing; 19 is the stage when wheat has 9 or more leaves unfolded; 20 is the stage when wheat starts to tiller; 29 is the end of tillering. The maximum number

of tillers detectable; 30 is the stage when wheat's stem elongation starts; 59 is the stage when a heading is finishing (inflorescence is completed); 60 is the stage when anthesis begins, and 89 is the stage when wheat has hard dough (grain hard, difficult to divide with thumbnail) (Lancashire et al. 1991). The other phenological assessment were discussed with agronomists – the parameters about the maximum relative increase in leaf area index (RGRLAI), life span of leaves growing at an average temperature of 35 °C (SPAN) and the lower threshold temperature for physiological ageing of leaves (TBASE). All values are recorded in **Table 10**.



Figure 15. Wheat field; year 2017, Field ID - 5

The wheat yield was measured by a combine harvester New Holland CR9080 equipped with a yield monitor and DGPS receiver with EGNOS correction. The accuracy of this system is $\pm 0.1-0.3$ m in horizontal and $\pm 0.2-0.6$ m in vertical direction. The yield data are recorded every 1 second with synchronized saving to the external memory. Failure on external memory caused the data losses in 2017. The yield data were processed by a basic statistical method to eliminate the errors of the yield measurement system. The yield data sets were then interpolated to kriging maps using experimental variograms. Details about yield data processing are more described in Kumhálová et al. (2011).

5.1.3 Remote sensing data

The satellites Sentinel-2 and Sentinel-1 from the Copernicus program – *Europe's eyes on Earth*, which is coordinated and managed by the European Commission and intended for monitoring environment on the Earth, were used for research (European Commission 2015). The Sentinel family of satellites of the Copernicus programme provides a very large scale of services due to several missions, which are monitoring the earth. While

Sentinel-1 is a radar-imaging mission intended for day and night monitoring of land and ocean independent of weather, Sentinel-2 is a multispectral high-resolution imaging mission for land monitoring with a focus on vegetation imagery or soil and water cover and others (ESA 2018).

Freely accessible Sentinel-2 and Sentinel-1 satellite images were obtained from the Copernicus Open Access Hub (SciHub) provided by ESA, the Alaska Satellite Facility within the Geophysical Institute at the University of Alaska Fairbanks and Collaborative Ground Segment - Czech Republic (accessible via <https://dhr1.cesnet.cz/#/home>). Sentinel-1 images were obtained on two platforms – Sentinel-1A and Sentinel-1B. The Sentinel-1A data started to be available systematically from 14.04.2016, while Sentinel-1B data started to be available systematically from 26.09.2016. The initial number of downloaded images was 44 for 2016, 92 for 2017, 87 for 2018, and 89 for 2019 (**Table 1**); however, during the processing and analysis, 2 images from 2016 and one image from 2019 were corrupted. All others were used for further analysis. The Sentinel-1 was downloaded in the form of Ground Range Detected (GRD). According to the satellite imagery metadata, the SAR instrument on the satellite operates at a central frequency of 5.405 GHz (C-band) and provides Interferometric Wide mode (IW) with dual-polarization - VH; VV. The spatial resolution of IW images is 5 x 20 m over a 250 km wide swath. The area of Vendolí was monitored from 3 Relative orbits (i.e., numerical order of Sentinel-1's 175 orbits per cycle) (**Figure 13**), namely 124, 73, 22 with Descending, Ascending and Descending pass directions. The range of Incidence angle was approximately between 30.38 and 45.90 ° for 124, 30.24 and 46.14 ° for 73 and from 30.24 to 46.18 ° for 22 (Copernicus not dated - b).

The Sentinel-2 images were also obtained from two platforms – Sentinel-2A and Sentinel-2B. While the Sentinel-2A was launched 23.06.2015, the Sentinel-2B was launched 7.3.2017. A number of downloaded images was 3 images for 2016, 5 images for 2017, 2 images for 2018, and 8 images for the year 2019. The decision was made not to use the images with a high percentage of cloud cover as the processing of such images could be time-consuming without the possibility to do it semi-automatically or fully automatically. The Sentinel-2 images were downloaded in the form of Level-1C (Top-Of-Atmosphere reflectances in cartographic geometry) for 2016 images and Level-2A (Bottom-Of-

Atmosphere reflectances in cartographic geometry) for rest of images. The Sentinel-2's bands and their resolutions can be seen in **Table 6**.

Table 6. Sentinel-2 band characteristics – resolution and spectral bands. (Source: ESA 2015)

Sentinel-2 Bands	Central Wavelength (µm)	Resolution (m)
Band 1 - Coastal aerosol	0.443	60
Band 2 – Blue	0.490	10
Band 3 – Green	0.560	10
Band 4 – Red	0.665	10
Band 5 - Vegetation Red Edge	0.705	20
Band 6 - Vegetation Red Edge	0.740	20
Band 7 - Vegetation Red Edge	0.783	20
Band 8 – NIR	0.842	10
Band 8A – Vegetation Red Edge	0.865	20
Band 9 - Water vapour	0.945	60
Band 10 - SWIR – Cirrus	1.375	60
Band 11 – SWIR	1.610	20
Band 12 – SWIR	2.190	20

The scientific paper - *The Noise-reduction Potential of Radar Vegetation Index for Crop Management in the Czech Republic* examined the possibilities to use Radar Vegetation Index for monitoring vegetation development by comparison with optical data in the same research area, however for time 2015 – 2018. The methodology and goals of the paper were overlapping with the methodology and goals of this research, and obtained outcomes will be presented later in the text and were used during this research. However, there were several different approaches during the research, which will be further described. Although the research used the exact same approach for Sentinel-1, the optical data involved the use of Landsat 7, 8 satellite images for 2015 and 2016, when Sentinel-2 data was not provided or were scarce. From 2017, Sentinel-2 images were already used as the only source of optical data (Tůma et al. 2021). Unfortunately, the use of Landsat 7, 8 for LAI is not possible by the methods chosen during this research as software contains bugs (errors), making it impossible to estimate LAI.

5.1.4 Climate data

The climate data for this study are taken from NASA POWER database. NASA POWER is a frequently used source of data for crop growth modelers (Bai et al. 2010; Duarte & Sentelhas 2020; Ojeda et al. 2017; Wart et al. 2013; Wart et al. 2015; de Wit et al. 2017; Koo 2012). NASA POWER database is service, which provides mean daily values of the base meteorological and solar data in timeseries format. The data are the result of weather modelling and satellite observation and can successfully and accurately substitute missing meteorological data over regions with surface measurement scarcity. The resulting weather data are promoted as user-friendly with a possibility to access these data via a user-friendly web portal without the necessity to understand large data archives. The POWER aggregates three specific components - Surface meteorology and Solar Energy, Sustainable Building, and Agroclimatology into one data portal.

The meteorological data are based on Modern Era Retrospective-Analysis for Research and Applications (MERRA-2) assimilation model products and Goddard's Global Modeling and Assimilation Office Forward Processing, while solar based data/parameters are based upon satellite observations with subsequent inversion to surface solar insolation by NASA's Global Energy and Water Exchange Project and NASA's CERES Fast Longwave and Shortwave Radiative project. The weather and solar data are distributed in spatial resolution of 1.0° latitude by 1.0° longitude for the radiation datasets and ½° latitude by ⅝° longitude for the meteorological datasets (POWER Project Team not dated). Daily data are available from 1983 to the present. The validation of NASA POWER results can be found in *valuation of NASA satellite- and assimilation model-derived long-term daily temperature data over the continental US* (White et al. 2008) published in *Agricultural and Forest Meteorology* journal or in *Evaluation of NASA Satellite- and Model-Derived Weather Data for Simulation of Maize Yield Potential in China* (Bai et al. 2010) published in *Agronomy Journal*.

Desired meteorological and solar radiation variables for crop modelling are presented in **Table 7**. Data for years 2016, 2017, 2018, and 2019 were downloaded from NASA POWER by application programming interface (API) via Python Crop Simulation Environment (PCSE) for research site's coordinates, processed by data wrangling (e.g., unit change), and prepared for later crop modelling.

Table 7. Weather input data for the WOFOST model. (Source: Kraalingen et al. 1997)

Weather data – name	Time period	Unit
Global radiation	Daily total	$\text{kJ.m}^{-2}.\text{d}^{-1}$
Minimum air temperature	Daily minimum	$^{\circ}\text{C}$
Maximum air temperature	Daily maximum	$^{\circ}\text{C}$
Vapour pressure	Daily average	kPa
Wind speed	Daily average	m.s^{-1}
Rain/Precipitation	Daily total	mm.d^{-1}

5.1.5 Soil data

Soil data is essential input parameter for crop modelling with WOFOST. It affects the water balance by physical soil characteristics. Water retention, hydraulic conductivity, and workability are needed for the calculation of water balance on a daily basis. This is necessary for the simulation of water-limited growth (see **chapter 2.1**). However, the chemical soil properties are not included in the WOFOST's soil input data. The European Community (EC) is commonly used during the WOFOST modelling and was also chosen for this research. EC soil data files are distributed with WOFOST and can be used immediately (Boogaard et al. 2014).

The soil information was obtained from Soilgrids database powered by International Soil Reference and Information Centre (ISRIC). Soilgrids is a global digital soil mapping that uses machine learning methods to map soil properties. The machine learning was trained on data of 230 000 soil observations originated from the World Soil Information Service database and environmental covariates based on climate, land cover and terrain morphology, and other environmental information. The outcome is a global soil map with six layers representing six standard depths ranges with a spatial resolution of 250 m. The relevant soil properties for crop modelling were sand content, silt content and clay content (ISRIC Not dated; Hengl et al. 2017).

All relevant grids over the research site at six depths were observed and recorded. For the selection of the soil was use set of rules found in *Crop production potential of rural areas within the European Communities 111: Soils, Climate, and Administrative Regions* by Reinds et al. (1992) as follows:

1. **Coarse:** more than 65 % sand and less than 18 % clay.
2. **Medium:** more than 15 % sand and less than 35 % clay; more than 18 % clay if the sand content exceeds 65 %.
3. **Medium fine:** less than 15 % sand and less than 35 % clay.
4. **Fine:** more than 35 % clay but less than 60 % clay.
5. **Very fine:** more than 60 % clay.

Since the observation and records discovered that all grids for the research area can be classified as Medium EC, it was not taken any more steps (e.g., interpolation or averaging), and default soil file EC2.soil (**Figure 16**) was chosen as soil input for crop modelling for whole research site area. Since no data were collected/found for the maximum soil rootable depth [cm] (RDMSOL), it was made an assumption there are no limits for the wheat root system, and a value of 200 cm was set up in EC2.soil. This value is not restricting the growth of the wheat roots.

```

** EC2-medium
SOLNAM='EC2-medium'
** physical soil characteristics
** soil water retention
SMTAB = -1.000, 0.390, ! vol. soil moisture content
        1.000, 0.361, ! as function of pF [log (cm); cm3 cm-3]
        1.300, 0.353,
        1.491, 0.346,
        2.000, 0.309,
        2.400, 0.260,
        2.700, 0.216,
        3.400, 0.134,
        4.204, 0.099,
        6.000, 0.090
SMW    = 0.099 ! soil moisture content at wilting point [cm3/cm3]
SMFCF  = 0.272 ! soil moisture content at field capacity [cm3/cm3]
SM0    = 0.390 ! soil moisture content at saturation [cm3/cm3]
CRAIRC = 0.075 ! critical soil air content for aeration [cm3/cm3]
** hydraulic conductivity
CONTAB = 0.000, 1.380, ! 10-log hydraulic conductivity
        1.000, 0.312, ! as function of pF [log (cm); log (cm/day)]
        1.300, 0.000,
        1.491, -0.268,
        1.700, -0.538,
        2.000, -1.114,
        2.400, -1.699,
        2.700, -2.658,
        3.000, -3.092,
        3.400, -3.620,
        3.700, -4.009,
        4.000, -4.377,
        4.204, -4.638
K0     = 23.988 ! hydraulic conductivity of saturated soil [cm day-1]
SOPE   = 1.32  ! maximum percolation rate root zone[cm day-1]
KSUB   = 2.05  ! maximum percolation rate subsoil [cm day-1]
RDMSOL = 200  ! maximum soil rootable depth [cm]

** soil workability parameters
SPADS  = 0.300 ! 1st topsoil seepage parameter deep seedbed
SPODS  = 0.035 ! 2nd topsoil seepage parameter deep seedbed
SPASS  = 0.400 ! 1st topsoil seepage parameter shallow seedbed
SPOSS  = 0.060 ! 2nd topsoil seepage parameter shallow seedbed
DEFLIM = -0.200 ! required moisture deficit deep seedbed

```

Figure 16. The European Community medium soil's (EC2-medium) parameters.

5.2 Remote sensing data processing and analysis

5.2.1 Sentinel-2 data processing and analysis

The data processing and analysis of 18 Sentinel-2 images started with pre-processing of that Sentinel-2 images (year 2016), which were in the format of Level-1C (Top of Atmosphere). This pre-processing was done by Sen2cor software applying a scene classification, an atmospheric correction, and conversion to Bottom-Of-Atmosphere (BOA) reflectance product resulting in Level-2A product. Images from the year 2017, 2018, and 2019 were already corrected by the provider and freely accessible (Mueller-Wilm 2020). The pre-processing step also contained resampling of Sentinel-2 products to a resolution of 10 meters for all bands (bands characteristics in **Table 6**). As it was already mentioned, pre-processing didn't involve any cloud masking for LAI estimation analysis.

The analysis of Sentinel-2 data used the Biophysical processor (**Table 8**) implemented into the SNAP software. This processor provides the estimates of biophysical variables such as LAI, a fraction of absorbed photosynthetically active Radiation, Fraction of vegetation cover, Canopy Water Content, or Chlorophyll content in the leaves. These indices (outputs) are based upon algorithms, which have been scientifically proven to be efficient and have been generated for satellite data from other satellites (e.g., LANDSAT, MERIS, SPOT). The neural networks are used in the process of canopy characteristics estimation according to the top of canopy reflectances (TOC reflectance) and the observational configuration (Weiss & Baret 2016).

The LAI products were subsequently cropped by SNAP's subset function to a smaller size image containing only the research area with North latitude bound equal to 49.783, West longitude bound equal to 16.533, South latitude bound equal to 49.703, and East longitude bound equal to 16.261. After that, satellite images were converted from SNAP native format to Geographic Tagged Image File Format (GeoTIFF) format. After that, all GeoTIFF images were processed in Python programming language with supporting libraries (listed in section 5.8). Sentinel-2 GeoTIFF subsets were then converted to NumPy (Numerical Python) array, resampled, and interpolated to match Sentinel-1 coordinates by function *scipy.interpolate.griddata* with the method of linear interpolation in SciPy (Scientific Python)(Virtanen et al. 2020). As the “master” image with points (coordinates) at which satellite images were interpolated, was chosen first Sentinel-1 image in timeseries with date 1.3.2016. After the resampling and interpolation, the LAI products were cropped by the Geographic Information System (GIS) shapefiles (see delineation in **Figure 14**) (.shp) delineating wheat fields. In the final step, descriptive statistics and figures were created for LAI results.

From the perspective of *Tũma et al. 2021*, The optical data analysis was using pre-processing methods - The atmospheric correction of Fast Line-of-Sight Atmospheric Analysis of Hypercubes (FLAASH) for Landsat images with the aim of converting data to surface reflectance (Domínguez et al. 2017). A masking algorithm was used to mask cloud cover. The NDVI results were then calculated using the standard formula (**Table 8**). The bands used for the calculation of NDVI were Bands 3 and 4 in the case of Landsat 7, bands 4 and 5 in the case of Landsat 8, and Bands 4 and 8 in the case of Sentinel-2.

5.2.2 Sentinel-1 data processing and analysis

The Sentinel-1 data processing started with pre-processing steps, which can be observed in **Figure 17**. The first step, after downloading Sentinel-1 images, was applying cropping to reduce the size of the image. The same options were used as for Sentinel-2 described above in **chapter 5.2.1**. After that, applying of Orbit file was done. This pre-processing step tries to find more precise orbit files in online databases to provide more accurate satellite position and velocity information. The orbit state vectors in the satellite image metadata can be updated based on such information. The precise orbit files are generally available with some latency after the availability of the Sentinel-1 product. The Thermal Noise Removal is a method for correction of GRD products with noise Look-Up Table (LUT), particularly in the cross-polarization channel. This method is useful for the normalization of a backscatter signal. The next step was dealing with Border Noise Removal, which corrects invalid data and removes low intensity noise on Sentinel-1 imagery borders.

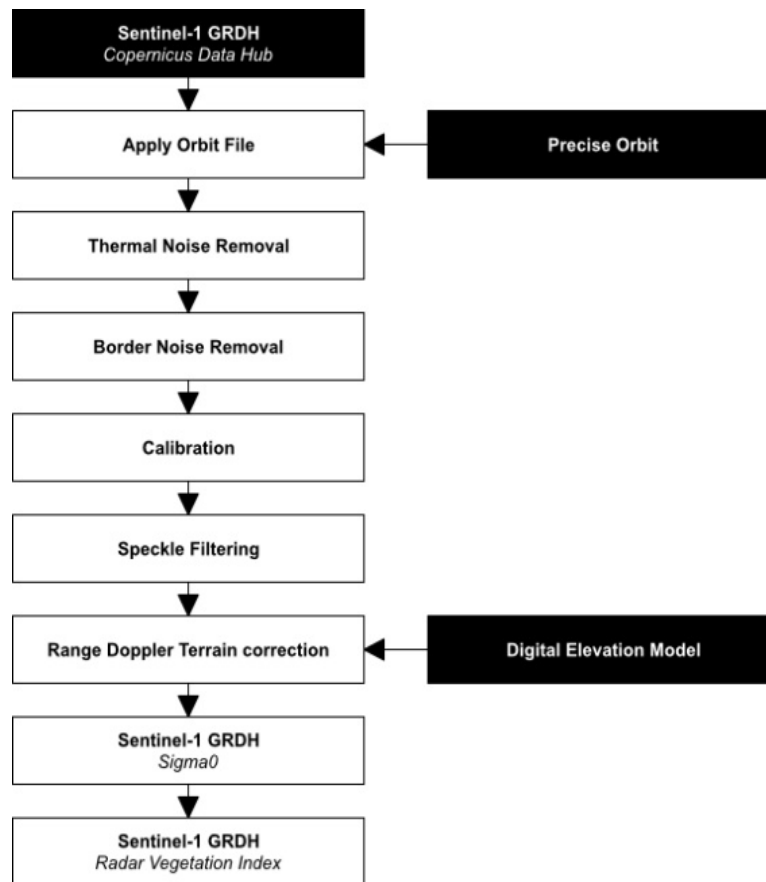


Figure 17. Sentinel-1 Ground Range Detected (GRD) pre-processing and processing workflow. (Source: adjusted from Filipponi 2019)

The calibration part was the next step for converting values of pixels to radiometrically calibrated SAR backscatter. Sigma nought (σ^0) backscatter was result of conversion scene intensity values and can be described as the conventional measure of the strength of radar signals reflected by a distributed scatterer. After the calibration, the Speckle Filtering takes place. This method tries to suppress so-called Speckle – granular noise/ interference incoming from many elementary scatterers as a result of surface roughness variability. Such a procedure can be beneficial for the quality of an image. There are several speckle filtering methods (e.g., Boxcar, Gamma Map, Lee, Refined Lee or Lee Sigma). During this research, the Lee Sigma filtering was used as it is the default speckle filtering process. Parameters were as follows: number of looks 1; window size 7x7; sigma 0.9 and arget window size 3x3. The last pre-processing step applies Range Doppler Terrain correction, which compensates for the scene distortion caused by side-looking geometry (i.e., viewing angle is greater than 0 degrees). After this process, the Sentinel-1 image should be close as possible to the real-world visualization with a resolution of 10 meters. All these preprocessing steps were done in SNAP software with the help of the Batch Processing tool (Copernicus not dated - a; Filipponi 2019; Jurkevich & Lee 1994, Lee and Pottier, 2009). The Radar Vegetation Index was calculated directly from pre-processed images using the band math in SNAP tool and Batch Processing tool for automatic processing of products. The formula presented by Charoboneau et al. (2005) can be seen in **Table 8**. Sigma nought with VV polarization and VH cross-polarization was used for the calculation of RVI.

Table 8. Overview of used vegetation indices in this study. (Source: adjusted from Tůma et al. 2021)

Spectral Index	Algorithm	References
Normalized Difference Vegetation Index (NDVI)	$(\text{NIR}-\text{RED})/(\text{NIR}+\text{RED})$	Rouse et al. 1974
Radar Vegetation Index (RVI)	$(4\sigma^0\text{VH})/(\sigma^0\text{VV}+\sigma^0\text{VH})$	Trudel et al. 2012 (based on Kim & van Zyl 2009)
Leaf Area Index (LAI)	Neural Network (SNAP - Biophysical processor)	Weiss & Baret 2016

NIR = near infrared reflectance; RED = red reflectance; σ^0 - backscatter coefficient (sigma nought); VH – polarization mode Vertical/Horizontal; VV - polarization mode Vertical/Vertical

RVI products were subsequently converted to GeoTIFF by SNAP. The next analysis was done by Python programming language with supporting libraries (listed in section 5.6). The first step was an interpolation of RVI products, which were all resampled and interpolated, (Travis Oliphant, Pearu Peterson, and others) to match coordinates of first Sentinel-1 image in timeseries with date 1.3.2016 likewise the Sentinel-2 products described in **chapter 5.2.1**. After that, the application of Savitzky-Golay filter was performed. This decision was based on results from *Tũma et al. 2021*, which describes the impact of Relative orbits on RVI development. All these findings are thoroughly described in chapter 6.1. The Savitzky-Golay (S–G) filter (Savitzky & Golay 1964; Virtanen et al. 2020) was used successfully during several remote sensing analyses (Cai et al. 2017, Chen et al. 2004; Huang et al. 2014). The simple methodological approach was utilized when the S–G filter was applied on stacked RVI products for every vegetation season. The stacking of images was done by NumPy. After that, every array was filtered by S–G filter in SciPy, resulting in the adjustment of every single pixel in stacked RVI timeseries. The setting of the S–G filter parameters (window length and polyorder) were chosen for suppressing the negative impact of Relative orbits (presented in **Results and Discussion – 6.2**). The final step was cropping the scenes by the GIS shapefiles of wheat fields.

From the perspective of *Tũma et al. 2021*, the RVI results were tested against estimated NDVI values from optical satellite imagery for every field and every date with simple linear regression and coefficient of determination by Scikit-Learn and Statsmodels to define the relation.

5.3 Machine learning prediction of Leaf Area Index

5.3.1 Preparation of data

The Machine learning methodological part dealt with the prediction of LAI from Sentinel-1 data. The supervised learning was used for the finding the desired solutions. The supervised learning is generally based on sets of *features* and a set of *predictors*. *Features* are values of some attribute (data type) and this attribute, while *predictors* are *target* values. Such training set is used by the Machine learning algorithm to try to find desired solution (Géron 2019).

As the *features* for this research, values of RVIs from Sentinel-1 were used, while the *predictors* will be the LAIs estimated by SNAP software from Sentinel-2. Since both sources of datasets were stored in GeoTIFF after the actions described in **chapter 5.2**, data “*wrangling*” in python had to be done before the launch of Machine learning.

The first step dealt with the conversion of RVI and LAI GeoTIFF images to Comma-separated values (CSV) files according to the date of observation and Field ID. The conversion was done in Python and its libraries. 277 csv files were created for LAI products, while 3420 files were created for RVI products. The next dealt with the search of the closest csv files between the RVI and LAI. This match procedure was based upon the Python/Pandas function *pandas.merge_asof* and dates of observations. The result table for the matching dates can be found in chapter 6.4. 277 csv files of LAIs found a match in RVI dataset. Matched data were loaded to dataframes, subsequently to flatten arrays, and merged. The final dataframe (**Figure 18**) contained samples with $n = 568659$. The Pearson pairwise correlation coefficient was calculated between the RVI and LAI for all data and for every vegetation season (year). In this part of the work, dataframe for *features* (RVI) was also prepared by a similar approach; however without the matching and merging with LAI data. The final RVI dataframe contained samples with $n = 10337601$. The structure of the dataframe was similar, as can be seen in **Figure 18**; however, without LAI values and with the date of observations for Sentinel-1.

	LAI	RVI	filename	shapefile	date	year	month
568659	0.353702	0.614153	RVI_LAI_20190725_9.csv	9	2019-07-25	2019	Jul

Figure 18. Final structure of dataframe; Tail of data; Shapefile is unique ID for wheat field, date of record is date of Sentinel-2 monitoring.

5.3.2 Random Forest Regression

The prepared data in the final dataframe were analysed by Supervised machine learning. As the method was chosen Random Forrest Regression (RFR). Several papers find Random Forrest Regressor successful in estimating biomass or LAI (Li et al. 2020; Sibanda et al. 2021; Wang et al. 2016; Zhu et al. 2019). The initial task dealt with finding optimal hyperparameters, the so-called Hyperparameter tuning for optimizing performance. Hyperparameters need to be set before the training of the model, which will

then learn model parameters during the training. Hyperparameters are described by Pedregosa et al. (2011) as follows:

- **Number of estimators** - The number of trees in the forest.
- **Maximum depth** - The maximum depth of the tree.
- **Minimum samples split** - The minimum number of samples required to split an internal node.
- **Minimum samples leaf** - The minimum number of samples required to be at a leaf node.
- **Max features** - The number of features to consider when looking for the best split
- **Bootstrap** - Whether bootstrap samples are used when building trees. If False, the whole dataset is used to build each tree (Pedregosa et al. 2011).

For the first runs, the number of estimators was set up according to Probst et al. (2018) (i.e., 500), and other parameters were chosen randomly within the limit described in Koehrsen 2018. The first run served for the creation of a Randomized Search frame, as can be seen in **Table 9**. Randomized Search is a method using the cross-validated search over hyperparameters settings. However, not all parameters are tested in Randomized Search. The only specific number of combinations is sampled. In this research, it was used 100 combinations. The random search model with RFR was then performed according to the standard conditions. *Features* (RVI) and *predictors* (LAI) were split into the training set with size 0.7 and the test set with size 0.3; then the model was launched. After specific settings of hyperparameters were found (see Results and Discussion - 6.4) by Randomized Search, the Grid search with RFR was performed for even more accurate hyper parameter settings. Contrary to Randomized Search, the Grid search use exhaustive search over the selected options of hyperparameters (**Table 9**). The final settings of RFR's hyperparameters can be observed in Results and Discussion - 6.4 (Géron 2019; Pedregosa et al. 2011).

Table 9. Randomized search and Grid search for optimal hyperparameters of the Random Forest Regression

	Randomized search	Grid search
Number of estimators	[200, 300, 400, 500, 600, 700, 800]	[400, 500, 600]
Max features	['auto', 'sqrt']	['sqrt']
Max depth	[1, 2, 3, 4, 5, 6, 7, 8, 9, 10, 11, 12, 13, 14, 15, 16, 17, 18, 19, 20, None]	[3, 4, 5, 6, 7]
Minimum samples split	[2, 5, 10]	[9, 10, 11]
Minimum samples leaf	[0, 1, 2, 3, 4]	[0, 1, 2]
Bootstrap	[True, False]	[True]

In the final step, the RFR was launched with S–G filtered data and non-filtered data. The accuracy of the model was measured by the coefficient of determination (R^2) of the prediction. The R^2 is defined as follows:

$$1 - \frac{u}{v} \quad (5.01)$$

Where u is the residual sum of squares:

$$\sum(y_{true} - y_{pred})^2 \quad (5.02)$$

And v is the total sum of squares:

$$\sum(y_{true} - \overline{y_{true}})^2 \quad (5.03)$$

The best possible value of the score is 1.0, and it can be negative. The score with a value of 0.0 indicates that the model always predicts the expected value of the predictor (Pedregosa et al. 2011). Finally, the LAI from RVI (calling it - R-LAI) was predicted from the final RVI dataframe for every possible RVI value.

5.4 WOFOST - Crop growth modelling

5.4.1 Calibration and run of crop growth model

The important part of the research was the calibration of the WOFOST. Since the performance of the crop growth model in simulation growth and yield forecasting depends on the ability of the model to reproduce impacts of environmental conditions and crop parameters (Djaby et al. 2013). The definition of calibration described in Kersebaum et al. (2015) understand calibration as the adaptation process of parameters or relations of the model according to the measurable (real) background.

As the type of simulation, the water-limited was chosen (see **Figure 2; chapter 2.1**). Firstly, the initial soil moisture for the chosen research site has been set up according to the data about Volumetric soil moisture from Soil moisture gridded data provided by Copernicus' Climate Data Store (CDS, 2021). Secondly, parameters and attributes of the simulated crop (wheat) were adjusted according to the field observations in the wheat input file. Parameters about phenological development (e.g., maximum relative increase in leaf area index) are essential for precise estimation of simulated growth and final yield forecasting by the WOFOST. **Table 10** shows the crop parameters used for calibration of the model (via the creation of wheat variety). Thirdly, the agromanagement settings were created. These settings are providing parameters about crop start type, start date, crop end date type, maximum duration of simulation, crop, and crop variety. The crop start type was set up on *sowing*, and the crop end type was set up on *maturity*, maximum duration of the simulation was set up on 500 days. The crop was set up to wheat plant type and crop variety to variety created previously. The weather data were used data described in 5.1.2.3 (Djaby et al. 2013). Finally, 52 simulations were performed for sowing dates described earlier, and results with crop growth development were saved in excel files for later analysis. The results contain daily values for every day of crop growth from the day of sowing until the day of maturity. The structure of obtained results can be seen in **Table 11**.

Table 10. WOFOST's crop specific parameter values used for calibration.

Parameter	Description	Units	Value	Source
DLO	Optimum day length for development	h	20	Day length in anthesis phase
TSUM1	Threshold temperature sum from emergence to anthesis	°C	450	Meteorological data
TSUM2	Threshold temperature sum from anthesis to maturity	°C	1400	Meteorological data
RGRLAI	Maximum relative increase in leaf area index	ha.ha ⁻¹ .d ⁻¹	0.032	Field observation
SPAN	Life span of leaves growing at an average temperature of 35 °C	d	20	Field observation
TBASE	Lower threshold temperature for physiological ageing of leaves	°C	3.0	Field observation

Table 11. WOFOST's structure of daily outcomes from crop simulation.

Parameter	Variable	Units
Day	Day	date
DVS	Development stage	-
LAI	Leaf Area Index	m ² .m ⁻²
TAGP	Total above-ground production (dead and living plants organs)	kg.ha ⁻¹
TWSO	Total weight of storage organs	kg.ha ⁻¹
TWL	Total dry weight of leaves (dead and living)	kg.ha ⁻¹
TWST	Total dry weight of leaves (dead and living)	kg.ha ⁻¹
TWRT	Total dry weight of roots (dead and living)	kg.ha ⁻¹
TRA	Transpiration rate	mm.day ⁻¹
RD	Current rooting depth	cm
SM	Volumetric soil moisture content	-
WWLOW	Total amount of water in the soil profile	cm

5.4.2 Assimilation of satellite data to the WOFOST

The assimilation process started with data wrangling in Python. All R-LAI results from 2016 to 2019 were separated into files according to the monitored years. Data were then grouped according to the shapefile (Field ID) and date. The average R-LAI was calculated for every observed field and date.

The assimilation process of LAI data and R-LAI was done with Ensemble Kalman Filter (EnKF). This method has had many utilizations in crop growth modelling (Bai et al. 2019; Ma et al. 2013b; de Wit & van Diepen 2007; Zhang et al. 2016). The EnKF uses an ensemble of model predictions to provide an estimation of the error values used by the Kalman Filter for the updates of model-simulated values by the observation values (Crow

& Wood 2003). The calculation of updated LAI from remotely sensed data and simulated data will be based upon the following assumptions of a linear Gaussian state-space model for discrete time points $t=1, 2, 3, \dots$:

$$x_t = M_t * x_{t-1}^{actualized} + w_t, \quad w_t \sim N(0, Q_t) \quad (5.04)$$

Where x_t is the unobserved (simulated) estimates/state variable of interest, x_{t-1} is filtering distribution of previous time, M_t is covariance matrix of model operator, and w_t is model error representing model uncertainties. The w_t assumes the Gaussian distribution of zero mean and the covariance matrix Q_t . Given the specific number of ensemble members N , the mean value of the ensemble's state variable is calculated:

$$\bar{X}_t = \frac{1}{N} \sum_{i=1}^N X_{i,t} \quad (5.05)$$

The subsequently, the Ensemble covariance matrix of the ensemble's simulated state variable P_t is calculated as follows:

$$P_t = \frac{1}{N-1} \sum_{i=1}^N (x_{i,t} - \bar{X}_t)(x_{i,t} - \bar{X}_t)^T \quad (5.06)$$

A similar step is created for observed estimates/state vector of interest, starting with mean of ensemble's observed state variable:

$$\bar{b}_t = \frac{1}{N} \sum_{i=1}^N b_{i,t} \quad (5.07)$$

$$R_t = \frac{1}{N-1} \sum_{i=1}^N (b_{i,t} - \bar{b}_t)(b_{i,t} - \bar{b}_t)^T \quad (5.08)$$

Where R_t is the covariance of the observation ensemble. The observation model is expressed by the following equation:

$$y_t = H_t * x_t + v_t, \quad v_t \sim N(0, R_t) \quad (5.09)$$

Where H_t is the observation measurement operator matrix. The x_t is the state vector, and v_t is the observation error assuming the Gaussian distribution of zero mean and the covariance matrix R_t . The observation data is then assimilated into the model, updating the state variable of each ensemble member of simulation by the following equation:

$$x_t^{actualized} = x_t + K_t[y_t - H_t(x_t)] \quad (5.10)$$

Where K_t is the Kalman gain time at a given time, and it is calculated as follows:

$$K_t = P_t H_t^T (H_t P_t H_t^T + R_t)^{-1} \quad (5.11)$$

Where H^T is the inverse matrix of H . Given model at time t , the state variable of each ensemble is updated by observation data. This process is repeated with all following observations same way (Katzfuss et al. 2016; Ma et al. 2013b; Pan et al. 2019).

As it was already mentioned, the LAI was the state variable for ENKF assimilation. This variable needs to be provided with the error of observation. Based on the work of Pan et al. (2019), the error of LAI observation was set at 10 %, while the error of R-LAI was set at 20 % due to the small accuracy of the RFR model (i.e., 52 %). Then the ensemble size was chosen to be $n = 50$. The initial total crop dry weight (TDWI), initial soil water content (WAV), life span of leaves growing at 35 Celsius (SPAN), maximum relative increase in LAI (RGRLAI), and the field capacity of the soil (SMFCF) were chosen to be initial variables and parameters defining the uncertainties of model. These values were chosen according to the discussion with ZD Vendolí's agronomist and the work of Wang et al. 2013. These five parameters were treated as Gaussian random variables with a mean equal to a default (calibrated) values and standard deviations setup created from information obtained from ZD Vendolí's agronomist. The EnKF updated the LAI values of every ensemble member in LAI or R-LAI observation time. The entire process can be seen in **Figure 19**. The data assimilation process was tested for assimilation of LAI from Sentinel-2 and then for assimilation of R-LAI from Sentinel-1. The results are presented in **chapter 6.6**.

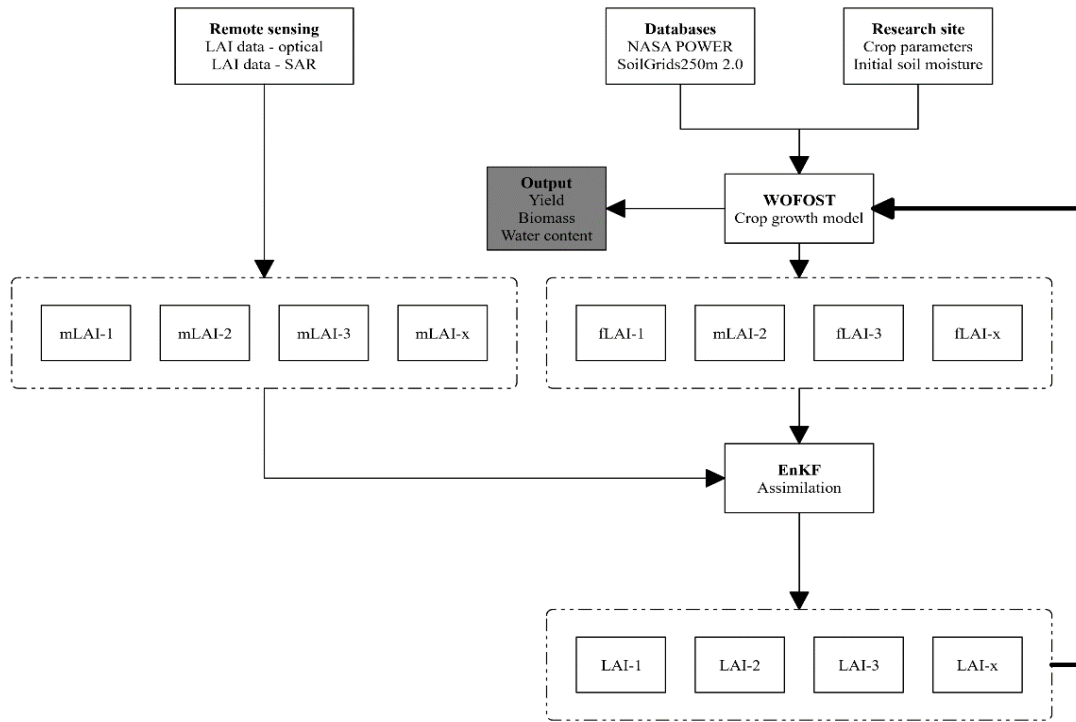


Figure 19. EnKF data assimilation – general overview.

5.5 Statistical assessment of crop modelling accuracy

The root mean square error (RMSE) and the mean absolute error (MAE) were used to measure of the simulation’s and EnKF simulation’s accuracy. These two statistical metrics are regularly used in model studies. Since both measurements have positive and negative characteristics, both were used for the comparison of errors of different data assimilation scenarios. While the RMSE is the preferred measure for the performance of models and corresponds to the *Euclidean norm*, the MAE corresponds to the “*Manhattan norm*” (ℓ_1). Generally, the RMSE is more sensitive to outliers than the MAE. The data assimilation methods in crop modelling are usually using RMSE or MAE for the final evaluation. The calculations of the RMSE for n samples is as follows:

$$RMSE = \sqrt{\frac{1}{n} \sum_{i=1}^n (O_i - S_i)^2} \quad (5.12)$$

Where O_i are observations and S_i are predicted values. The MAE is given as:

$$MAE = \frac{1}{n} \sum_{i=1}^n |O_i - S_i| \quad (5.13)$$

The RMSE and MAE were calculated via Python (and Scikit-learn) between the measured yield and crop modelling forecasts, between the measured yield and crop modelling forecast using EnKF of LAI, and between the measured yield and crop modelling forecast using EnKF of R-LAI (Bai et al. 2019, Chai & Draxler 2014; Cheng et al. 2020; Géron 2019; Ma et al. 2013, Tripathy & Prusty 2021).

During the entire data processing and analysis, the auxiliary statistical methods were used, mostly descriptive statistics. For these approaches, the pandas and statsmodels were used (McKinney 2010; Seabold & Perktold 2010).

5.6 Software and data processing tools

The last chapter of methodology summarizes all used software and processing tools, which were used during the research.

The analysis of Remote sensing data was carried out mainly in SNAP software provided by the ESA. The software is freely usable, and it provides a sufficient environment for both radar and optical imagery data. The software contains an abundance of pre-processing tools necessary for research such as radiometric correction, reflectance to radiance algorithm, terrain correction, or radiometric calibration, but also processing tools such as analytical tools for vegetation and soil analysis or classification algorithms. The crucial tool for the research was a Biophysical processor for LAI estimation and Band math tool for RVI (STEP 2018). The Sen2-Cor software was used for the conversion of Sentinel-2 Level-1C images to Sentinel-2 Level-2A products. The ENVI software was used for F-mask cloud masking, FLAASH, and calculation of NDVI. For the visualization of GIS files or satellite imagery as well as creation of shapefiles and zonal statistics were used QGIS and ArcGIS softwares (Tuma et al. 2021).

The Python Crop Simulation Environment was applied as a basic environment for crop modelling with the WOFOST (more in the Literature review). For the machine learning and statistical assessment (i.e., RMSE and MAE), the Scikit-learn library for Python was used. The Pandas, SciPy, and NumPy Python's libraries were used for general data wrangling with dataframes or numerical arrays. These libraries also provided some data analysis and statistical tools as described earlier. For GIS data manipulation and processing, these Python's libraries were used – GDAL (The Geospatial Data Abstraction Library), Geopandas, Rasterio, Rasterstats, Rioxarray, Shapely, and Xarray. For the

visualization of figures, the Matplotlib and Altair python libraries were used. The HoloViews and Folium were used in some cases of visualization of GIS data. Finally, some statistics were computed by statsmodels.

6. Results and Discussion

6.1 NDVI and RVI results

6.1.1 NDVI results

The following results were published in *Tůma et al. 2021*. The results of NDVI for wheat calculated are shown in **Figure 20** from 2015 to 2018. Since there was a day with cloud cover over the monitored fields, some results are missing. The noise in NDVI results was probably caused by varying atmospheric conditions and viewing geometries between sun-surface-sensor, as described in Hoblen and Fraser, 1984; Gutman, 1991; Goward et al., 1991, and more thoroughly described in Hird and McDermid (2009). The initial values varied between 0.25 and 0.85; peak values near 1 and final values ranged between 0.35 and over 0.9 when maturity begins, with greenness diminishing. The peak values can be generally observed in May (before flowering) and less in June, in the grain filling stage. Panek and Gozdowski (2020) observed similar values of NDVI for wheat monitoring in Central Europe in 2015 and 2016, especially during the maturity phase. There was quite high heterogeneity between field values for every year, although 2018 had quite a similar development of values over time. The NDVI's means for the wheat fields were 0.74, 0.69, 0.76, and 0.77 between the years 2015 and 2018. The Standard deviations for wheat were 0.14, 0.19, 0.21, and 0.15 between the years 2015 and 2018.

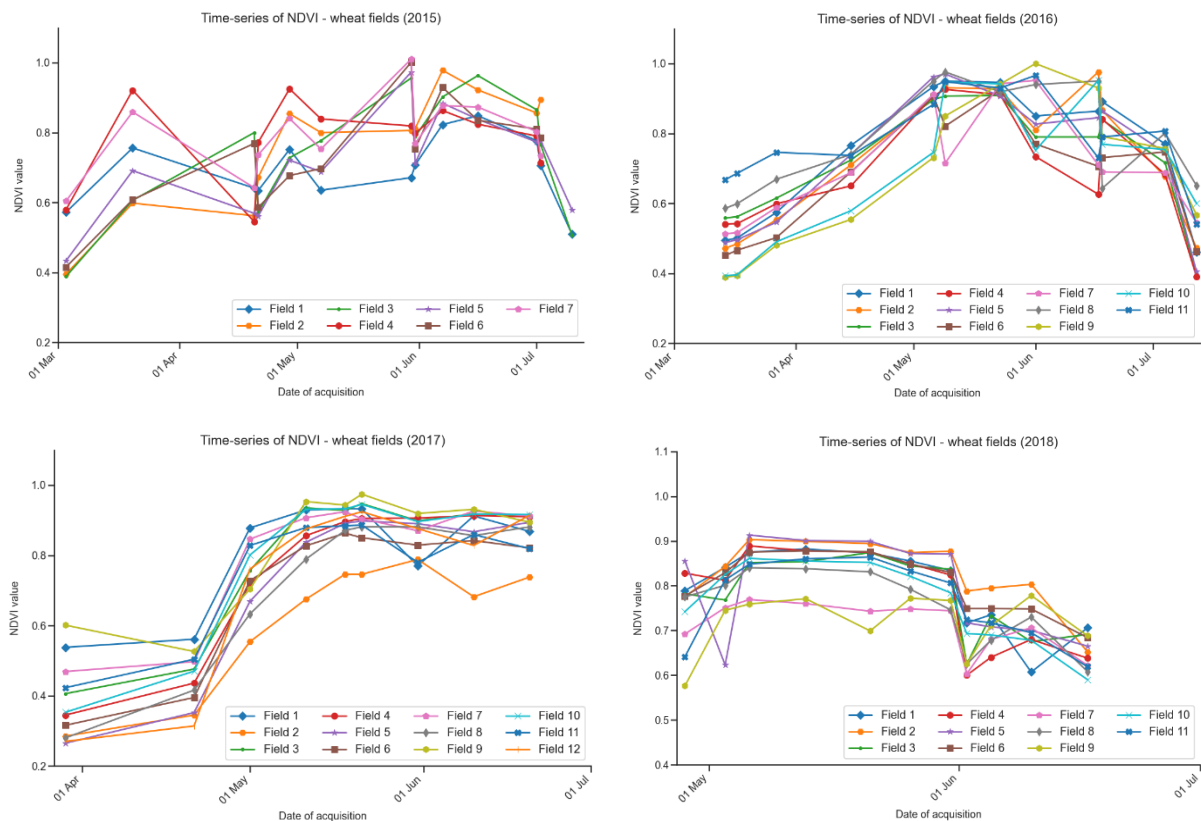


Figure 20. Normalized difference vegetation indices for investigated wheat fields throughout the 2015 – 2018 growing seasons. (Source: Tůma et al. 2021)

6.1.2 RVI results

Figure 22 presents all the results for the Radar Vegetation Index for wheat fields in the monitored seasons from 2015 to 2019. These results stand for adjusted Tůma et al. (2021), since the observation period needed to be extended for goals crop growth modelling. The year 2015 is presented here due to the later presentation of the correlation between NDVI and RVI.

As can be noticed, the RVI data were not influenced by cloud cover, so repeat measurements were mostly periodical. The timeseries of RVI seems to be remarkably close to the NDVI series and the BBCH scale (Domínguez et al., 2015); however, there were several differences. Firstly, the RVI results had significant periodicity in the rapid decrease and increased in values (noise) during the development of the growth curve. This phenomenon will be more thoroughly described further in the text. Secondly, whilst the NDVI values reached maximum values of 1, the RVI values reached results almost 1.4. Finally, RVI development through time was more gradual as there were more

available measurements. It also seems that the spatial distribution of RVI was very heterogeneous, as can be seen in **Figure 21**. This high irregularity is caused by speckle effects (graininess), as described in Goodman (1976). It seems that applying Lee Sigma provided insufficient outcomes. However, promising speckle filtration was presented by Robertson et al. (2020), primarily using the Touzi filter. **Figure 21 - b)** also reveals that Field 7 (see **Figure 14** to see Field locations) in the year 2017 changed its area, probably due to legislative regulations. The significantly different results can be seen in the southeast part of the field.

Initial RVI values were between 0.08 and 0.7, and peak values were over 1.5. The final RVI values ranged between 0.77 and 1.31 when crop maturity began. RVI values generally achieved their peak around the end of June and the beginning of July (development of fruit). It was also observed that wheat recorded high values in May when the grain filling stage took place. Mean RVI values were 0.73, 0.71, 0.65, 0.59 and 0.65 between the years 2015 and 2019. The standard deviation between years 2015 and 2019 was 0.26, 0.27, 0.26, 0.25 and 0.22. The results for wheat generally seemed to show a similar development as described by Kim et al. (2014) for L-band monitoring; however, the values reach higher numbers. A modified approach to how to use RVI for monitoring rapeseed and wheat by Sentinel-1 was recently presented by Mandal et al. (2020 - a; 2020 - c). The tables with descriptive statistics for all filtered and unfiltered RVI products can be found in **Annex Table II - IX**.

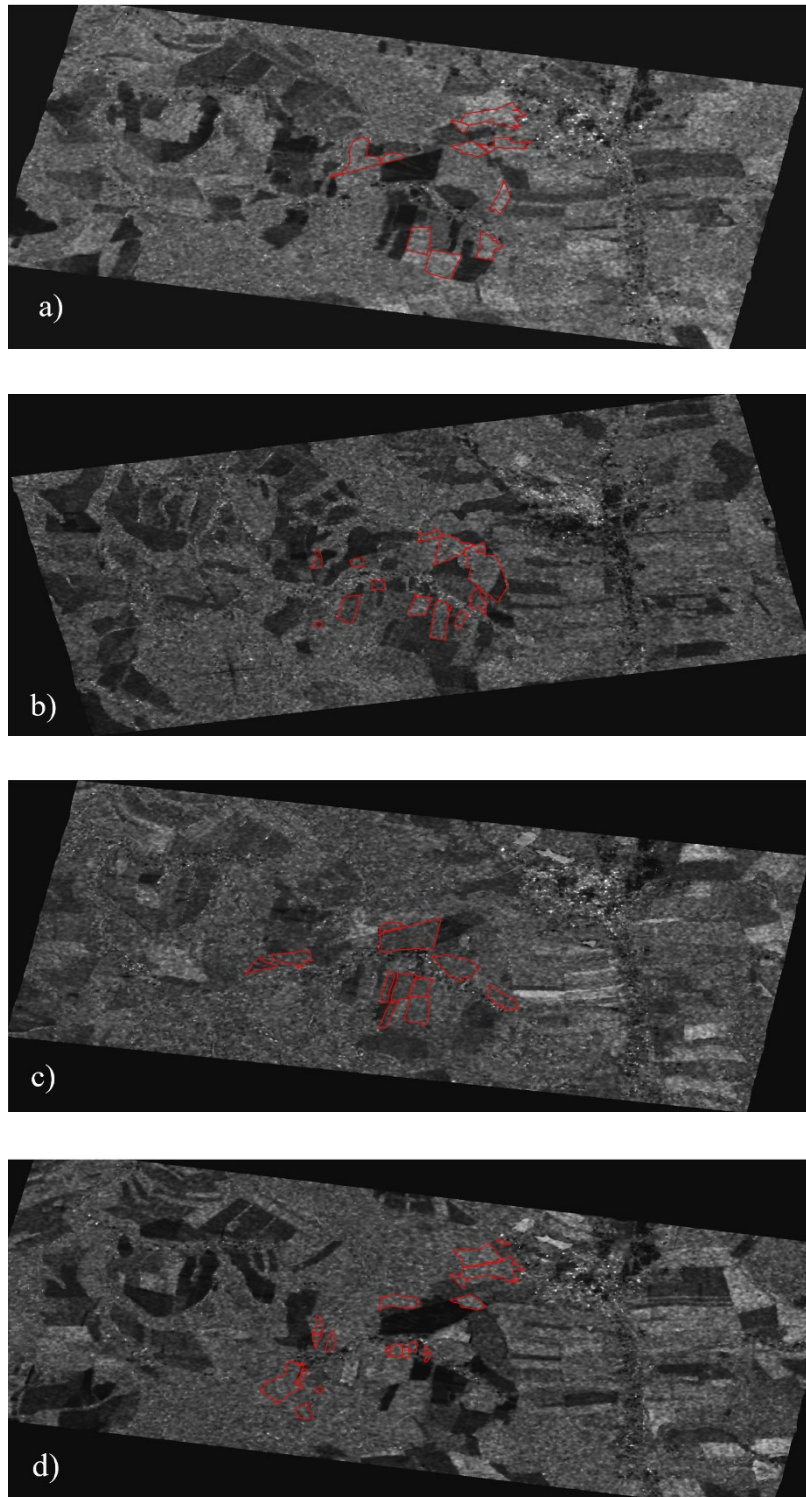


Figure 21. Radar Vegetation Index visualization of monitored wheat (red) fields and its graininess – a) 5.5.2016; b) 3.5.2017; c) 2.5.2018; d) 2.5.2019; Different relative orbits; white – high values, black – low values.

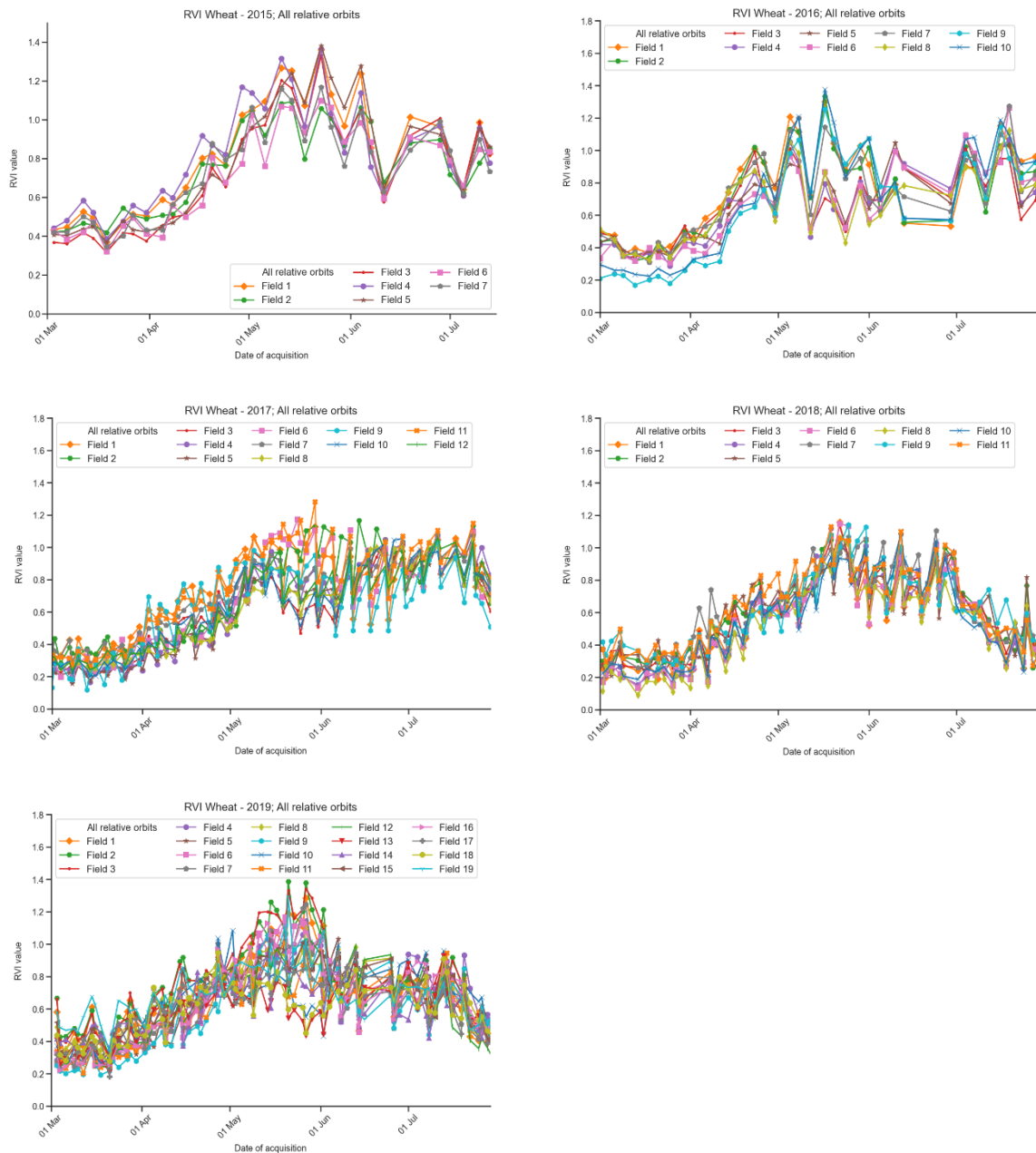


Figure 22. The average Radar Vegetation Indices for monitored rapeseed and wheat fields throughout the 2015 – 2019 vegetation seasons (**Source:** adjusted from Tůma et al. 2021)

The above-mentioned issues of rapid increase and decrease in RVI, so-called noise, were solved by data wrangling and considering metadata from satellite imagery during the analysis. The data wrangling output is illustrated in **Figure 23**. As can be seen, the rapid decrease and increase in RVI timeseries can be solved via the selection of Relative orbits

and Platform, which will be used. Although **Figure 23** shows only the results from Field 1 and Relative orbit 22, the application of this procedure to other Relative orbits and fields provided a similar smoothing of the curve. Such a phenomenon has not yet been described in the case of RVI, however Schaufler et al. (2018) recently thoroughly analyzed the azimuthal anisotropy of Sentinel-1 from the perspective of azimuth angle, and Gauthier et al. (1998) described its sensitivity in agricultural areas from the perspective of Incidence Angle. Li et al. (2016) recently suggested promising models for the extraction of polarimetric information based on the different anisotropy of polarimetric scattering. Considering these articles in the future development and interpretation of RVI timeseries could bring more positive outcomes (Tuma et al. 2021).

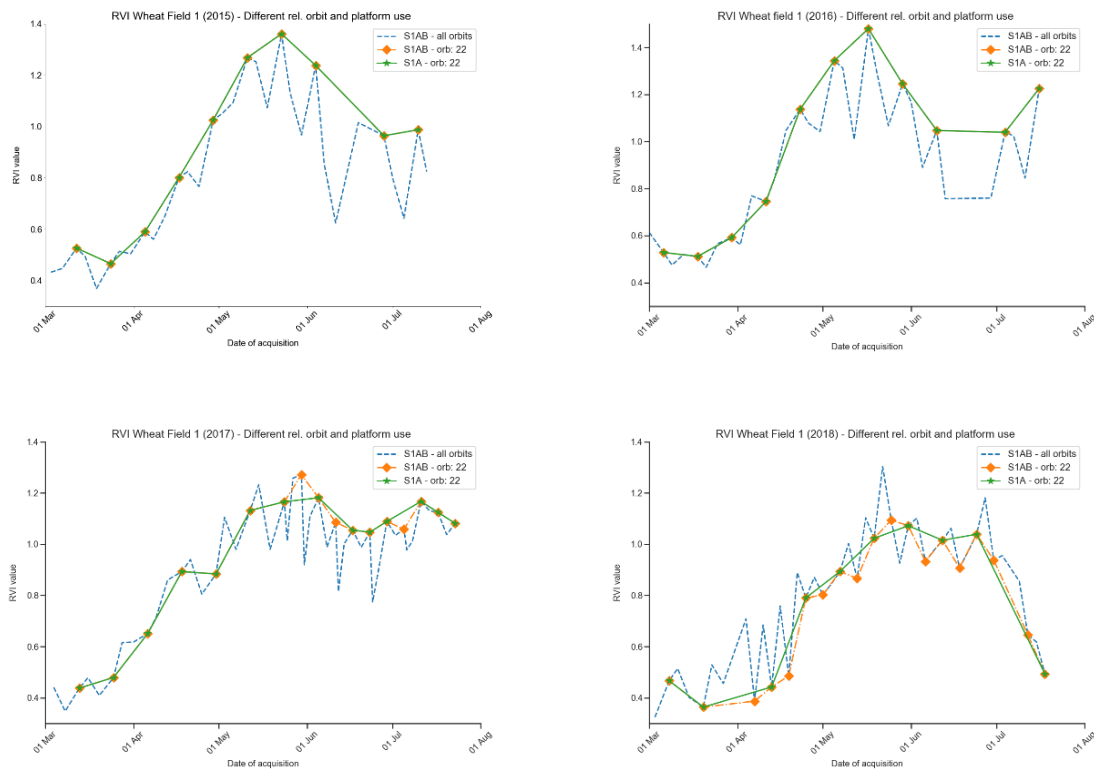


Figure 23. Illustrative timeseries of wheat RVI for field 1 through the vegetation seasons of 2015 – 2018. The dash line represents images from all Relative orbits (22; 73; 124), while the dotted-dash line shows only results from Relative orbit 22. The full line considers only Relative orbit 22 for the Sentinel-1 platform A. (**Source:** Tuma et al. 2021)

6.1.3 Correlation of Radar Vegetation Index with Normalized Difference Vegetation Index

The following results were published in *Tũma et al. (2021)* and consider RVI for years 2015 -2018 and shorter vegetation seasons (i.e., from the beginning of July until half of July). Simple linear regression was performed between NDVI and RVI, as can be seen in **Figure 24** and **Table 12**. The Line of Best Fit and R-squared were used for the given data set of wheat and for every single Relative orbit and Platform. As can be seen, the goodness of fit slightly increased for Relative orbits 22 and 73. On the other hand, decrease in the case of Relative orbit 124. The best regression outcome for the model was 0.387, monitored from Relative orbit 73. These changes in correlation can be explained by different geographical location or different Relative orbit that can alter the behavior of the model due to differences in incidence angles (Gauthier et al., 1998; Shuai et al., 2019). A similar comparison of NDVI and RVI (obtained from Radarsat-2) was presented by Gonenc et al. (2019) with a correlation result of 0.505; however, without consideration of the Relative orbital effect (Tũma et al. 2021).

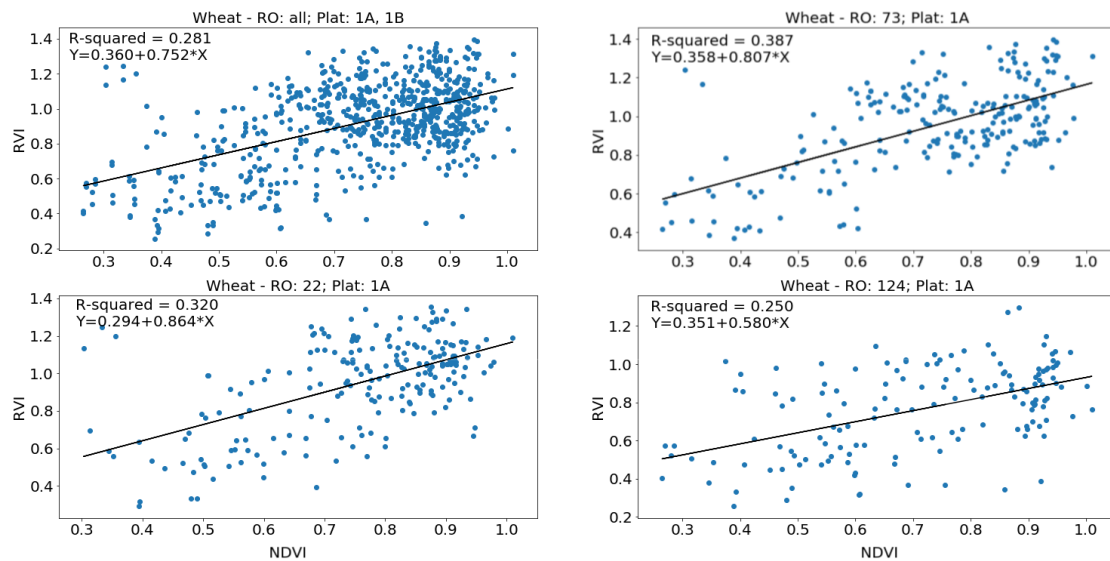


Figure 24. Scatterplots of RVI and NDVI for wheat with simple Linear regression and R-squared. Comparison of all data used, single platform and Relative orbit used.

(Source: Tũma et al. 2021)

Table 12. Linear regression results for NDVI and RVI values of observed wheat fields. Different Relative orbit utilization; Platform A.

Platform/Relative orbit	R-squared	Intercept	Coeff. (NDVI)
1A; All	0.281	0.36	0.752
1A; 22	0.32	0.295	0.864
1A; 73	0.387	0.358	0.807
1A; 124	0.25	0.351	0.58

6.2 Radar Vegetation Index filtering and adjustment

Based on previous findings of RVI dependence on the platform or Relative orbit, from which the imagery is acquired, the decision to use the S–G filter was made. The overall results for all wheat fields and all seasons can be seen in **Figure 25**. As can be seen, the development of RVI was smoother as noise caused by different used Relative orbit or platform was reduced. The successful settings for window length and polyorder were 33 and 8. The measurement of filtering accuracy will be described further in the text.

Although there are differences, the filtered RVI was more resembling the vegetation phenology curve (see **Annex Figure I, II**) than the unfiltered results. While the peak of phenological development (e.g., NDVI) in the northern hemisphere occurs in June/July turn, the RVI was experiencing two peaks – one in May and one in June/July turn (Chang et al. 2013, Griffith et al. 2002). Although the overall phenological development can have uncomplicated development as described earlier, the wheat phenological development can experience the sudden drop (see **Annex Figure III**) of NDVI values during the 50 – 69 BBCH (start of heading – end of flowering) as described in Domínguez et al. (2015). A similar decrease experienced Li et al. (2021) when they observed the winter wheat in Fucheng County (37°46'–38°02' N, 116°04'–116°33' E).

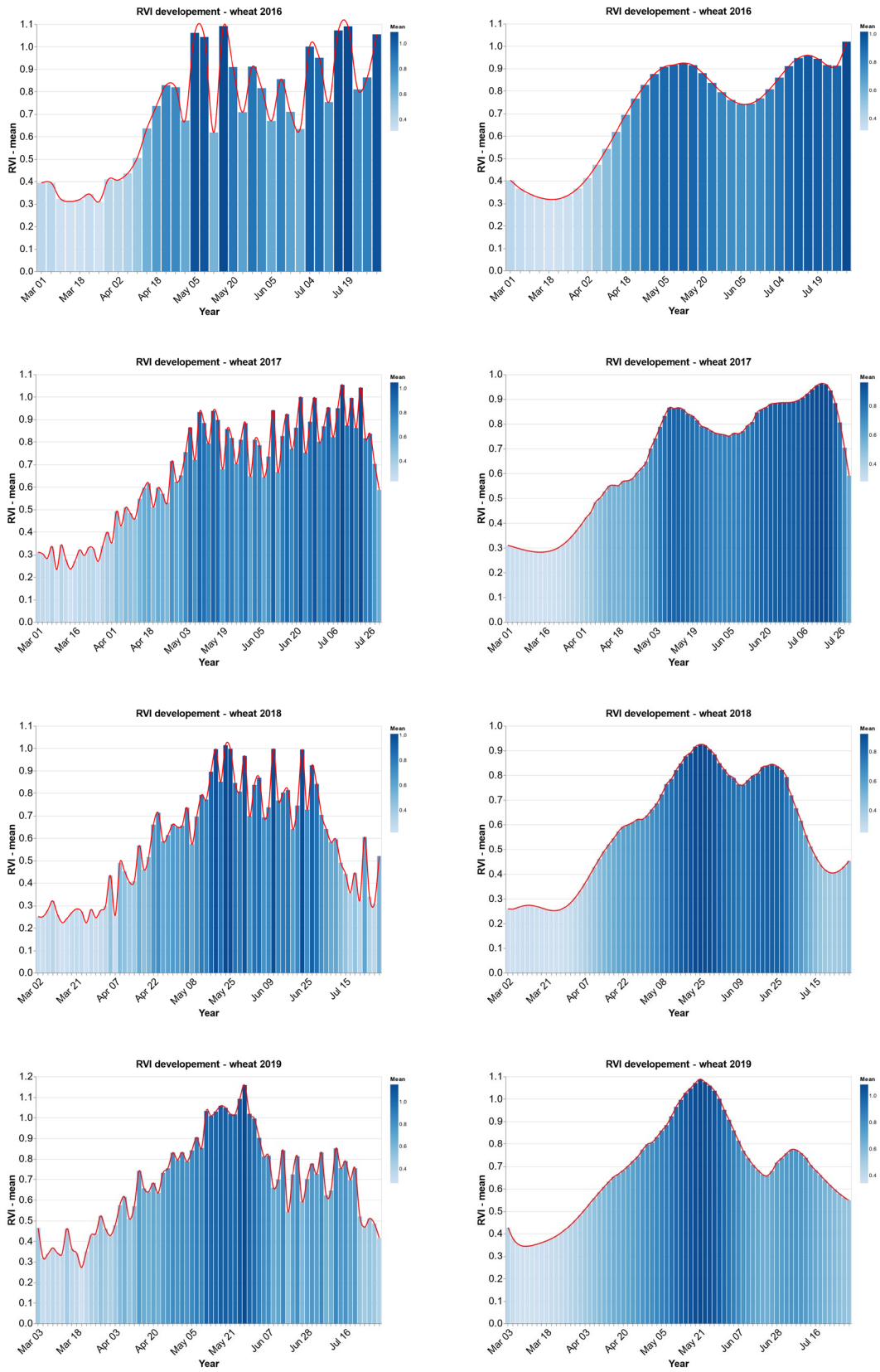


Figure 25. Average RVI unfiltered (left) and filtered (right) values (2016 -2019) – development through vegetation season; basic interpolation (red line).

The Vreugdenhil et al. (2018) found that winter cereals' (barley and wheat) phenological stages and vegetation structure has an impact on Cross-Ratio (VH/VV backscatter). Moreover, from the engagement of Random Forest machine learning, it is obvious that VH/VV backscatter was a very important variable in the prediction of VWC. Harfenmeister et al. (2019) discussed the backscatter variation due to plants development and soil moisture. However, Harfenmeister et al. (2019) also explain that the decrease of backscatter signal is caused by the increasing development of vegetation, causing the higher attenuation of the backscatter. When vegetation development comes to heading, then the backscatter starts to be more driven by vegetation and less by soil moisture. To some degree, Holtgrave et al. (2020) completed these findings with statements that SAR indices cannot be used interchangeably with the optical indices. The findings of Harfenmeister et al. (2019) could explain the behavior of the backscatter, however probably not the RVI. The difference was that during the BBCH 20–29, the results RVI was increasing, while during the same period, Harfenmeister's measurement was decreasing. To some extent, results from period BBCH 30 – 59 also didn't match Harfenmeister's results. These struggles suggest that more research needs to be done to understand the relationships between RVI, Backscatter, Optical indices, and field measurements (soil moisture, vegetation canopy development).

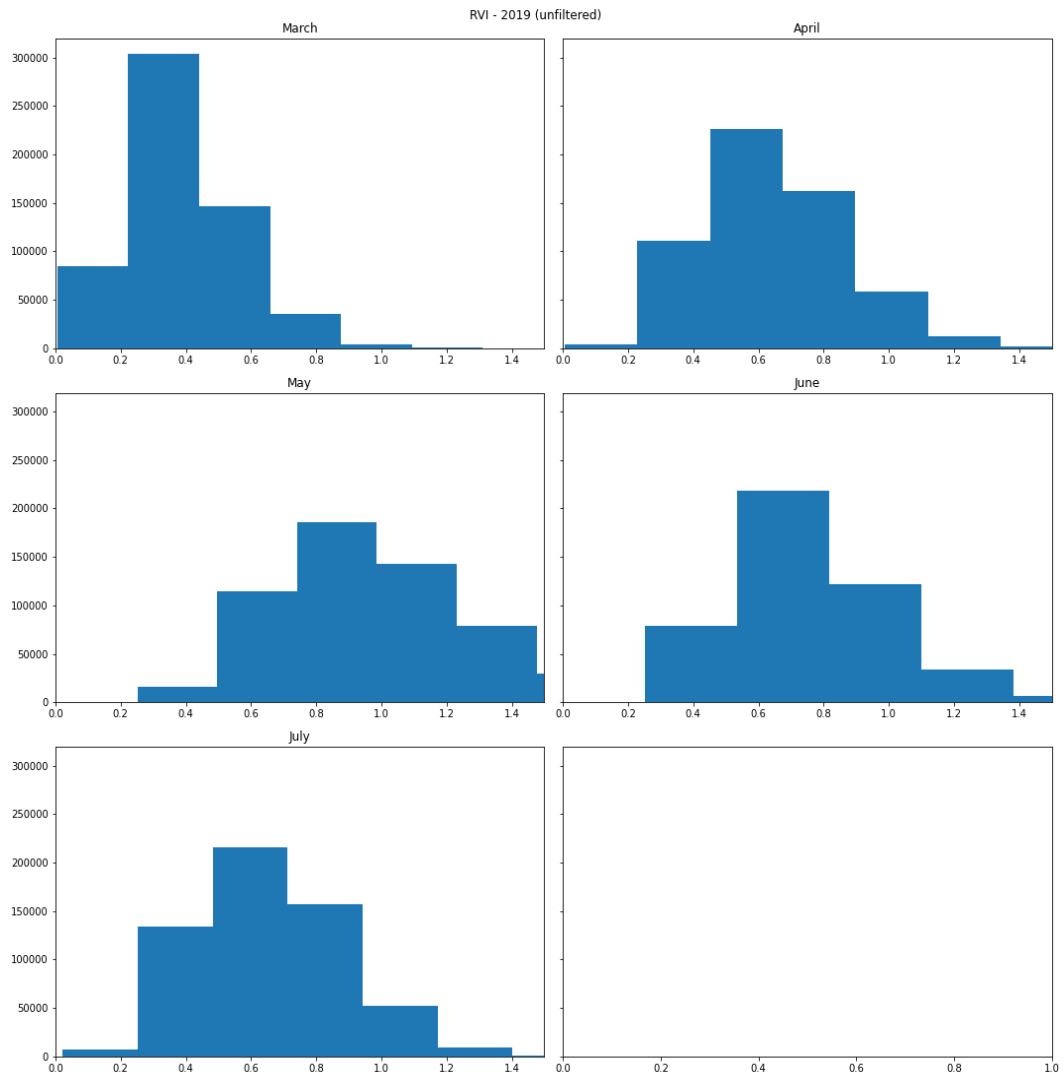


Figure 26. Histogram for RVI values – year 2019; unfiltered values.

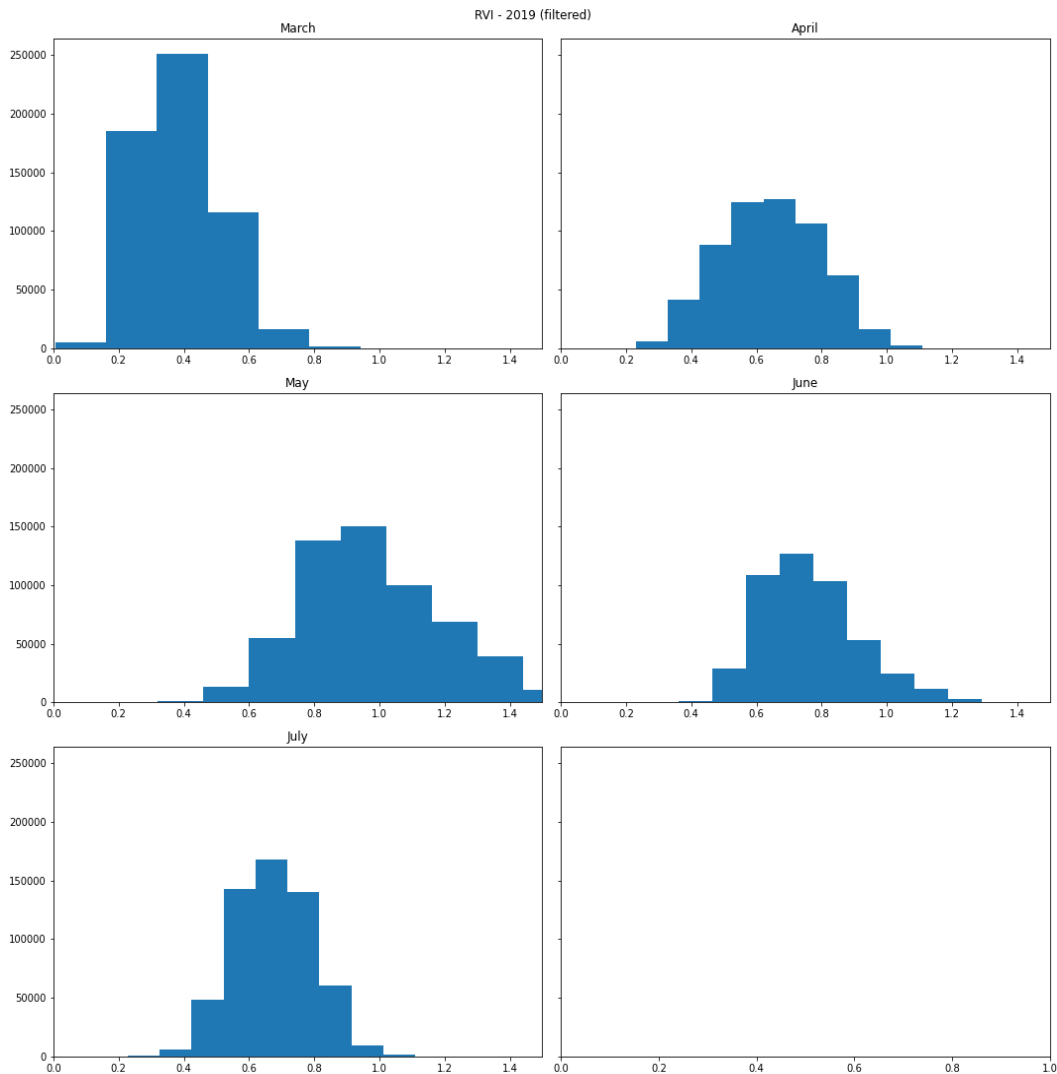


Figure 27. Histogram for RVI values – year 2019; unfiltered values.

The differences between the monthly RVI data structures can be seen in **Figures 26 and 27**, depicting monthly histograms for the year 2019. All other years recorded similar development. As can be noticed, both figures demonstrate the gradual development of the most recorded values. It also seems that filtered results were more bell-shaped, indicating the normal distribution. For example, the result for the unfiltered April seemed to be skewed to the left, while filtered results for April provided more symmetrical data distribution. Resembling practice can be observed in June and July. The example of visual difference between unfiltered and filtered Sentinel-1 satellite images can be seen in **Figure 28**, which depicted images for five dates – 3.3.2019, 2.4.2019, 2.5.2019, 1.6.2019, and 1.7.2019 for Fields 1, 2, and 3. The difference between the spatial distribution of values between filtered and unfiltered datasets was obvious mostly in the later season,

while the beginning of the season (i.e., March and April) gathered similar results. The mean RVI values for filtered data were 0.71, 0.66, 0.59, and 0.69 between the years 2016 and 2019. The standard deviation was then – 0.2 0.13, 0.09, and 0.13. The tables with descriptive statistics for all filtered and unfiltered RVI products can be found in **Annex Table II**.

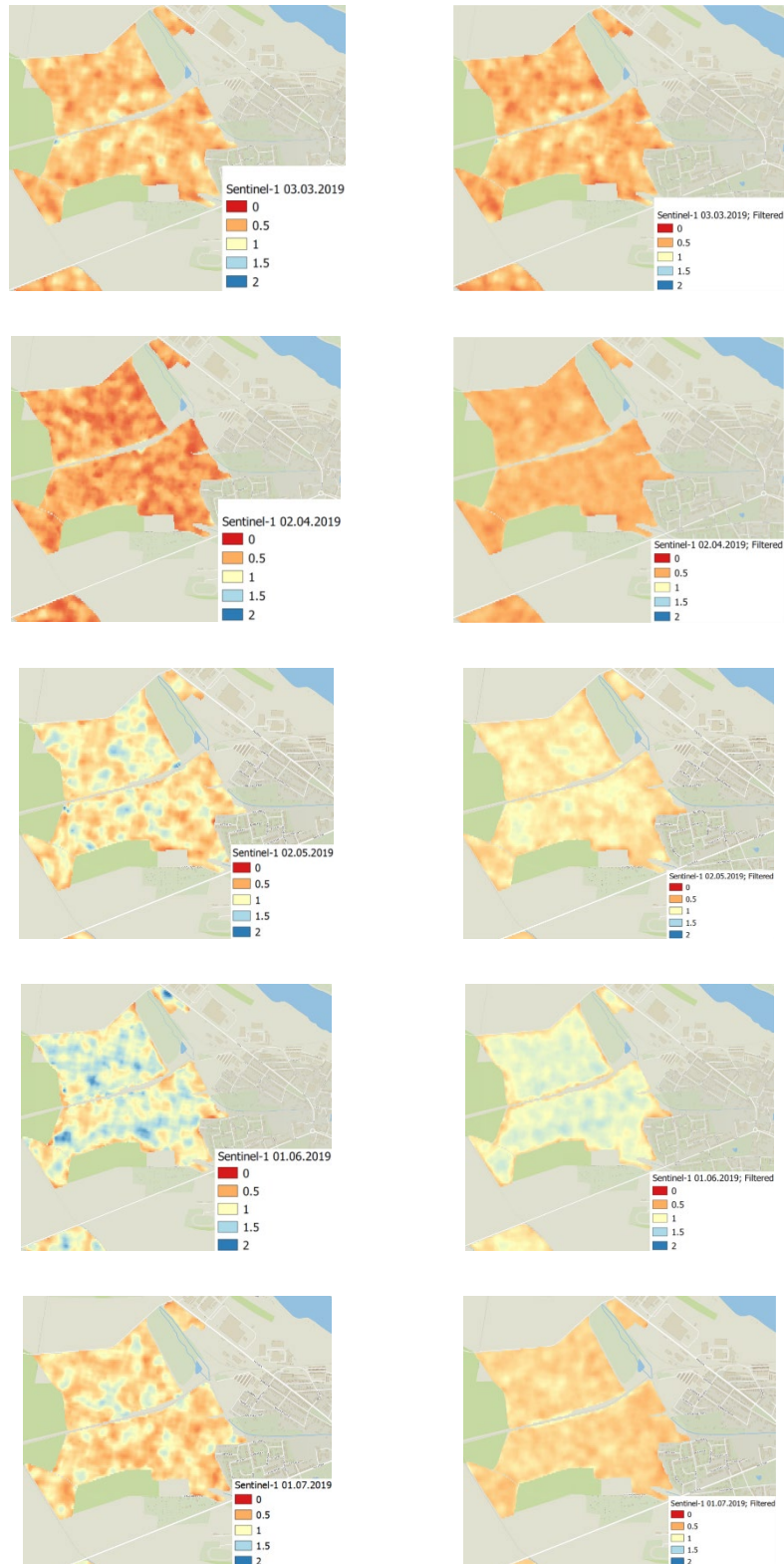


Figure 28. Comparison of five RVI images from season 2019 (3.3.2019, 2.4.2019, 2.5.2019, 1.6.2019 and 1.7.2019) before the filtering (left) and after the Savitzky–Golay filtering (right); Wheat fields 1, 2, 3.

It seems that filtration by S–G filter was not done yet in the case of RVI product; however, Soudani et al. (2021) used this method in *Potential of C-band Synthetic Aperture Radar Sentinel-1 time-series for the monitoring of phenological cycles in a deciduous forest*. During this research, the Sentinel-1 timeseries of VV/VH were filtered by S–G filter for characterization of the seasonal phenological cycles allowing to use of these data as phenological metrics.

6.3 Leaf Area Index estimation from Sentinel-2

This chapter presents the results of LAI estimation from Sentinel-2 satellite imagery by the Biophysical processor from the SNAP software. The results were collected from the year 2016 to 2019. **Figure 29** visualized the results of the monitored wheat fields for every yield. The monitoring used accessible Sentinel-2 satellite imagery without clouds. There were 568 659 results if we considered the number of pixels. The number of results for 2016 was 96 392, for 2017 it was 171 613, for 2018 it was 62 665, and for 2019 it was 237 990. Unfortunately, the LAI results were not in such extension how it had been intended. It is because of technical difficulties, which arose during the data processing. Some data from satellite imagery were corrupted during the processing due to wrong data wrangling of Biophysical processor within the data processing of satellite images with non-standard shape (e.g., triangular). Still, the number of results was enough to provide reasonable outcomes and inputs for the prediction of R-LAI and data assimilations into the crop model.

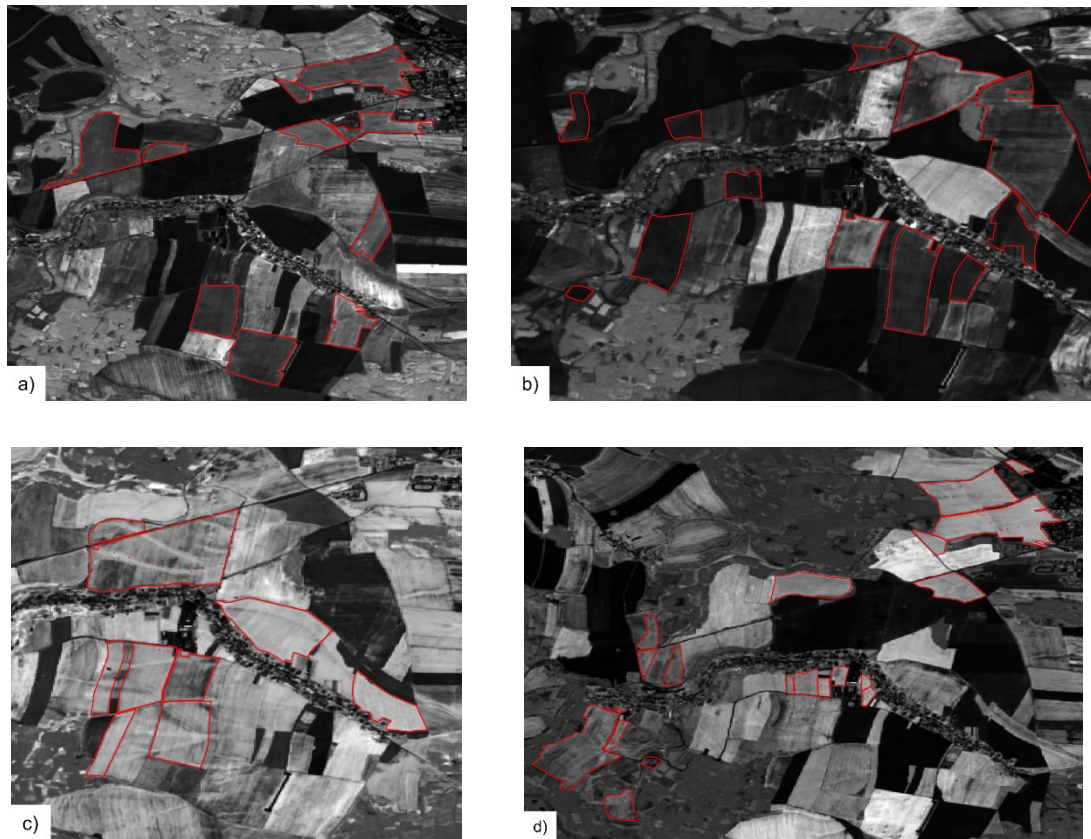


Figure 29. Visualization of LAI products (2016 -2019); wheat fields – red delineation;
a) 27.3.2016, b) 1.4.2017, c) 31.5.2018, d) 1.5.2019.

Figure 30 depicts the mean LAI values for available results. As can be seen, the general curve pattern was, to some point, like NDVI and filtered RVI. The peak values could be observed in May. However, the LAI for wheat differed from RVI in the final part of phenological development. While RVI was fluctuating in July and June, the LAI values are dropping down. Nevertheless, the number of daily observations were much smaller with Sentinel-2 than with Sentinel-1, and some substantial development didn't have to be measured. The mean annual values for LAI products were 2.31, 3.71, 4.1 and 3.26 in 2016 – 2019, and the standard deviation was 0.40, 1.00, 0.81, and 0.88. The maximum LAI was recorded on May 18th, 2017, with the value of 7.14. The minimum value was recorded on May 18th 2017, and on May 13th 2018 with values of 0. The basic descriptive statistics for every LAI product from obtained satellite imagery can be found in **Annex Table I**.

Overall dynamics of LAI for three C3 crops (spring barley, winter wheat and oilseed rape) was presented by Tripathi AM et al. (2017). Although the measurement was conducted only for one research location, their LAI results for wheat are in line with this research

showing maximum LAI was around 4.1 for wheat. Similar development of winter wheat's LAI in the Czech Republic was described by Pozníková (2016), which used plant canopy analyzer system - SunScan by Delta-T Devices and regularly sampled five spots on research experimental field. Nevertheless, comparing the Pozníková's results with the **Figure 31** reveals that field measurement by SunScan was providing much higher results in this research. This could be caused by the favourable year 2015 or by the errors during the measurements. Another measurement of LAI in the Czech Republic was presented by Wimmerová et al. (2016) and Tripathi et al. (2018). They also measured the LAI by SunScan and found the values, which were broadly in the line with results of this work.

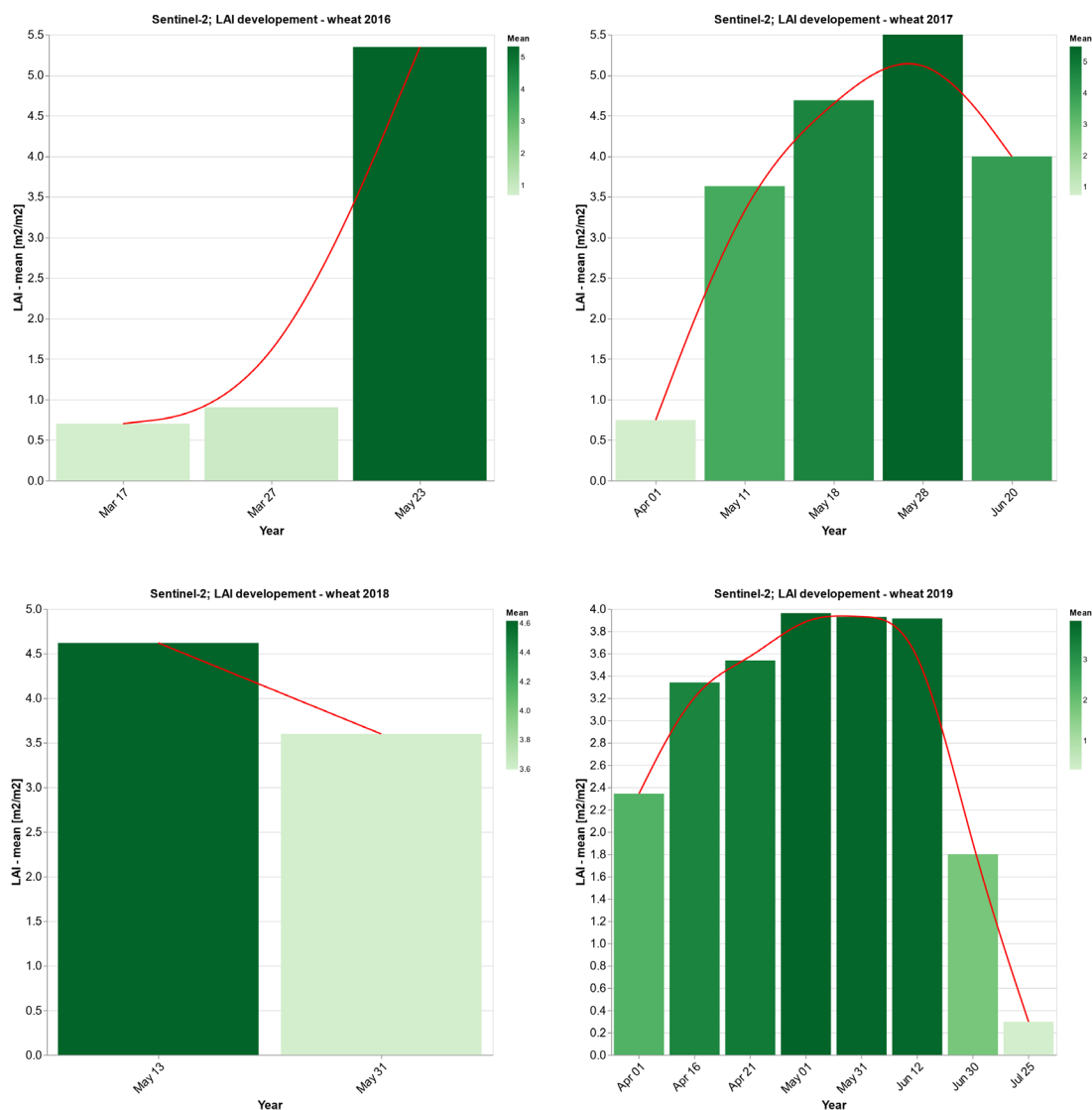


Figure 30. LAI development through vegetation season (2016 – 2019); Wheat fields – mean; basic interpolation (red line).

No research for LAI estimates from satellite imagery was found for conditions of the Czech Republic. However, several researchers investigated the possibilities to retrieve LAI values for wheat by satellite imagery. In 2017, Bochenek et al. (2017) analyzed the LAI ground measurement with vegetation indices, and LAI estimated from Sentinel-2 in SNAP software by the Biophysical processor for wheat fields in the Wielkopolska region. The results revealed similar values; however, the authors concluded that these values are overestimated for most fields. The high error of LAI estimation by SNAP software was also found by Pasqualotto et al. (2019), which tried a different approach of LAI estimation for durum wheat (and other crops) and compared it with the ground measurements and SNAP estimations. Authors estimated $R^2 = 0.475$ and $RMSE = 0.91$ between the in-situ measurement and SNAP estimation.

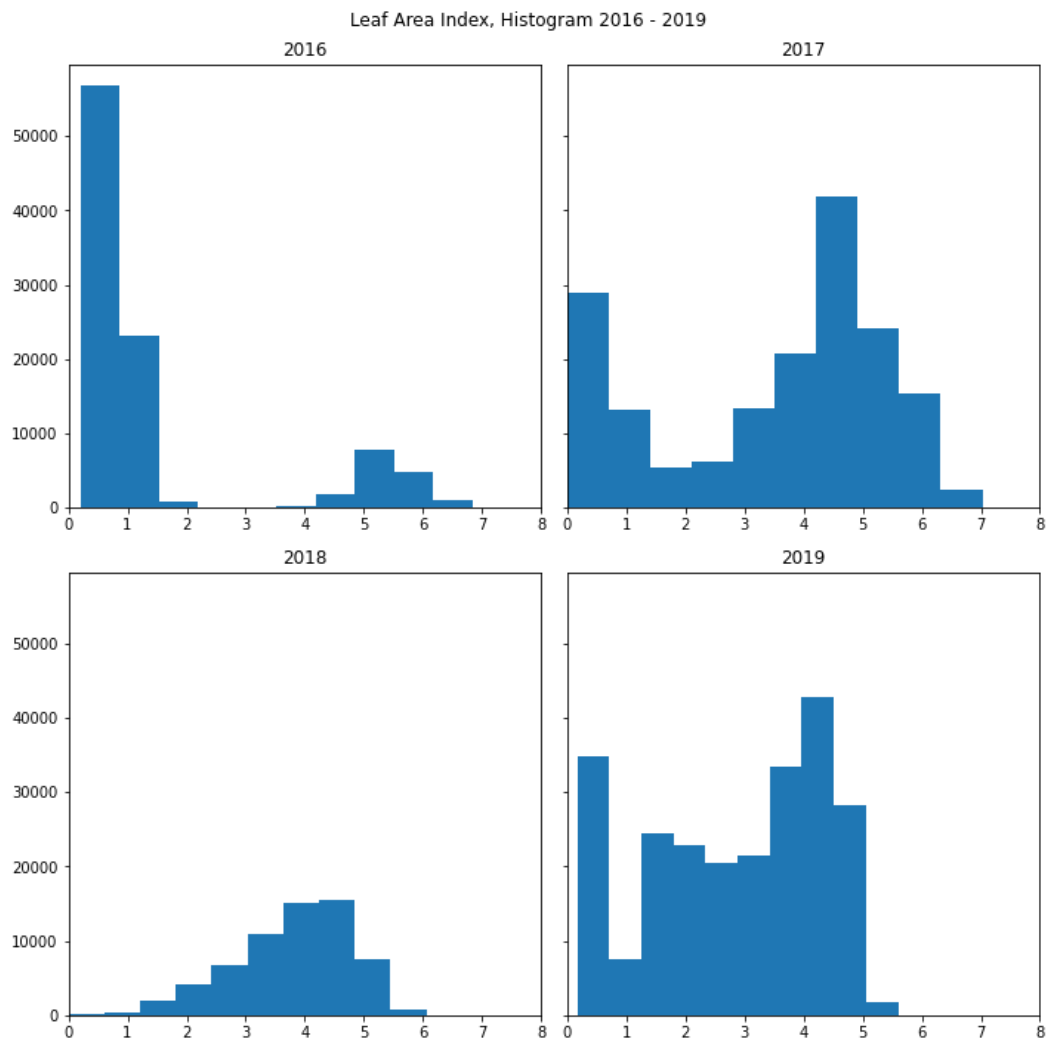


Figure 31. Histogram – wheat’s LAI [m².m⁻²]; vegetation seasons (2016 – 2019).

6.4 Leaf Area Index prediction from Sentinel-1 by Machine Learning

6.4.1 Data composition

The LAI prediction started with general data wrangling and matching the values of LAI with values of RVI. **Table 13** presented the results of finding the closest observations dates between the RVI and LAI products. Because the number of LAI products was smaller, they were so-called masters during the matching, while RVI were so-called slaves. For every LAI product were found reasonable RVI observation. As can be seen, the longest period between LAI product and RVI observation was 4 days immediately during the first match. There was only one match with a latency of 3 days, while the rest of the matches had a latency of 0, 1, or 2 days. Since the daily development for wheat was relatively small (Maruyama et al. 2010), the potential correlation shouldn't be harmed.

Table 13. Match tables for finding the closest Sentinel-1 and Sentinel-2 dates of observations.

LAI	RVI
2016-03-17	2016-03-13
2016-03-27	2016-03-25
2016-05-23	2016-05-20
2017-03-29	2017-03-28
2017-04-01	2017-04-01
2017-05-11	2017-05-09
2017-05-18	2017-05-18
2017-05-28	2017-05-27
2017-06-20	2017-06-20
2018-05-13	2018-05-13
2018-05-31	2018-05-31
2019-04-01	2019-03-30
2019-04-16	2019-04-15
2019-04-21	2019-04-21
2019-05-01	2019-04-29
2019-05-31	2019-05-29
2019-06-12	2019-06-10
2019-06-30	2019-06-28
2019-07-25	2019-07-25

Additionally, the research continued with matching values from RVI and LAI products (pixel matching) with sample size $n = 568\ 659$. The Pearson correlation coefficient was calculated for LAI and RVI, resulting in a value of 0.69, which suggests a high degree of correlation between variables. The Pearson correlation coefficient was also calculated for every year. 2016 gathered almost perfect correlation, then 2017 correlation was comparable to overall correlation with value 0.67. The correlation for the year 2018 was -0.11, while for 2019 it was 0.49 (moderate correlation). In addition, it was assessed the relation between RVI and LAI. **Figure 32** demonstrates the data clouds (scatterplots) of RVI and LAI values. From these results, it was clear that data that covers the longer period of vegetation season provide better correlation results. Such evidence can be seen in the year 2017 and 2019. While the year 2017 recorded the data for April, May, and June, 2019 gathered data for April, May, June, and July.

Jiao et al. (2009) measured the sensitivity of RADARSAT-2 with ground truth data of LAI (Corn and Soybean) in June, July, and August. They found that HV Backscatter correlated with ground truth data well. The R-square reached value of 0.92 for the corn measurements. The research aimed at the relationship between the backscattering coefficient (AIRSAR sensor - fully polarimetric at L- and C-bands) and the biomass (LAI) of narrow and broadleaf crops found out that backscattering generally increases for broad leaves (sunflower), however, decrease for narrow leaves (wheat) as LAI increase (Macelloni et al. 2001). The sensitivity of wheat LAI to backscatter was also tested by Fontanelli et al. (2013) with X-band SAR (COSMO-SkyMed and TerraSAR-X). They stated that even though the x-band is not the best frequency for monitoring the soil and vegetation parameters, a high sensitivity was found between the of the backscatter was found out. They confirmed that the decreasing trend of backscatter is related to the vegetation growth of narrow-leaf crops (wheat and barley). They also presented that the determination coefficients were 0.6 – 0.7 between the LAI and Backscatter. Earlier discussed, Vreugdenhil et al. (2018) found that R^2 between the backscatter indices and LAI is best in the case of linear model and cross-ratio (CR). From the perspective of RVI, it seems not many studies were conducted. Nevertheless, Szigarski et al. (2018) analysed the RVI for SMAP L-band radar data on global levels and compared results to the Moderate Resolution Imaging Spectroradiometer's (MODIS) VWC and LAI. They found

out that the correlation between the LAI and RVI is $R^2 = 0.56$, which suggests a weak, however positive, correlation.

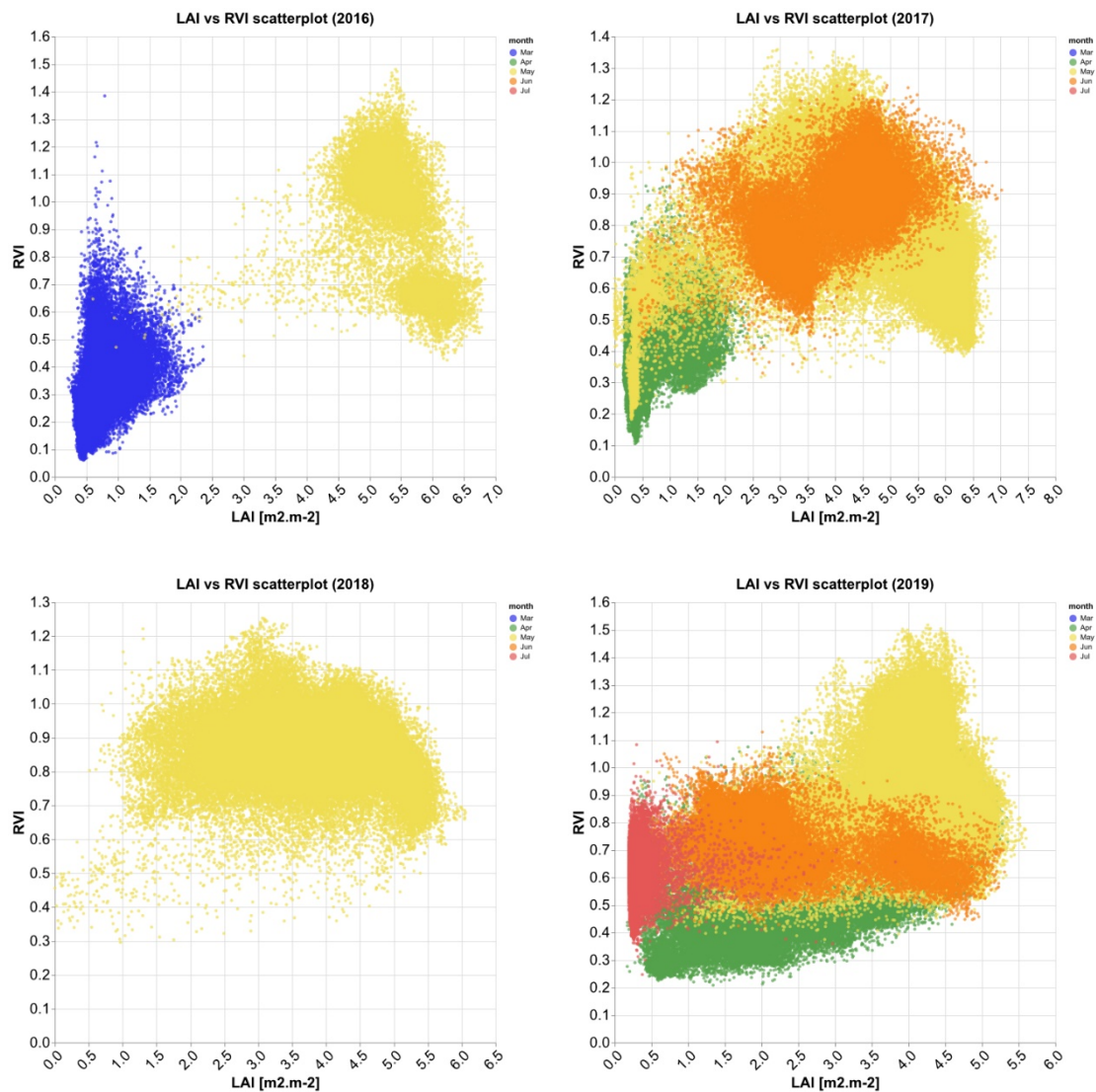


Figure 32. Scatterplots of annual RVI and LAI values for wheat (2016 – 2019); blue – March, green – April, yellow – May, orange – June, red – July.

6.4.2 Random Forest Regression – results

The training of the RFR started with testing the right settings of hyperparameters. The function of Scikit-learn library the Random Search was tested. The best result for random 100 combinations was the following:

- **Number of estimators - 500**
- **Maximum depth - 5**

- **Minimum samples split** - 10
- **Minimum samples leaf** - 1
- **Max features** - 5
- **Bootstrap** – True

After the Random Search determined the composition of parameters, the Grid Search was also tested with use of exhaustive search over the selected options of hyperparameters. The final hyperparameters settings were as follows:

- **Number of estimators** - 500
- **Maximum depth** - 7
- **Minimum samples split** - 10
- **Minimum samples leaf** - 1
- **Max features** – sqrt
- **Bootstrap** – True

So, as can be seen, the Grid Search changed the Maximum depth to 7, and Max features were changed to sqrt, which means Square root of n features. The Random Forest was then run for filtered data and unfiltered data. Test features (RVI) and test predictors (LAI) were set apart with test size = 0.3. As it was already described, The Pearson pairwise correlation coefficient for filtered data was 0.69, while for the unfiltered dataset, it was 0.64. The accuracy of RFR model was 0.52 for filtered RVI data and 0.51 for unfiltered data. The Decision tree for RFR can be found in **Annex Figure V**. According to the fitted model (with filtered RVI data), the prediction of R-LAI for $n = 10\ 337\ 601$ was done. The results of predicted R-LAI can be seen in **Figure 33** for every single year/vegetation season and for every single wheat field. The mean values for R-LAI were 2.96, 2.78, 2.41 and 2.87 $\text{m}^2.\text{m}^{-2}$ between 2016 – 2019. The standard deviation was then 1.34, 1.40, 1.36, and 1.19 $\text{m}^2.\text{m}^{-2}$. It is important to highlight that the maximum values were 4.28 $\text{m}^2.\text{m}^{-2}$ and minimum values were 0.48 $\text{m}^2.\text{m}^{-2}$ in every single year. It is likely to be an outcome of RFR decision tree. When comparing the R-LAI results to those of LAI described earlier, it must be pointed out that general similarity was found. Also, the development of R-LAI is some degree similar to the RVI development. Nevertheless, if we compare the results of the proposed method with those of the traditional methods, we see that the standard development of wheat's LAI (see **Annex Figure IV**) is without fluctuation

(Yesilkoy et al. 2015; Kumari et al. 2009; Afrasiabian et al. 2021). The irregular shifting up and down in R-LAI suggests low correlation during certain parts of the main vegetation season (i.e., generally May). On the other hand, the outline and the structure of R-LAI curve suggested that S–G filtering could provide a better result (shape) of R-LAI in the future.

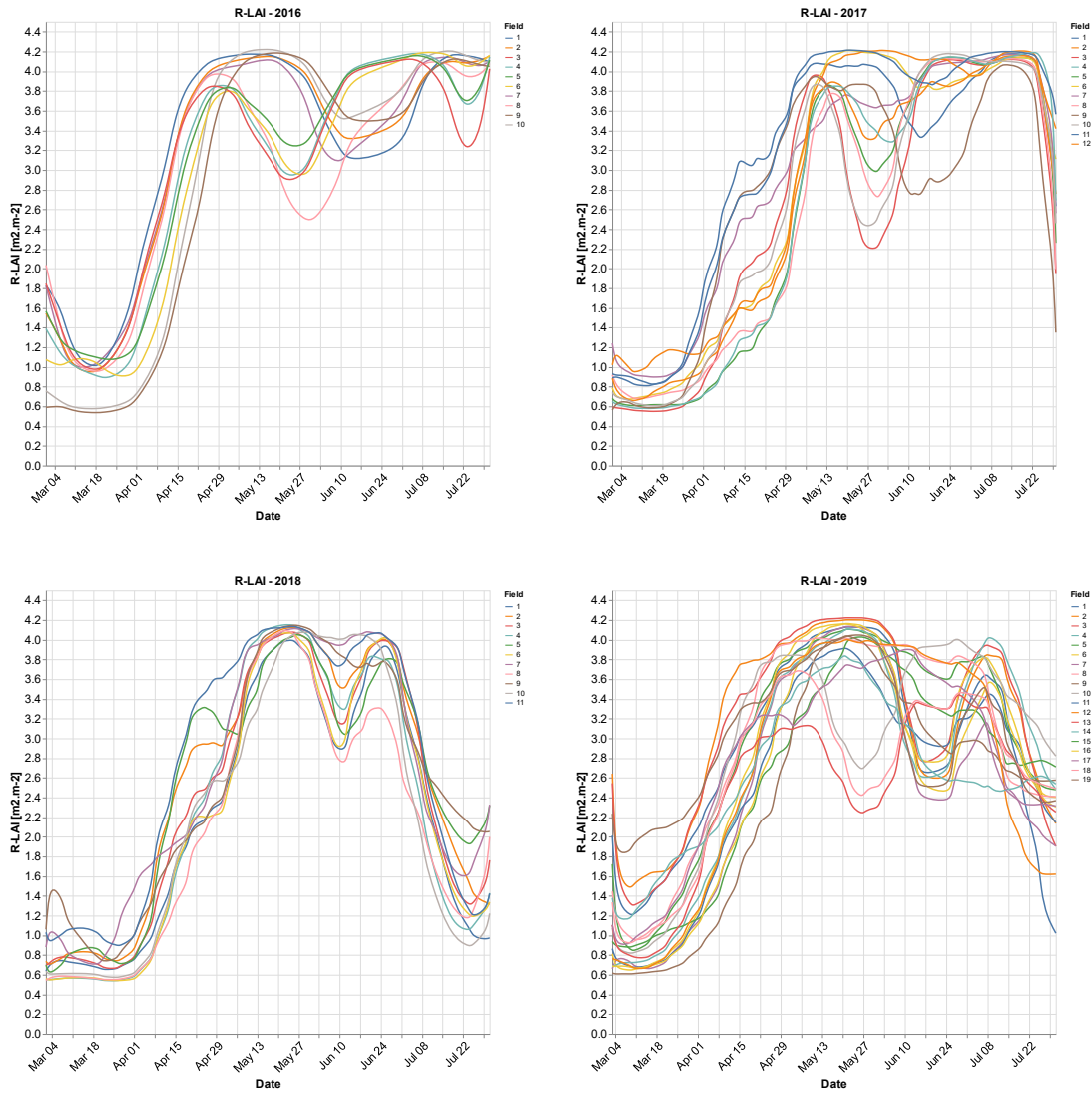


Figure 33. Line charts of R-LAI results for years 2016 – 2019 with single wheat field development.

6.5 Wheat – crop growth modelling

The crop modelling for simulation of wheat growth was done in the WOFOST for the period 2015 – 2019. The 52 simulations were performed. The final yield (TWSO) for crop growth modelling of wheat can be seen in **Figure 34**. The yield represents the

obtainable amount of harvest in tons per hectare after the crop reached maturity. The average yield was 11.23, 7.77, 11.25, and 11.70 t.ha⁻¹ in the period 2015/2016 – 2018/2019. The minimum yield was 6.82 for field ID 3 with the sowing date 11.10.2016. The maximum yield was obtained on 26.9.2015 with a value of 12.19. Some of the fields have the same results as the major factor influencing the growth was the sowing date. The tables with final yield values can be seen further in the text (**Table 14, 15, 16, 17; chapter 6.6.3**) for easier comparison of final results. While the RMSE was 4.23 t ha⁻¹, the MAE was 3.79 t ha⁻¹.

As can be noticed, the WOFOST simulation overestimated the TWSO values in most cases. For the year 2016, 2018, and 2019, the overestimation was recorded. The only year 2017 provided the majority of results, which were lower than the ground truth yield. These results tie well with previous studies wherein the overestimation is also experienced. The Pohanková (2016) tested the use of different models (WOFOST, DSSAT, HERMES, DAISY, and AQUACROP and ensemble of models) for the simulation of the spring barley and found that WOFOST is overestimating the final yield about 1.28 t.ha⁻¹ on average. The quite high overestimation of some yields was also experienced by Eitzinger et al. (2004) in the case of winter wheat and spring barley during the simulation of soil water content by the WOFOST. The overestimation of WOFOST was also noticed by Rötter et al. in the case of spring barley (2012) and by Palosuo et al. (2011) in the case of winter wheat.

One possible explanation of overestimation could be a quite low spatial resolution of NASA POWER meteorological data (i.e., 0.5 x 0.625 degree). The NASA POWER (MERRA2; see the 5.1.2.3) was tested by several researchers. White et al. (2008) provided the evaluation of NASA POWER data with data of 855 individual ground stations and found that RMSE is 4.1 °C for daily maximum temperatures and 3.7 °C for minimum temperature. The authors stated that the NASA POWER as a promising source of data for daily temperatures. Rodrigues & Braga (2021) and Aboelkhair et al. (2019) also evaluated the NASA POWER with a similar conclusion like the previous one. The MERRA2 also performed well in the evaluation of Reanalysis datasets in several studies (Zandler et al. 2020; Arshad et al. 2021). From this standpoint, NASA POWER can be considered as a good source of meteorological data. However, Pushpalatha et al. (2021) performed the sensitivity analysis of meteorological variables (minimum temperature,

maximum temperature, and solar radiation) for WOFOST and found that yield variation can be even up to 7.65 % with ± 5 %. By similar research, Mishra et al. (2015) proved that change in minimum or maximum temperature values can alter the yield by 24 % to 29 %. This would indicate that even with relatively small errors within the used meteorological data, the yield estimation errors can be quite high. On the other hand, more research needs to be done to provide a better understanding of reanalysis datasets' errors and their impacts on crop modelling (in WOFOST). So, it remains unclear to which degree could uncertainties in meteorological data influence the provided results.

The other explanation of overestimation would be a poor calibration of the model. Ceglar et al. (2019) demonstrated the importance of model calibration in the case of winter wheat for regional modelling. The calibration process, including the sowing date adjustment, vernalization, and calibration of phenology, lead to better simulation in the anthesis simulation. Kersebaum et al. (2015) described that the model uncertainty increases with the size of the area, which is investigated since data for testing and evaluation are not usually available. The model calibration of this research was done with field observation data describing the standard state variables and fluxes of the research area. One could speculate that such calibration can be defined as poor and high-quality field observations that should be carried out in future research to decrease the uncertainty during the modelling.

Also, the validation of calibration could be beneficial for the crop modelling. Also, the chosen water-limited production could underestimate the decrease of yield due to the unconcern of nutrients. The WOFOST can simulate the nutrient-limited production, considering the amount of nitrogen, phosphorus, and potassium (NPK). However, these data were not collected during the field observations. Also, the NPK module for WOFOST is relatively new, and no research outcomes are provided for comparison between the water-limited and nutrient-limited production. Kulig et al. (2020) provided some outputs, which can partly reveal the impact of model limitation levels on the forecasted crop production. They found out that water-limited production provides almost 40 % lower results than the potential production. Haberle & van Diepen (2001) also found that the difference between the water-limited and potential production can be 19% (de Wit et al. 2020).

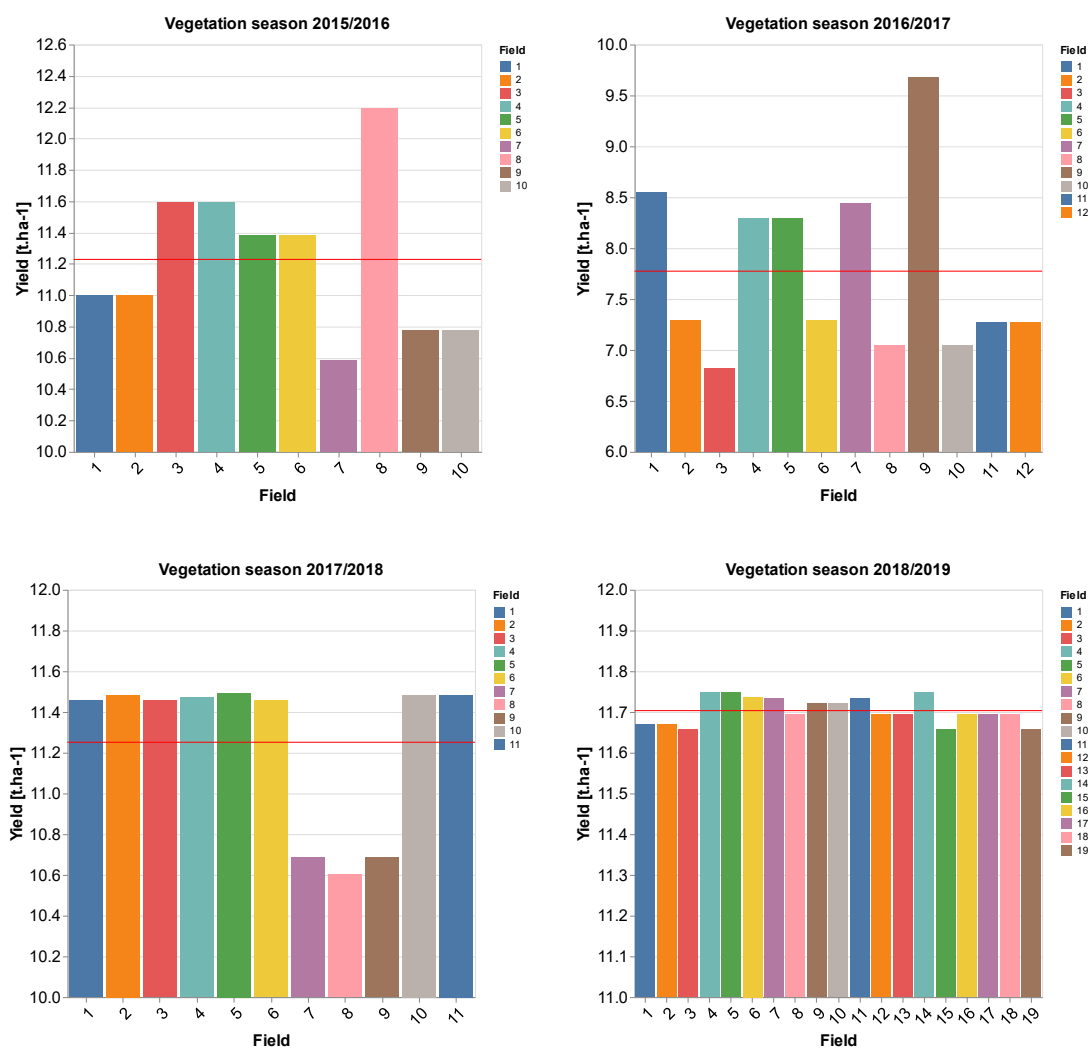


Figure 34. Final yield for wheat growth modelling (2015 – 2019).

The simulated LAIs for wheat in observed vegetation seasons can be seen in **Figure 35**. The average simulated LAI was 0.91, 0.48, 1.17, and 2.56 $\text{m}^2.\text{m}^{-2}$ between the seasons 2015/2016 – 2018/2019. The standard deviation was 1.34, 0.70, 1.93, and 2.1 $\text{m}^2.\text{m}^{-2}$. The maximum LAI was obtained in season 2018/2019 with the value of 7.11. While the first three seasons seem to be providing a reasonable estimate of LAI, the LAI for season 2018/2019 is very likely overestimated (Afrasiabian et al. 2021; Kumari et al. 2009; Palosuo et al. 2011; Yesilkoy et al. 2015). The Boogaard et al. (2013) presented the maximum LAI in Europe in 1990 – 2006 for autumn-sown wheat and found that wheat with LAI values can be found generally in the northern Europe, while Czechia's maximum potential was around 5 – 6 $\text{m}^2.\text{m}^{-2}$. Another uncertain finding was that vegetation season 2018/2019, which has unlikely development of LAI through the first part of vegetation season (i.e., October, December, February, and April). This is

particularly important when investigating the maximum LAI in this season. The author of this study speculated that such a high LA value just might be due to the steep development of LAI (Afrasiabian et al. 2021; Kumari et al. 2009; Pohanková 2016; Yesilkoy et al. 2015).

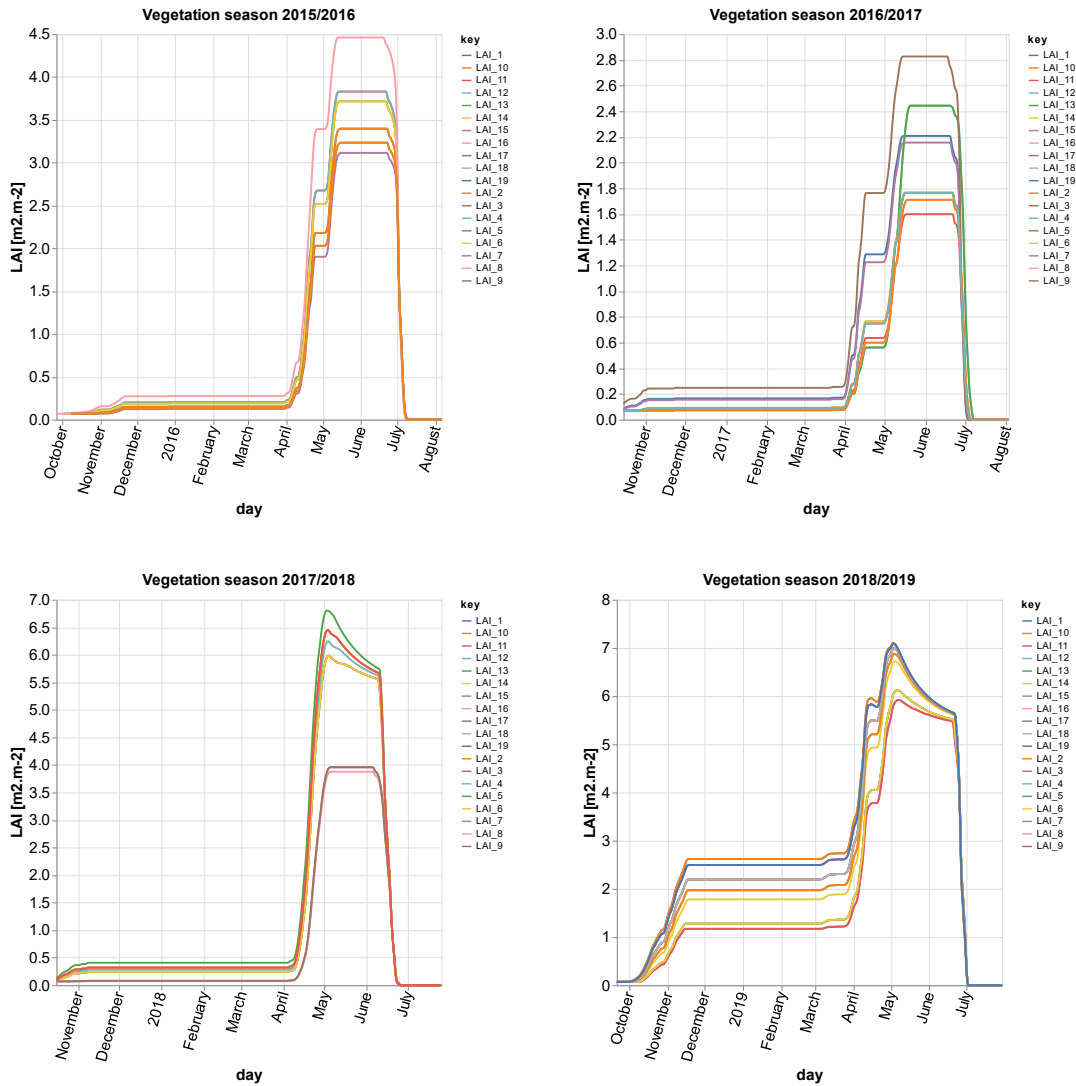


Figure 35. LAI development, simulation of WOFOST (2015 – 2019)

6.6 Assimilation of satellite data into the crop model

6.6.1 Ensemble Kalman Filter – Sentinel-2’s Leaf Area Index assimilation

Firstly, the WOFOST model was launched for simulations of wheat growth on 52 fields with EnKF data assimilation of LAI obtained from Sentinel-2. The Ensemble size was $n = 50$, so 2600 simulations were performed. The ensemble simulation was performed

according to the uncertainty described in 5.4.2. The **Annex - Fig. V.** provides an overview of Gaussian random variables results, which determine the development of the ensemble model.

The process of ensemble simulations is depicted in **Figure 36.** Due to the number of simulations and the number of the fields, the only results for Field ID 1 are depicted. It can also be mentioned that some planned observations were not used due to technical errors described earlier in 6.3. As can one notice, the Gaussian random variables changed the LAI development through the vegetation season. The satellite observations of LAI then adjusted the development of the entire ensemble by Kalman filter. Careful observations reveal that EnKF changed the development of LAI significantly. Such change can be seen during the vegetation season 2018/2019 in May, where a drop of simulated LAI was caused by three consequent observations. The average of the ensemble is then considered as the main result. The average simulated LAI was 1.43, 0.96, 1.12, and 2.71 between the seasons 2015/2016 – 2018/2019. The standard deviation was 0.13, 0.24, 0.24 and 0.52 $\text{m}^2.\text{m}^{-2}$. The maximum LAI was measured with values of 2.78 $\text{m}^2.\text{m}^{-2}$ (sowing date 21.9.2018). The yield results after the performed simulation for every vegetation season can be seen in **Figure 37** and in **Table 14, 15, 16, and 17.** The average yield was 11.42, 9.41, 10.31, and 9.88 t ha^{-1} for monitored seasons 2015/2016 – 2018/2019. The maximum obtained yield was 11.45 t ha^{-1} for several sowing dates in the year 2016, and the minimum yield was 9.21 t ha^{-1} obtained on sowing date 7.10.2016. The RMSE and MAE were 3.44 t ha^{-1} and 3.17 ha^{-1} for yield forecasting, respectively. The final comparison and discussion of results are presented in **chapter 6.6.3.**

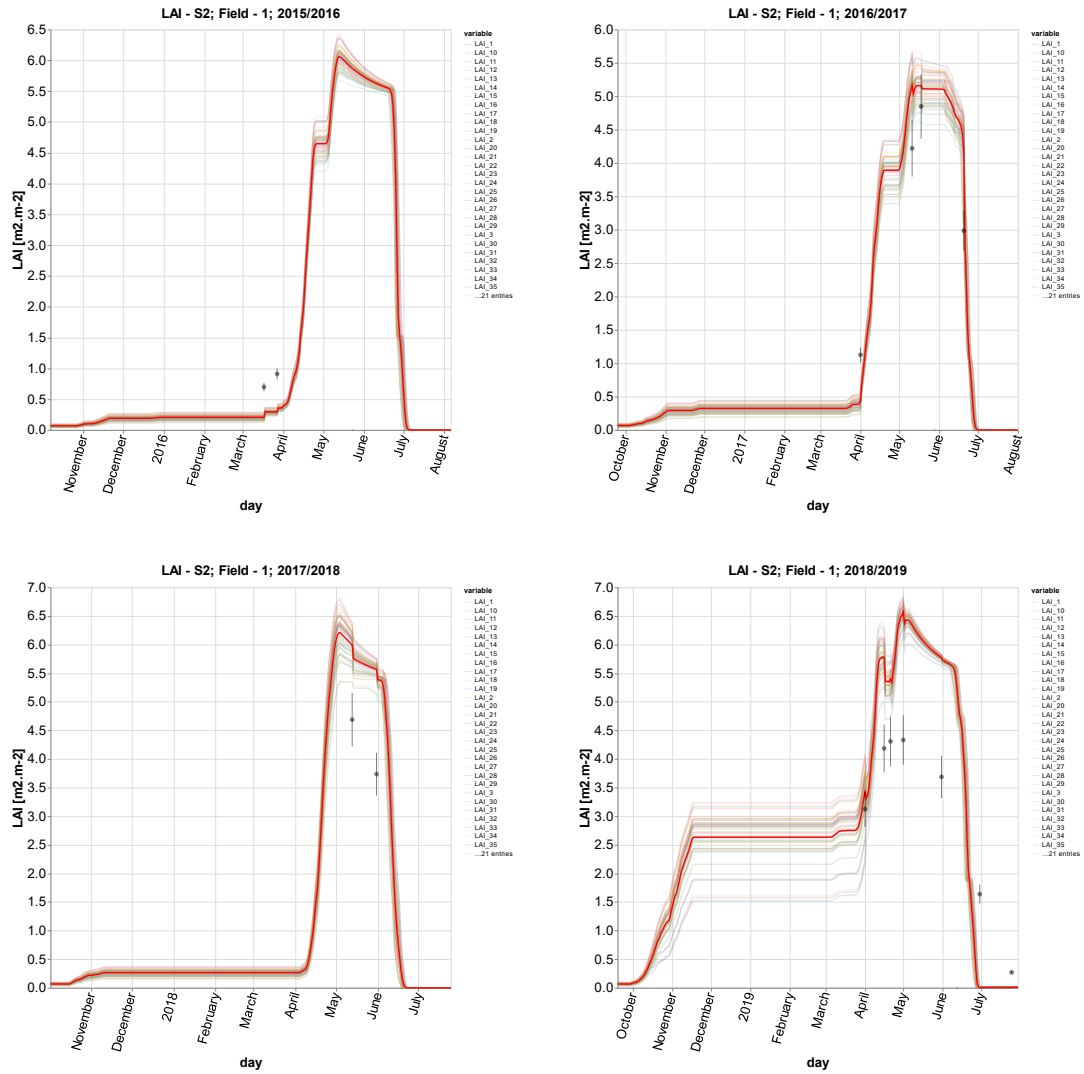


Figure 36. LAI development, Wheat field ID 1; Model Ensemble (transparent lines), Model Ensemble Mean (red line), LAI observations from Sentinel-2 with 10 % error (black circles).

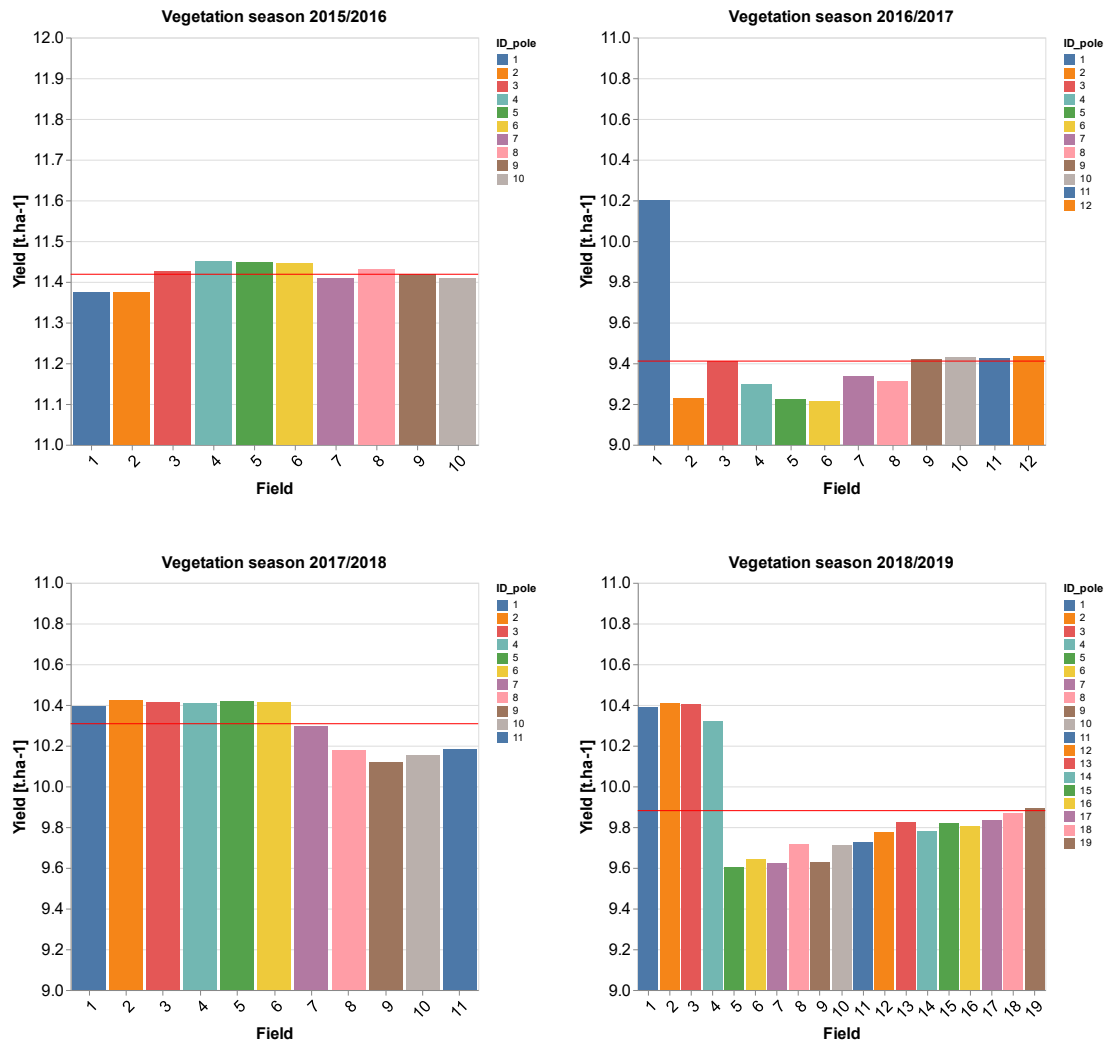


Figure 37. Final yield for wheat growth modelling after the LAI data assimilation from Sentinel-2 (2015 – 2019).

6.6.2 Ensemble Kalman Filter – Sentinel-1's Leaf Area Index assimilation

Secondly, the WOFOST model performed 2600 simulations, similarly as discussed in 6.6.1, however with EnKF data assimilation of R-LAI obtained from Sentinel-1. The modes used the same uncertainty as previous data assimilation. **Annex - Fig. V.** provides an overview of Gaussian random variables results.

The Sentinel-1 EnKF simulation can be seen in **Figure 38**. Due to the number of simulations and the number of fields, the only results for Field ID 1 are depicted. Compared to the previous assimilation, much more observations were used for adjustment of LAI. The ensemble model changed the simulation in exactly the same way as in previous data assimilation. The predicted R-LAI from Sentinel-1 then adjusted the development of the entire model ensemble by Kalman filter. As can be seen, the R-LAI observations changed the simulated LAI in every possible match. Comparing S1 assimilation to EnKF, it seems that changes were fluent as the number of observations was significantly larger. The sudden drops were not observed during the simulation. Nevertheless, it seems that some simulations (e.g., 2016/2017, 2018/2019) went through the sudden increase of LAI values in June/July (time of maturity) after the development already (almost) reached zero value. It is evident that this phenomenon is caused by the rising R-LAI at the end of phenological development. The average of the ensemble is then considered as the main result. The average simulated LAI was 1.47, 1.14, 1.29, and 2.05 $\text{m}^2 \cdot \text{m}^{-2}$ between the seasons 2015/2016 – 2018/2019. The standard deviation was 0.12, 0.20, 0.21 and 0.33. The maximum LAI was measured with values of 2.61 $\text{m}^2 \cdot \text{m}^{-2}$ (sowing date 27.9.2018). The yield results after the performed simulation for every vegetation season can be seen in **Figure 39** and in **Table 14, 15, 16, and 17**. The average yield was 11.44, 9.70, 10.35, and 10.35 $\text{t} \cdot \text{ha}^{-1}$ for monitored seasons 2015/2016 – 2018/2019. The maximum obtained yield was 11.47 $\text{t} \cdot \text{ha}^{-1}$ for several sowing dates in the year 2016, and the minimum yield was 9.43 $\text{t} \cdot \text{ha}^{-1}$ obtained on sowing date 17.10.2016. The RMSE and MAE were 3.66 $\text{t} \cdot \text{ha}^{-1}$ and 3.31 $\text{t} \cdot \text{ha}^{-1}$ for yield forecasting, respectively. The final comparison and discussion of results are presented in **chapter 6.6.3**.

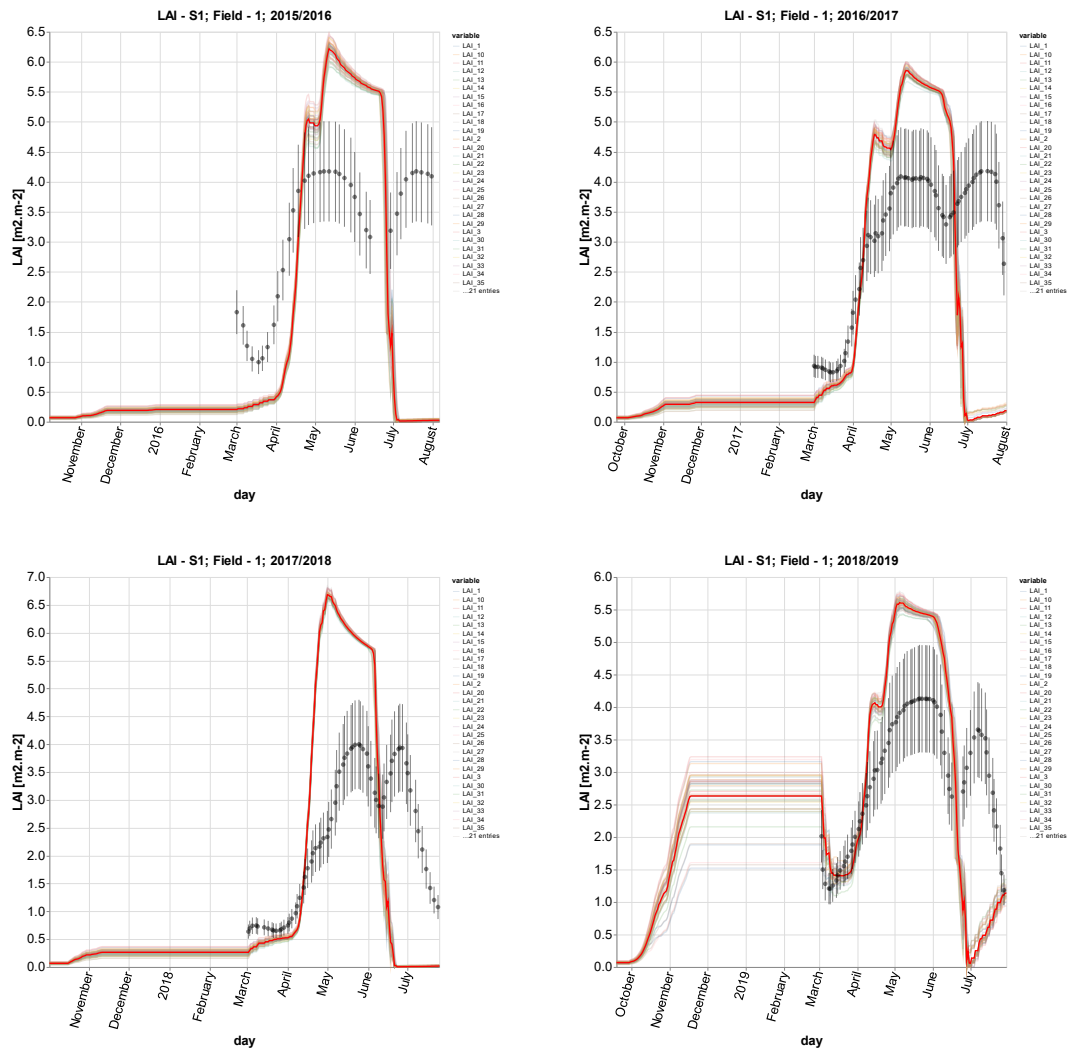


Figure 38. LAI development, Wheat field ID 1; Model Ensemble (transparent lines), Model Ensemble Mean (red line), LAI observations from Sentinel-1 with 20 % error (black circles).

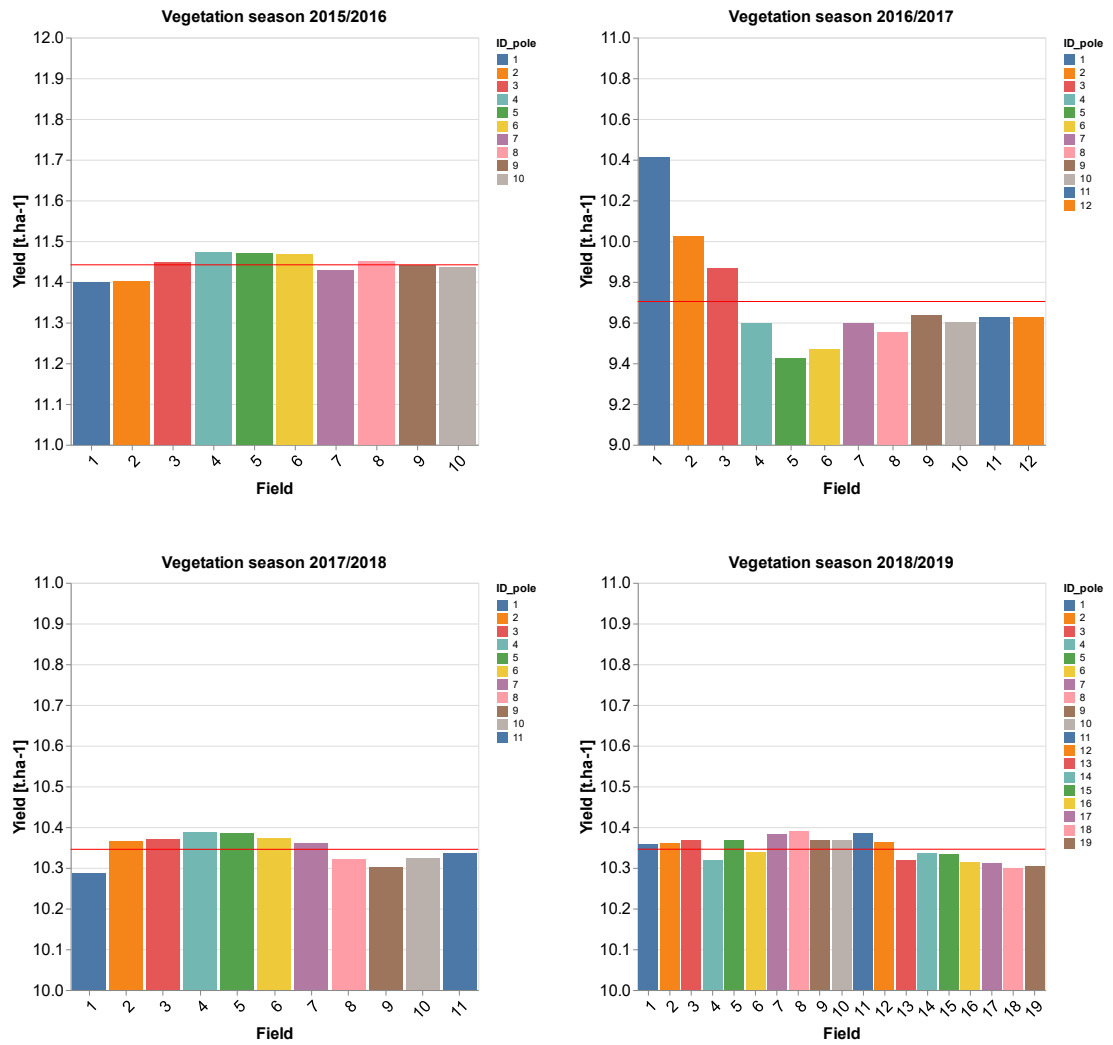


Figure 39. Final yield for wheat growth modelling after the LAI data assimilation from Sentinel-1 (2015 – 2019).

6.6.3 Final evaluation and discussion of data assimilation methods

The final part deals with the comparison of simulated (forecasted) results for crop modelling only, crop modelling with EnKF data assimilation of LAI derived from Sentinel-2 (EnKF S2 modelling), and crop modelling with EnKF data assimilation of LAI derived from Sentinel-1 (EnKF S1 modelling). **Tables 14, 15, 16, and 17** provide the comparison of different simulations.

Results for the year 2016 recorded a very large overestimation for crop modelling, EnKF S2 modelling, and EnKF S1 modelling. The percentage change ranged from 42.18 % to 106 % increase for crop modelling. The EnKF S2 modelling percentage change ranged from 50.64 % up to a 122.82 % increase. The EnKF S1 modelling for the year 2016 provided the percentage change ranges from 50.93 % - 123.61 %. Considering the only year 2016, the RMSE and MAE were 5.03 and 4.94 t.ha⁻¹ for crop modelling, 5.19 t.ha⁻¹ and 5.13 t.ha⁻¹ for EnKF S2 modelling, and 5.22 ha⁻¹ and 5.15 t.ha⁻¹ EnKF S1 modelling.

The year 2017 provided more promising results than the year 2016 for crop modelling, however, the EnKF was not able to increase the accuracy of modelling. The percentage change ranged from -35.80 % decrease to 51.19 % increase for crop modelling. The EnKF S2 modelling changed the forecasting, and the percentage changes range from -14.04 % decreased up to 91.41 % increase. The EnKF S1 modelling for the year 2016 recorded the percentage change ranges from -12.45 decrease – 108 % increase. The RMSE and MAE was 1.57 and 1.14 t.ha⁻¹ for crop modelling, 1.84 t.ha⁻¹ and 1.60 t.ha⁻¹ for EnKF S2 modelling and 2.14 t.ha⁻¹ and 1.86 t.ha⁻¹ EnKF S1 modelling.

The outputs for the year 2018 provide overestimation for modelling; nevertheless both EnKF methods were able to increase the accuracy of modelling and decrease the uncertainty. The percentage change ranges from 25.20 % to 71.14 % increase for crop modelling. The EnKF S2 modelling altered the forecasting and the percentage changes ranged from 13.49 % decrease up to 58.34 % increase. The EnKF S1 modelling gathered the percentage change ranged from 13.10 % – 59.38 % increase. The RMSE and MAE was 3.76 and 3.68 t.ha⁻¹ for crop modelling, 2.87 t.ha⁻¹ and 2.73 t.ha⁻¹ for EnKF S2 modelling and 2.93 t.ha⁻¹ and 2.78 t.ha⁻¹ EnKF S1 modelling.

At last, the results for the year 2019 provide a similarly large overestimation for modelling as the year 2016. However, both EnKF methods were able to decrease the error of the

model. The percentage change ranged from 35.16 % to 193.69 % increase for crop modelling. The percentage changes ranged from 12.05 % up to 139.99 % increase for the EnKF S2 modelling. The EnKF S1 modelling recorded the percentage change ranged from 19.63 % – 159.20 % increase. The RMSE and MAE was 5.10 and 4.92 t.ha⁻¹ for crop modelling, 3.36 t.ha⁻¹ and 3.09 t.ha⁻¹ for EnKF S2 modelling and 3.81 t.ha⁻¹ and 3.56 t.ha⁻¹ EnKF S1 modelling.

Table 14. 2016 - Comparison of observed yield, crop modelling and crop modelling with EnKF assimilation methods.

Field_ID	Sowing date	Yield [t.ha⁻¹]	Crop modelling [t.ha⁻¹]	ENKF S2 modelling [t.ha⁻¹]	ENKF S1 modelling [t.ha⁻¹]
1	7/10/2015	5.84	11.00	11.38	11.40
2	7/10/2015	5.84	11.00	11.38	11.40
3	2/10/2015	5.12	11.59	11.42	11.45
4	2/10/2015	6.89	11.59	11.45	11.47
5	4/10/2015	6.14	11.38	11.45	11.47
6	4/10/2015	6.35	11.38	11.45	11.47
7	11/10/2015	5.12	10.59	11.41	11.43
8	26/9/2015	6.63	12.19	11.43	11.45
9	8/10/2015	7.58	10.78	11.42	11.44
10	8/10/2015	7.36	10.78	11.41	11.43

Table 15. 2017 - Comparison of observed yield, crop modelling and crop modelling with EnKF assimilation methods.

Field_ID	Sowing date	Yield [t.ha⁻¹]	Crop modelling [t.ha⁻¹]	ENKF S2 modelling [t.ha⁻¹]	ENKF S1 modelling [t.ha⁻¹]
1	25/9/2016	8.13	8.55	10.20	10.41
2	7/10/2016	4.82	7.29	9.23	10.03
3	11/10/2016	8.10	6.82	9.41	9.87
4	17/10/2016	8.46	8.30	9.30	9.59
5	17/10/2016	8.42	8.30	9.22	9.43
6	7/10/2016	7.76	7.29	9.21	9.47
7	26/9/2016	8.03	8.44	9.34	9.60
8	15/10/2016	7.92	7.04	9.31	9.55
9	22/9/2016	7.83	9.68	9.42	9.64
10	15/10/2016	10.97	7.04	9.43	9.60
11	8/10/2016	8.24	7.27	9.42	9.63
12	8/10/2016	8.11	7.27	9.44	9.63

Table 16. 2018 - Comparison of observed yield, crop modelling and crop modelling with EnKF assimilation methods.

Field_ID	Sowing date	Yield [t.ha⁻¹]	Crop modelling [t.ha⁻¹]	ENKF S2 modelling [t.ha⁻¹]	ENKF S1 modelling [t.ha⁻¹]
1	2/10/2017	8.33	11.46	10.39	10.29
2	30/9/2017	8.73	11.48	10.42	10.36
3	2/10/2017	7.55	11.46	10.41	10.37
4	1/10/2017	8.05	11.47	10.41	10.39
5	28/9/2017	9.18	11.49	10.42	10.38
6	2/10/2017	8.33	11.46	10.41	10.37
7	15/10/2017	6.50	10.68	10.29	10.36
8	16/10/2017	6.56	10.60	10.18	10.32
9	15/10/2017	6.50	10.68	10.12	10.30
10	30/9/2017	6.71	11.48	10.15	10.32
11	30/9/2017	6.82	11.48	10.18	10.34

Table 17. 2019 - Comparison of observed yield, crop modelling and crop modelling with EnKF assimilation methods.

Field_ID	Sowing date	Yield [t.ha⁻¹]	Crop modelling [t.ha⁻¹]	ENKF S2 modelling [t.ha⁻¹]	ENKF S1 modelling [t.ha⁻¹]
1	19/9/2018	5.67	11.67	10.39	10.36
2	19/9/2018	8.61	11.67	10.41	10.36
3	20/9/2018	8.54	11.66	10.40	10.37
4	26/9/2018	6.00	11.75	10.32	10.32
5	26/9/2018	4.00	11.75	9.60	10.37
6	23/9/2018	6.40	11.74	9.64	10.34
7	27/9/2018	5.38	11.73	9.62	10.38
8	21/9/2018	7.60	11.69	9.71	10.39
9	22/9/2018	6.00	11.72	9.63	10.37
10	22/9/2018	7.00	11.72	9.71	10.37
11	27/9/2018	8.68	11.73	9.73	10.38
12	21/9/2018	7.48	11.69	9.77	10.36
13	21/9/2018	6.77	11.69	9.82	10.32
14	26/9/2018	6.40	11.75	9.78	10.33
15	20/9/2018	8.59	11.66	9.82	10.33
16	21/9/2018	5.26	11.69	9.80	10.31
17	21/9/2018	5.26	11.69	9.83	10.31
18	21/9/2018	6.77	11.69	9.87	10.30
19	20/9/2018	8.54	11.66	9.89	10.30

The overall assessment of crop modelling and crop modelling with assimilation methods can be seen in **Table 18**. The crop modelling of wheat by WOFOST gathered a large overestimation of the final yield resulted in RMSE of 4.23 and MAE of 3.79. After that, the forecast was adjusted by EnKF LAI data assimilation originated from Sentinel-2 satellite. This method decreased the uncertainty of the model by 0.8 t ha⁻¹ for RMSE and by 0.72 t.ha⁻¹ for MAE. Subsequently, the data assimilation of predicted R-LAI originated from Sentinel-1 were used for the update of crop modelling forecast, and this method decreased the error of the model by 0.57 t.ha⁻¹ for RMSE, and by 0.48 t.ha⁻¹ for MAE; however, this method did not overcome the EnKF S2 modelling. The fluency (smoothness) of adjusted LAI development was also analyzed by descriptive statistics. The absolute maximum change of LAI between days during the wheat growth was obtained from every ensemble simulation of the EnKF S1 and S2 modelling. The average maximum change for every wheat field was then calculated with a value of 1.10 for EnKF S2 modelling and a value of 1.09 for EnKF S1 modelling. Considering the highest absolute maximum change during the modelling, the EnKF S1 modelling provided 2.24 increment, while the EnKF S2 modelling provided 2.57 increment.

Table 18. RMSE and MAE for observed yield and crop modelling methods.

	RMSE [t.ha ⁻¹]	MAE [t.ha ⁻¹]
Crop modelling, obs. yield	4.23	3.79
Crop modelling + EnKF S2, obs. yield	3.43	3.07
Crop modelling + EnKF S1, obs. yield	3.66	3.31

The Remote sensing data assimilation into the crop model WOFOST was presented by many authors. From the perspective of WOFOST, EnKF, and simulation of winter wheat, Pan et al. (2019) recently demonstrated the join data assimilation of LAI and soil moisture from Sentinel-1 and Sentinel-2 into the WOFOST by EnKF for winter wheat. They were able to decrease the RMSE from 0.47 t.ha⁻¹ to 0.31 t.ha⁻¹ at field level and from 1.87 t.ha⁻¹

¹ to 0.71 t.ha⁻¹ at regional scale. Ma et al. (2013) tried to use the NVDI data for adjustment of the WOFOST with EnKF in the mode of potential production and presented the decrease of RMSE from 2.17 t.ha⁻¹ to 0.78 t.ha⁻¹. However, they also tried water-limited simulation, and their RMSE results increased from 1.63 t.ha⁻¹ to 3.01 t.ha⁻¹. Wang et al. (2017) presented that MODIS LAI assimilation can have a positive impact on crop modelling and change the RMSE from 0.59 to 0.36 t.ha⁻¹. Beyene et al. (2021) coupled the remote sensing (MODIS LAI) and crop growth model and demonstrated the decrease of RMSE from 0.59 t.ha⁻¹ to 0.41 t.ha⁻¹ at a regional scale. Huang et al. (2016 - a) were able to create LAI product by using Landsat TM and MODIS and subsequently adjust the regional forecasting of winter wheat. The reduction of uncertainty (RMSE) was reduced from 0.65 to 0.44 t.ha⁻¹. The use of Sentinel-1 and Sentinel-2 for WOFOST crop modelling was also examined by Zhuo et al. (2018), which tried to derive the soil moisture from the so-called water cloud model and adjust the simulation of winter wheat by EnKF. Results of their study indicated that improvements of WOFOST modelling are quite low (RMSE 0.60 t.ha⁻¹ for crop modelling compared to RMSE 0.36 t.ha⁻¹ for data assimilation). Compared to our study, the presented crop modelling of wheat provides smaller RMSE during the modelling; however, almost all these presented studies (uncertain with Zhuo et al. (2018)) used the meteorological data from the weather/meteorological stations in surroundings of research sites. This could be a significant difference between the approach of this study and studies of other authors. Also, it seems that while a decrease of RMSE was quite low in the case of this study, the decrease of RMSE was more significant in discussed studies. This implies that the results of this research should be considered as cautiously acceptable as the effects of data assimilation were quite low.

7. Conclusions

Remote sensing and crop growth modelling represent the developing fields of study, which can jointly provide a powerful tool for agricultural/environmental observation and monitoring. The Copernicus programme of the European Space Agency offers easily accessible and continuous Earth Observation data by Earth Observation missions and Contributing missions. The Sentinel missions Sentinel-1 and Sentinel-2 monitor are able to monitor the Earth's surface by optical and radar instruments. The aim of this study was to examine the relation between the optical indices (NDVI, LAI) obtained from Sentinel-2 and RVI obtained from Sentinel-1 and use them for purposes of crop modelling.

The wheat fields were monitored with Sentinel-1 and Sentinel-2 (complemented by Landsat 8) between the years 2015 and 2019 and then analyzed. The calculated NDVI from the optical instrument and RVI obtained from SAR instruments were compared by descriptive statistics and linear regression. The results showed that RVI seems to have a similar development to the phenological curve. The radar data from the Sentinel-1 mission could supplement optical satellite data to a certain degree. However, whether Sentinel-1 radar data can fully replace optical data during vegetation monitoring is still uncertain. Also, the anisotropy of the backscatter caused by different incidence and azimuthal angles should be considered during vegetation analysis from the Sentinel-1 timeseries. It seems that Sentinel-1's Relative orbit and platform were crucial for such an approach and better results.

The subsequent research examined the application of RVI data in WOFOST crop growth modelling. The Savitzky–Golay filter was used for the filtration of RVI data and suppression of impacts of a monitoring from different Relative orbits and Sentinel-1's platforms. The later comparison of accuracy during the use of Random Forest Regression provided better results for filtered RVI data. Broadly translated this finding indicate that the SG filtering could be important tool during the RVI analysis and provide better outcomes of vegetation monitoring by radar data. Also, discussed the difference between the RVI, backscatter, and optical indices development during the vegetation season revealed the necessity to examine the relations more thoroughly. The Machine learning, specifically the Random Forest Regression, was used for the prediction of R-LAI using the LAI as predictor and RVI as a feature. This method resulted in not a such promising relationship between the LAI and RVI; however, the general similarity of seasonal

development could be found between LAI and resulting R-LAI. The implication of that is the this approach of LAI prediction is not reliable, however it is a good starting point for future research investigation and improvement of prediction.

The crop growth model research activities were done for wheat crop growth without and with data assimilations of LAI and R-LAI. The results of crop growth modelling demonstrated a quite high overestimation of the WOFOST. The data assimilation by EnKF of LAI originated from Sentinel-2 to the model provided better wheat yield forecasting. The R-LAI product resulting from Sentinel-1 was also used for the update of the model with better outputs than crop modelling; however, worse than with optical data. This partially rejected the **Hypothesis 1**. However, the **Hypothesis 2** could be fully confirmed as a sequential update of the model adjusted the simulated LAI more fluently (smoothly). The overall, the results demonstrate that using data assimilation of radar data can be beneficial during the crop growth modelling and increase accuracy of yield predictions. Other important find is that radar data can alter simulation more fluently with increased accuracy of modelling than the optical data.

The presented research was performed in the conditions of the Czech Republic; nevertheless, it is obvious that the finding can be applied globally.

8. Recommendations for further research

Further research in the usage of remote sensing data for the purpose of agricultural/environmental monitoring and crop modelling is highly recommended. The recommendations can be distinguished on potential improvements/better understating originated directly from results and on improvements/better understanding from results and discussion with other authors. The recommendations from the results are as follows:

- The use of S-G filtering can provide potential improvement in the quality of predicted LAI from Sentinel-1 data as predicted R-LAI have a similar basic shape as LAI.
- Assessment of different filtering methods or mathematical operations adjusting the RVI index according to the used Relative orbits and platforms should be conducted.
- Comparing the RVI with canopy water content (e.g., normalized difference water index from optical sensors, ground measurements), since the coefficient of determination provides only weak or moderate goodness-of-fit between RVI and NDVI (Tuma et al. 2021), is desired.
- Structured assessment of relations between RVI and LAI (and NDVI) in different parts of the vegetation season and utilization of results for crop modelling could be beneficial.
- The analysis of different methods of SAR data speckle filtering and their impact on quality of RVI spatial distribution is needed.

From the results and subsequent discussion arise these study questions:

- The relation between the SAR's backscatters (Cross-ratio or Direct-ratio) and RVI (originated from SAR's backscattering) should be analysed, since RVI and backscatter behave differently in each part of vegetation season.
- The comparison and evaluation of crop growth simulation based on different Reanalysis data (e.g., NASA POWER, ERA5) and meteorological data originated from meteorological stations could clarify the sensitivity of the WOFOST (and other crop growth models) to different weather inputs.
- Better understanding of reanalysis data's limits in context of spatial usage during the crop growth modelling could be beneficial for future research.

- Assessment of NPK module on simulated nutrient-limited production of the WOFOST is recommended.

9. References

- Aboelkhair H, Morsy M, Afandi GE. 2019. Assessment of agroclimatology NASA POWER reanalysis datasets for temperature types and relative humidity at 2 m against ground observations over Egypt. *Advances in Space Research* 64: 129-142 DOI: 10.1016/j.asr.2019.03.032.
- Abrahamsen P, Hansen S. 2000. Daisy: an open soil-crop-atmosphere system model. *Environmental Modelling & Software* 15:313-330 DOI: 10.1016/S1364-8152(00)00003-7.
- Afrasiabian Y, Noory H, Mokhtari A, Nikoo RM, Pourshakouri F, Haghghatmehr P. 2021. Effects of spatial, temporal, and spectral resolutions on the estimation of wheat and barley leaf area index using multi- and hyper-spectral data. *Precision Agriculture* 22:660-668.
- Arshad Muhammad, Ma X, Yin J, Ullah W, Liu Mengyang, Ullah I. 2021. Performance evaluation of ERA-5, JRA-55, MERRA-2, and CFS-2 reanalysis datasets, over diverse climate regions of Pakistan. *Weather and Climate Extremes* 33 (100373) DOI: 10.1016/j.wace.2021.100373
- AIRBUS. 2020. Happy birthday Sentinel-2A: Five Years of Environmental Insights. AIRBUS. Available from <https://www.airbus.com/en/newsroom/press-releases/2020-06-happy-birthday-sentinel-2a-five-years-of-environmental-insights> (accessed November 2021).
- Ayyoob KC, Krishnadas M. 2013. Production forecast of groundnut (*Arachis hypogaea* L.) using crop yield-weather model. *Agriculture Update* 8:436-439.
- Baghdadi N, Cresson R, Pottier E, Aubert M, Zribi M, Jacome A, Benabdallah SC. 2011. A Potential Use for the C-Band Polarimetric SAR Parameters to Characterize the Soil Surface Over Bare Agriculture Fields. *IEEE Transactions on Geoscience and Remote Sensing* 50:3844-3858 DOI: 10.1109/TGRS.2012.2185934.
- Bai J, Chen X, Dobermann A, Yang H, Cassman KG, Zhang F. 2010. Evaluation of NASA Satellite- and Model-Derived Weather Data for Simulation of Maize Yield Potential in China. *Agronomy Journal* 102:9-16 DOI: 10.2134/agronj2009.0085.
- Bai T, Wang S, Meng W, Zhang N, Wang T, Chen Y, Mercatoris B. 2019. Assimilation of Remotely-Sensed LAI into WOFOST Model with the SUBPLEX Algorithm for

- Improving the Field-Scale Jujube Yield Forecasts. *Remote Sensing* 11: (1945) DOI: 10.3390/rs11161945.
- Baruth B, Leo O. 2009. The MARS Crop Yield Forecasting System – introduction by JRC. Joint Research Centre, Institute for the Protection and Security of the Citizen, Monitoring Agricultural Resources Unit (MARS). Available from <https://edepot.wur.nl/11213> (accessed November 2021)
- Basso B, Cammarano D, Carfagna E. 2013. Review of Crop Yield Forecasting Methods and Early Warning Systems. Available from http://www.fao.org/fileadmin/templates/ess/documents/meetings_and_workshops/GS_SAC_2013/Improving_methods_for_crops_estimates/Crop_Yield_Forecasting_Methods_and_Early_Warning_Systems_Lit_review.pdf (accessed October 2021).
- Basso B, Liu L. 2018. Seasonal crop yield forecast: Methods, applications, and accuracies. *Advances in Agronomy* 154: 201-255 DOI: 10.1016/bs.agron.2018.11.002.
- Bassu S, Fumagalli D, Toreti A, Ceglar A, Giunta F, Motzo R, Zajac Z, Niemeyer S. 2021. Modelling potential maize yield with climate and crop conditions around flowering. *Field Crops Research* 271 (108226) DOI: 10.1016/j.fcr.2021.108226.
- Beriaux E, Lucau-Danila C, Auguiere E, Defourny P. 2013. Multiyear independent validation of the water cloud model for retrieving maize leaf area index from SAR time series. *International Journal of Remote Sensing*: 34: 4156-4181 DOI: 10.1080/01431161.2013.772676.
- Bériaux E, Lambot S, Defourny P. 2014. Estimating surface-soil moisture for retrieving maize leaf-area index from SAR data. *Canadian Journal of Remote Sensing* 37: 136-150 DOI: 10.5589/m11-021.
- Bernardi M, Delince J, Durand W, Zhang N. 2016. Crop Yield Forecasting: Methodological and Institutional Aspects. Food and Agriculture Organization of The United Nations (FAO). Rome.
- Beyene NA, Zeng H, Wu B, Zhu L, Gebremicael G, Zhang M, Bezabh T. 2021. Coupling remote sensing and crop growth model to estimate national wheat yield in Ethiopia. *Big Earth Data*. DOI: 10.1080/20964471.2020.1837529.
- Blaes X, Defourny P, Wegmuller U, Vecchia AD, Guerriero L, Ferrazzoli P. 2006. C-band polarimetric indexes for maize monitoring based on a validated radiative

- transfer model. *IEEE Transactions on Geoscience and Remote Sensing* 44: 791-800
DOI: 10.1109/TGRS.2005.860969
- Bochenek Z, Dąbrowska-Zielińska K, Gurdak R, Niro F, Bartold M, Grzybowski P. 2017. Validation of the LAI biophysical product derived from Sentinel-2 and Proba-V images for winter wheat in western Poland. *Geoinformation Issues* 9: 15-26. Available from <http://www.igik.edu.pl/upload/File/wydawnictwa/GI9BochenekZ.pdf> (accessed October 2021).
- Bolten JD, Crow WT, Zhan X, Jackson TJ, Reynolds CA. 2010. Evaluating the Utility of Remotely Sensed Soil Moisture Retrievals for Operational Agricultural Drought Monitoring. *IEEE Journal of Selected Topics in Applied Earth Observations and Remote Sensing* 3: 57-66 DOI: 10.1109/JSTARS.2009.2037163.
- Boogaard HL, de Wit AJW, te Roller JA, van Diepen CA, Rooter RP, Cabrera JMCA, Van Laar HH. 2014. WOFOST Control Centre 2.1 and WOFOST 7.1.7. Alterra, Wageningen University & Research Centre, Wageningen.
- Boogaard H, Wolf J, Supit I, Niemeyer S, van Ittersum M. 2013. A regional implementation of WOFOST for calculating yield gaps of autumn-sown wheat across the European Union. *Field Crops Research* 143: 130-142 DOI: 10.1016/j.fcr.2012.11.005.
- Boote KJ, Porter C, Jones JW, Thorburn PJ, Kersebaum KC, Hoogenboom G, White JW, Hatfield JL. 2016. Sentinel site data for crop model improvement - definition and characterization. Pages 125-128 in *Improving Modeling Tools to Assess Climate Change Effects on Crop Response 7. Advances in Agricultural Systems Modeling*. Madison, USA. DOI: 10.2134/advagricystmodel7.2014.0019.
- Bouman BAM. 1995. Crop modelling and remote sensing for yield prediction. *Wageningen Journal of Life Sciences* 43 DOI: 10.18174/njas.v43i2.573.
- Bouman BAM, van Keulen H, van Laar HH, Rabbinge. 1996. The 'School of de Wit' Crop Growth Simulation Models: A Pedigree and Historical Overview. *Agricultural Systems* 52:171-198 DOI: 10.1016/0308-521X(96)00011-X.
- Brisson N, Gary C, Justes E, Roche R, Mary R, Mary B, Ripoche D, Zimmer D, Sierra J, Bertuzzi P, Burger P, Bussi re F, Cabidoche YM, Cellier P, Debaeke P, Gaudill re JP, H nault C, Maraux F, Seguin B, Sinoquet H. 2003. An overview of the crop

- model STICS. *Europ. J. Agronomy* 18:309-332 DOI: 10.1016/S1161-0301(02)00110-7.
- Cai Zhanzhang, Jönsson P, Jin H, Eklundh L. 2017. Performance of Smoothing Methods for Reconstructing NDVI Time-Series and Estimating Vegetation Phenology from MODIS Data. *Remote Sensing* 9 (1271) DOI: 10.3390/rs9121271.
- Cambell JB, Wynne RH, Mesev V, Treitz P, Lawrence R. 2011. *Introduction to Remote Sensing*. Guilford Publications, New York. DOI: 10.3390/rs5010282.
- Canisius F, Shang J, Liu J, Huang X, Ma B, Jiao X, Geng X, Kovacs JM, Walters D. 2018. Tracking crop phenological development using multi-temporal polarimetric Radarsat-2 data. *Remote Sensing of Environment* 210:508-518 DOI: 10.1016/j.rse.2017.07.031.
- Ceglar A, van der Wijngaart, de Wit A, Lecerf R, Boogaard H, Seguini L, van der Berg M, Toreti A, Zampieri M, Fumagalli D, Buruth B. 2019. Improving WOFOST model to simulate winter wheat phenology in Europe: Evaluation and effects on yield. *Agricultural Systems* 168:168-180 DOI: 10.1016/j.agsy.2018.05.002.
- Chai T, Draxler RR. 2014. Root mean square error (RMSE) or mean absolute error (MAE)? – Arguments against avoiding RMSE in the literature. *Geoscientific Model Development* 7:1247-1250 DOI: 10.5194/gmd-7-1247-2014.
- Chakrabarti S, Bongiovanni T, Judge J, Zotarelli L, Bayer C. 2014. Assimilation of SMOS Soil Moisture for Quantifying Drought Impacts on Crop Yield in Agricultural Regions. *IEEE Journal of Selected Topics in Applied Earth Observations and Remote Sensing* 7:3867-3879 DOI: 10.1109/JSTARS.2014.2315999.
- Chang CH-T, Wang H-CH, Huang CH. 2013. Impacts of vegetation onset time on the net primary productivity in a mountainous island in Pacific Asia. *Environmental Research Letters* 8: (045030).
- Chang JG, Shoshany M, Oh Y. 2018. Polarimetric Radar Vegetation Index for Biomass Estimation in Desert Fringe Ecosystems. *IEEE Transactions on Geoscience and Remote Sensing* 56:7102-7108 DOI: 10.1109/TGRS.2018.2848285.
- Chen J, Jönsson P, Tamura M, Gu Z, Matsushita B, Eklundh L. 2004. A simple method for reconstructing a high-quality NDVI time-series dataset based on the Savitzky–Golay filter. *Remote Sensing of Environment* 91:332-344 DOI: 10.1016/j.rse.2004.03.014.

- Cheng Z, Meng J, Shang J, Liu J, Huang J, Qiao Y, Qian B, Jing Q, Dong T, Yu L. 2020. Generating Time-Series LAI Estimates of Maize Using Combined Methods Based on Multispectral UAV Observations and WOFOST Model. *Sensors* 20: (6006) DOI: 10.3390/s20216006.
- Climate Data Store (CDS). 2021. Soil moisture gridded data from 1978 to present. Available from <https://cds.climate.copernicus.eu/cdsapp#!/dataset/satellite-soil-moisture?tab=overview> (accessed November 2021).
- Crow WT, Wood EF. 2003. The assimilation of remotely sensed soil brightness temperature imagery into a land surface model using Ensemble Kalman filtering: a case study based on ESTAR measurements during SGP97. *Advances in Water Resources* 26:137-149 DOI: 10.1016/S0309-1708(02)00088-X.
- Curnel Y, de Wit JWA, Duveiller G, Defourny P. 2011. Potential performances of remotely sensed LAI assimilation in WOFOST model based on an OSS Experiment. *Agricultural and Forest Meteorology* 151:1843-1855 DOI: 10.1016/j.agrformet.2011.08.002.
- Copernicus. Not dated - a. Definitions (Sentinel-1). Available from <https://sentinels.copernicus.eu/web/sentinel/user-guides/sentinel-1-sar/definitions> (accessed November 2021).
- Copernicus. Not dated - b. Production Scenario (Sentinel-1). Available from <https://sentinels.copernicus.eu/web/sentinel/missions/sentinel-1/production-scenario> (accessed October 2021).
- Copernicus. Not dated - c. Overview (Sentinel-1). Available from <https://sentinels.copernicus.eu/web/sentinel/user-guides/sentinel-1-sar/overview> (accessed October 2021).
- Darvishzadeh R, Skidmore A, Schlerf M, Atzberger C, Corsi F, Cho M. 2008. LAI and chlorophyll estimation for a heterogeneous grassland using hyperspectral measurements. *Journal of Photogrammetry & Remote Sensing* 63:409-426 DOI: 10.1016/j.isprsjprs.2008.01.001.
- Denize J, Hubert-Moy L, Betbeder J, Corgne S, Baudry J, Pottier E. 2019. Evaluation of Using Sentinel-1 and -2 Time-Series to Identify Winter Land Use in Agricultural Landscapes. *Remote Sensing* 11: (37) DOI: 10.3390/rs11010037.
- de Kok R, Weżyk P, Papież M, Migo L. 2017. Applications of Sentinel-2 data for agriculture and forest monitoring using the absolute difference (ZABUD) index

- derived from the AgroEye software (ESA). SPIE Remote Sensing. Proceedings 10421, Remote Sensing for Agriculture, Ecosystems, and Hydrology XIX. Warsaw DOI: 10.1117/12.2277828.
- De Peppo M, Taramelli A, Boschetti M, Mantino A, Volpi I, Fillipponi F, Tornato A, Valentini E, Ragaglini G. 2021. Non-Parametric Statistical Approaches for Leaf Area Index Estimation from Sentinel-2 Data: A Multi-Crop Assessment. *Remote Sensing* 13: (2841) DOI: 10.3390/rs13142841.
- de Wit A. 2018. PCSE: The Python Crop Simulation Environment. Available from <https://pcse.readthedocs.io/en/stable/> (accessed October 2021).
- de Wit A, Abelleira D, Veron S, Kroes J, Supit I, Boogaard H. 2017. Technical description of crop model (WOFOST) calibration and simulation activities for Argentina, pampas region. Stimulating Innovation for Global Monitoring of Agriculture. Available from <https://edepot.wur.nl/441498> (accessed October 2021).
- de Wit A, Boogaard H, Fumagalli D, Janssen S, Knapen R, van Kraalingen D, Supit I, van der Wijngaart R, van Diepen K. 2018. 25 years of the WOFOST cropping systems model. *Agricultural systems* 168:154-167 DOI: 10.1016/j.agsy.2018.06.018.
- de Wit AJW, Boogaard HL, Supit I, van der Berg M. 2020. System description of the WOFOST 7.2 cropping systems model. Wageningen Environmental Research. Available from <https://edepot.wur.nl/522204> (accessed October 2021).
- de Wit AJW, van Diepen CA. 2007. Crop model data assimilation with the Ensemble Kalman filter for improving regional crop yield forecasts. *Agricultural and Forest Meteorology* 146:38-56 DOI: 10.1016/j.agrformet.2007.05.004.
- Deepak K. 2015. Remote Sensing based Vegetation Indices Analysis to Improve Water Resources Management in Urban Environment. *Aquatic Procedia*:1374 – 1380 DOI: 10.1016/j.aqpro.2015.02.178.
- Dempewolf J, Adusei B, Becker-Reshef I, Hansen M, Potapov P, Khan A, Barker B. 2014. Wheat Yield Forecasting for Punjab Province from Vegetation Index Time Series and Historic Crop Statistics. *Remote Sensing* 6:9653-9675 DOI: <https://doi.org/10.3390/rs6109653>.
- Di Paola A, Valentini R, Santinia M. 2015. An overview of available crop growth and yield models for studies and assessments in agriculture. *Journal of the Science of Food and Agriculture* 96:709-714 DOI: 10.1002/jsfa.7359.

- Djaby B, de Wit A, Kouadio L, Jarroudi ME, Tychon B. 2013. Spatial Distribution of Calibrated WOFOST Parameters and Their Influence on the Performances of a Regional Yield Forecasting System. *Sustainable Agriculture Research*: 2 DOI: 10.5539/sar.v2n4p12.
- Domijan k, jorgensen m, reid j. 2006. Semi-mechanistic modelling in nonlinear regression: a case study. *Australian & New Zealand Journal of Statistics* 48:373-379 DOI: 10.1111/j.1467-842X.2006.00446.x.
- Domínguez JA, Kumhálová J, Novák P. 2015. Winter oilseed rape and winter wheat growth prediction using remote sensing methods. *Plant Soil Environment* 61:410-416 DOI: 10.17221/412/2015-PSE.
- Domínguez JA, Kumhálová J, Novák P. 2017. Assessment of the relationship between spectral indices from satellite remote sensing and winter oilseed rape yield. *Agronomy Research* 15:055-068.
- dos Santos EP, Da Silva DD, de Amaral CH. 2021. Vegetation cover monitoring in tropical regions using SAR-C dual-polarization index: seasonal and spatial influences. *International Journal of Remote Sensing* 42:7581-7609 DOI: 10.1080/01431161.2021.1959955.
- Duarte YCN, Sentelhas PC. 2020. NASA/POWER and DailyGridded weather datasets—how good they are for estimating maize yields in Brazil? *International Journal of Biometeorology* 64:319-329 DOI: 10.1007/s00484-019-01810-1.
- Eitzinger J, Trnka M, Hösch J, Žalud Z, Dubrovský M. 2004. Comparison of CERES, WOFOST and SWAP models in simulating soil water content during growing season under different soil conditions. *Ecological Modelling* 171:223-246 DOI: 10.1016/j.ecolmodel.2003.08.012.
- European commission. 2015. Copernicus: Europe's Eyes on Earth. Luxembourg: Publications Office of the European Union. Available from http://copernicus.eu/sites/default/files/documents/Brochure/Copernicus_brochure_EN_web_Oct2017.pdf (accessed October 2021).
- European commission. 2021. Introduction for MARS Crop Yield Forecasting System (MCYFS). Available at https://marswiki.jrc.ec.europa.eu/agri4castwiki/index.php/Welcome_to_WikiMCYFS (accessed October 2021).

- European Space Agency (ESA). 2011. Sentinel-1 to offer new ways of monitoring crops from space. Available from https://www.esa.int/Applications/Observing_the_Earth/Sentinel-1_to_offer_new_ways_of_monitoring_crops_from_space (accessed October 2021).
- European Space Agency (ESA). 2015. Sentinel-2 User Handbook. European Space Agency. Available from https://sentinel.esa.int/documents/247904/685211/Sentinel-2_User_Handbook (accessed October 2021).
- European Space Agency (ESA). 2019. Sentinels – Space for Copernicus. European Space Agency. Available from <https://esamultimedia.esa.int/multimedia/publications/BR-319/BR319.pdf> (accessed October 2021).
- European Space Agency (ESA). Not dated. Europe's Copernicus programme. Available from https://www.esa.int/Applications/Observing_the_Earth/Copernicus/Europe_s_Copernicus_programme (accessed October 2021).
- European Space Agency (ESA). Not dated - a. Facts and figures (Sentinel-1). European Space Agency. Available from https://www.esa.int/Applications/Observing_the_Earth/Copernicus/Sentinel-1/Facts_and_figures (accessed October 2021).
- European Space Agency (ESA). Not dated - b. Facts and figures (Sentinel-2). European Space Agency. Available from https://www.esa.int/Applications/Observing_the_Earth/Copernicus/Sentinel-2/Facts_and_figures (accessed October 2021).
- Eweys OA, Elwan AA, Borham TI. 2017. Integrating WOFOST and Noah LSM for modeling maize production and soil moisture with sensitivity analysis, in the east of The Netherlands. *Field Crops Research* 210:147-161 DOI: 10.1016/j.fcr.2017.06.004.
- Fan X, Liu Y. 2016. A global study of NDVI difference among moderate-resolution satellite Sensors. *Journal of Photogrammetry and Remote Sensing* 121:177-191 DOI: 10.1016/j.isprsjprs.2016.09.008.
- Fang H, Liang S, Hoogenboom G, Teasdale J, Cavigelli M. 2008. Corn-yield estimation through assimilation of remotely sensed data into the CSM-CERES-

- Maize model. *International Journal of Remote Sensing* 29:3011-3032 DOI: 10.1080/01431160701408386.
- Fang H, Liang S, Hoogenboom G. 2011. Integration of MODIS LAI and vegetation index products with the CSM–CERES–Maize model for corn yield estimation. *International Journal of Remote Sensing* 32:1039-1065 DOI: 10.1080/01431160903505310.
- Fern RR, F EA, Bruno A, Morrison ML. 2018. Suitability of NDVI and OSAVI as estimators of green biomass and coverage in a semi-arid rangeland. *Ecological Indicators* 94:16-21 DOI: 10.1016/j.ecolind.2018.06.029.
- Filippini F. 2019. Sentinel-1 GRD Preprocessing Workflow. Proceedings. 3rd International Electronic Conference on Remote Sensing, 22 May–5 June 2019. Roma. DOI: 10.3390/ECRS-3-06201.
- Fieuzal R, Baup F, Marais-Sicre C. 2013. Monitoring Wheat and Rapeseed by Using Synchronous Optical and Radar Satellite Data—From Temporal Signatures to Crop Parameters Estimation. *Advances in Remote Sensing* 2:162-180 DOI: 10.4236/ars.2013.22020.
- Fontanelli G, Paloscia S, Zribi M, Chahbi A. 2013. Sensitivity analysis of X-band SAR to wheat and barley leaf area index in the Merguellil Basin. *Remote Sensing Letters* 4:1107-1116 DOI: 10.1080/2150704X.2013.842285.
- Foster T, Brozovic N, Butler AP, Neale CMU, Raes D, Steduto P, Fereres E, Hsiao TC. 2017. AquaCrop-OS: An open source version of FAO’s crop water productivity model. *Agricultural Water Management* 181:18-22 DOI: 10.1016/j.agwat.2016.11.015.
- Galaktionov UK, Ashmarina LF, Galaktionova TA. 2009. Wheat yield prediction from winter temperature and precipitation. *Russian Agricultural Sciences* 35:147-149.
- Gao B. 1996. NDWI – A normalized difference water index for remote sensing of vegetation liquid water from space. *Remote Sensing Environment* 58: 257-266 DOI: 10.1016/S0034-4257(96)00067-3.
- Gauthier Y, Bernier M, Fortin JP. 1998. Aspect and incidence angle sensitivity in ERS-1 SAR data. *International Journal of Remote Sensing* 19:2001-2006 DOI: 10.1080/014311698215117.
- Géron A. 2019. *Hands-On Machine Learning with Scikit-Learn, Keras & TensorFlow*. O’Reilly, Canada.

- Gilardelli C, Confalonieri R, Cappelli GA, Bellocchi G. 2018. Sensitivity of WOFOST-based modelling solutions to crop parameters under climate change. *Ecological Modelling* 368:1-14 DOI: 10.1016/j.ecolmodel.2017.11.003.
- Gilardelli C, Stella T, Frasso N, Cappeli G, Bregaglio S, Chiodini ME, Scaglia B, Confalonieri R. 2016. WOFOST-GTC: A new model for the simulation of winter rapeseed production and oil quality. *Field Crops Research* 197:125-132 DOI: 10.1016/j.fcr.2016.07.013.
- Gonenc A, Ozerdem MS, Acar E. 2019. Comparison of NDVI and RVI Vegetation Indices Using Satellite Images. 8th International Conference on Agro-Geoinformatics (Agro-Geoinformatics). Istanbul. DOI: 10.1109/Agro-Geoinformatics.2019.8820225.
- Goodman JW. 1976. Some fundamental properties of speckle. *Journal of the Optical Society of America* 66:1145-1150 DOI: 10.1364/JOSA.66.001145.
- Google Scholar. Not dated. Google Scholar results (search WOFOST and different staple crops). Available from <https://scholar.google.com/> (Accessed December 2021)
- Goward S, Markham B, Dye D. 1991. Normalized difference vegetation index measurements from the advanced very high resolution radiometer. *Remote Sensing of Environment* 35:257-277 DOI: 10.1016/0034-4257(91)90017-Z.
- Griffith J, Martinko EA, Whistler JL, Price K. 2002. Interrelationships Among Landscapes, NDVI, and Stream Water Quality in the US Central Plains. *Ecological Applications* 12:1702-1718 DOI: 10.1890/1051-0761(2002)012[1702:IALNAS]2.0.CO;2.
- Groenendijk P, Boogaard H, Heinen M, Kroes JG, Supit I, de Wit A. 2016. Simulation nitrogen-limited crop growth with SWAP/WOFOST: process descriptions and user manual. Wageningen Environmental Research. DOI: 10.18174/400458.
- Guo WW, Xue H. 2014. Crop Yield Forecasting Using Artificial Neural Networks: A Comparison between Spatial and Temporal Models. *Mathematical Problems in Engineering* 2014:1-7 DOI: 10.1155/2014/857865.
- Gupta RK, Prasad TS, Vijayan D. 2000. Relationship Between LAI and NDVI For IRS LISS and Landsat Tm Bands. *Advanced Space Research* 26:1047-1050. DOI: 10.1016/S0273-1177(99)01115-1.

- Gutman G. 1991. Vegetation indices from AVHRR: An update and future prospects. *Remote Sensing of Environment* 35:121-136 DOI: 10.1016/0034-4257(91)90005-Q.
- Hadria R, Duchemin B, Lahrouni A, Khabba S, Er-raki S, Dedieu G, Chehbouni AG, Oliosio A. 2006. Monitoring of irrigated wheat in a semi-arid climate using crop modelling and remote sensing data: Impact of satellite revisit time frequency. *International Journal of Remote Sensing* 27:1093-1117 DOI: 10.1080/01431160500382980.
- Haldar D, Dave V, Misra A, Bhattacharya B. 2018. Radar Vegetation Index for assessing cotton crop condition using RISAT-1 data. *Geocarto International* 35:364-375 DOI: 10.1080/10106049.2018.1516249.
- Haldar D, Verma A, Kumar S, Chauhan P. 2021. Estimation of mustard and wheat phenology using multi-date Shannon entropy and Radar Vegetation Index from polarimetric Sentinel-1. *Geocarto International*. DOI: 10.1080/10106049.2021.1926554.
- Harfenmeister K, Spengler D, Weltzien C. 2019. Analyzing Temporal and Spatial Characteristics of Crop Parameters Using Sentinel-1 Backscatter Data. *Remote Sensing* 11: (1569) DOI: 10.3390/rs11131569.
- Herrmann I, Pimstein A, Karnieli A, Cohen Y, Alchanatis V, Bonfil DJ. 2011. LAI assessment of wheat and potato crops by VEN μ S and Sentinel-2 bands. *Remote Sensing of Environment* 115:2141-2151 DOI: 10.1016/j.rse.2011.04.018.
- Hengl T, de Jesus JM, Heuvelink GBM, Gonzalez MR, Kilibarda M, Blagotić A, Shangguan W, Wright MN, Geng X, Bauer-Marschallinger B, Guevara MA, Vargas R, MacMillan RA, Batjes NH, Leenaars JGB, Ribeiro E, Wheeler I, Mantel S, Kempen B. 2017. SoilGrids250m: Global gridded soil information based on machine learning. *PLoS ONE* 12: (e0169748) DOI: 10.1371/journal.pone.0169748.
- Hensawang S, Injan S, Varnakovida P, Humpries U. 2021. Predicting Rice Production in Central Thailand Using the WOFOST Model with ENSO Impact. *Mathematical and Computational Applications* 26: (72) DOI: 10.3390/mca26040072.
- Hird JN, McDermid GJ. 2009. Noise Reduction of NDVI Time-Series: An Empirical Comparison of Selected Techniques. *Remote Sensing of Environment* 113:248-258 DOI: 10.1016/j.rse.2008.09.003.

- Hoblen B, Fraser RS. 1984. Red and near-infrared response to off-nadir viewing. *International Journal of Remote Sensing* 5:145-460 DOI: 10.1080/01431168408948795.
- Holtgrave AK, Röder N, Ackermann A, Erasmi S, Kleinschmit B. 2020. Comparing Sentinel-1 and -2 Data and Indices for Agricultural Land Use Monitoring. *Remote Sensing* 12: (2919) DOI: 10.3390/rs12182919.
- Houborg R, Fisher JB, Skidmore AK. 2015. Advances in remote sensing of vegetation function and traits. *International Journal of Applied Earth Observation and Geoinformation* 43:1-6 DOI: 10.3390/rs12182919.
- Houborg R, McCabe MF. 2018. A hybrid training approach for leaf area index estimation via Cubist and random forests machine-learning. *ISPRS Journal of Photogrammetry and Remote Sensing* 135:173-188 DOI: 10.1016/j.isprsjprs.2017.10.004.
- Hu S, Shi L, Huang K, Zha Y, Hu X, Ye H, Yang Q. Improvement of sugarcane crop simulation by SWAP-WOFOST model via data assimilation. *Field Crops Research* 232:49-61 DOI: 10.1016/j.fcr.2018.12.009.
- Huang J, Ma H, Su W, Zhang X, Huang Y, Fan J, Wu W. 2015. Jointly Assimilating MODIS LAI and ET Products into the SWAP Model for Winter Wheat Yield Estimation. *IEEE Journal of Selected Topics in Applied Earth Observations and Remote Sensing* 8:4060-4071 DOI: 10.1109/JSTARS.2015.2403135.
- Huang J, Sedano F, Huang Y, Ma H, Li X, Liang S, Tian L, Zhang X, Fan J, Wu W. 2016 - a. Assimilating a synthetic Kalman filter leaf area index series into the WOFOST model to improve regional winter wheat yield estimation. *Agricultural and Forest Meteorology* 216:188-202 DOI: 10.1016/j.agrformet.2015.10.013.
- Huang J, Tian L, Liang S, Ma H, Becker-Reshef I, Huang Y, Su W, Zhang X, Zhu D, WU W. 2015. Improving winter wheat yield estimation by assimilation of the leaf area index from Landsat TM and MODIS data into the WOFOST model. *Agricultural and Forest Meteorology* 204:106-121 DOI: 10.1016/j.agrformet.2015.02.001.
- Huang Y, Walker JP, Gao Y, Wu X, Monerris A. 2016 - b. Estimation of Vegetation Water Content from the Radar Vegetation Index at L-Band. *IEEE Transactions on Geoscience and Remote Sensing* 54:981-989 DOI: 10.1109/TGRS.2015.2471803.

- Ines AMV, Das NN, Hansen JW, Njoku EG. 2013. Assimilation of remotely sensed soil moisture and vegetation with a crop simulation model for maize yield prediction. *Remote Sensing of Environment* 138:149-164 DOI: 10.1016/j.rse.2013.07.018.
- Inglada J, Vincent A, Arias M, Marais-Sicre C. 2016. Improved Early Crop Type Identification by Joint Use of High Temporal Resolution SAR And Optical Image Time Series. *Remote Sensing* 8: (362) DOI: 10.3390/rs8050362.
- International Journal of Applied Earth Observation and Geoinformation (IJAEOG). 2015. Advances in remote sensing of vegetation function and traits. *International Journal of Applied Earth Observation and Geoinformation* 43:1-6 DOI: 10.1016/j.jag.2015.06.001.
- International Soil Reference and Information Centre (ISRIC). Not dated. SoilGrids — global gridded soil information. Available from <https://www.isric.org/explore/soilgrids> (Accessed November 2021).
- Jiao X, Kovacs JM, Shang J, McNairn H, Walters D, Mab B, Geng X. 2014. Object-oriented crop mapping and monitoring using multi-temporal polarimetric RADARSAT-2 data. *ISPRS Journal of Photogrammetry and Remote Sensing* 96:38-46 DOI: 10.1016/j.isprsjprs.2014.06.014.
- Jiao X, McNairn H, Shang J, Pattey E, Liu Jianguo, Champagne C. 2009. The sensitivity of RADARSAT-2 quad-polarization SAR data to crop LAI. *Proceedings 7454, Remote Sensing and Modeling of Ecosystems for Sustainability VI; SPIE Optical Engineering + Applications*. San Diego. DOI: 10.1117/12.825701.
- Jin X, Kumar L, Li Z, Feng H, Xu X, Yang G, Wang J. 2018. A review of data assimilation of remote sensing and crop models. *European Journal of Agronomy* 92:141-152 DOI: 10.1016/j.eja.2017.11.002.
- Jin X, Yang G, Xu X, Yang H, Feng H, Li Z, Shen J, Zhao Ch, Lan Y. 2015. Combined Multi-Temporal Optical and Radar Parameters for Estimating LAI and Biomass in Winter Wheat Using HJ and RADARSAR-2 Data. *Remote Sensing* 7:13251-13272 DOI: 10.3390/rs71013251.
- Jiang Z, Chen Z, Chen J, Liu J, Ren J, Li Z, Sun L, Li H. 2014. Application of Crop Model Data Assimilation with a Particle Filter for Estimating Regional Winter Wheat Yields. *IEEE Journal of Selected Topics in Applied Earth Observations and Remote Sensing* 7:4422-4431 DOI: 10.1109/JSTARS.2014.2316012.

- Jones JW, Antle JM, Basso B, Boote KJ, Conant RT, Foster I, Godfray HCJ, Herrero M, Howitt RE, Janssen S, Keating BA, Munoz-Carpena R, Porter CH, Rosenzweig C, Wheeler TR. 2016. Brief history of agricultural systems modeling. *Agricultural Systems* 155:240-254 DOI: 10.1016/j.agsy.2016.05.014.
- Jonckheere I, Fleck S, Nackaerts K, Muys B, Coppin P, Weiss M, Baret F. 2004. Review of methods for in situ leaf area index determination Part I. Theories, sensors and hemispherical photography. *Agricultural and Forest Meteorology* 121:19-35 DOI: 10.1016/j.agrformet.2003.08.027.
- Kappas MW, Propastin PA. 2011. Review of Available Products of Leaf Area Index and Their Suitability over the Formerly Soviet Central Asia. *Journal of Sensors* 2012 (1687-725X) DOI: 10.1155/2012/582159.
- Kasampalis DA, Alexandridis TK, Deva Ch, Challinor A, Moshou D, Zalidis G. 2018. Contribution of Remote Sensing on Crop Models: A Review. *Journal of Imaging* 4: (52) DOI: 10.3390/jimaging4040052.
- Katzfuss M, Stroud RJ, Wikle CK. 2016. Understanding the Ensemble Kalman Filter. *The American Statistician* 70:350-357 DOI: 10.1080/00031305.2016.1141709.
- Kersebaum KC, Boote KJ, Jorgenson JS, Nendel C, Bindi M, Frühauf C, Gaiser T, Hoogenboom G, Kollas C, Olesen JE, Rotter RP, Ruget F, Thorburn PJ, Trnka M, Wegehenkel M. 2015. Analysis and classification of data sets for calibration and validation of agro-ecosystem models. *Environmental Modelling & Software* 72:402-417 DOI: 10.1016/j.envsoft.2015.05.009.
- Kim Y, Jackson T, Bindlish R, Hong S, Jung G, Lee K. 2014. Retrieval of Wheat Growth Parameters with Radar Vegetation Indices. *IEEE Geoscience and Remote Sensing Letters* 11:808-812 DOI: 10.1109/LGRS.2013.2279255.
- Kim Y, Jackson T, Bindlish R, Lee H, Hong S. 2012. Radar vegetation index for estimating the vegetation water content of rice and soybean. *IEEE Geoscience and Remote Sensing Letters* 9:564-568 DOI: 10.1109/LGRS.2011.2174772.
- Kim Y, van Zyl J. 2004. Vegetation effects on soil moisture estimation. In *Geoscience and Remote Sensing Symposium. Proceedings of the IGARSS '04 Conference; IEEE International* 2:800-802. Anchorage. DOI: 10.1109/IGARSS.2004.1368525.
- Kim Y, van Zyl J. 2009. A time-series approach to estimate soil moisture using polarimetric radar data. *IEEE Transactions on Geoscience and Remote Sensing* 47:2519-2527 DOI: 10.1109/TGRS.2009.2014944.

- Kim Y, Jackson T, Bindlish R, Hong S, Jung G, Lee K. 2014 – a. Retrieval of Wheat Growth Parameters with Radar Vegetation Indices. *IEEE Geoscience and Remote Sensing Letters* 11:808-812 DOI: 10.1109/LGRS.2013.2279255.
- Kim YH, Oh JH, Kim YI. 2014 - b. Comparative Analysis of the Multispectral Vegetation Indices and the Radar Vegetation Index. *Journal of the Korean Society of Surveying, Geodesy, Photogrammetry and Cartography* 32:607-615 DOI: 10.7848/ksgpc.2014.32.6.607.
- Knox S, Meier P, Yoon J, Harou JJ. 2018. A python framework for multi-agent simulation of networked resource systems. *Environmental Modelling & Software* 103:16-28 DOI: 10.1016/j.envsoft.2018.01.019.
- Koehrsen W. 2018. Hyperparameter Tuning the Random Forest in Python. *Towards Data Science*. Available from <https://towardsdatascience.com/hyperparameter-tuning-the-random-forest-in-python-using-scikit-learn-28d2aa77dd74> (accessed November 2021).
- Koetz B, Belward A, Gascon F, Strobl P, Paganini M, Lemoine G, Schaaf C. 2021. Science and Applications with Sentinel-2. *Remote Sensing of Environment*. Available from <https://www.sciencedirect.com/journal/remote-sensing-of-environment/special-issue/1045CSHL53V> (accessed November 2021).
- Koo J. 2017. NASA – POWER. DSSAT. Available from <https://dssat.net/714/> (accessed October 2021).
- Koppe W, Gnyp M, Hutt C, Yao Y, Miao Y, Chen, X, Bareth G. 2013. Rice monitoring with multitemporal and dual-polarimetric TerraSAR-X data. *International Journal of Applied Earth Observation and Geoinformation* 21:568-576 DOI: 10.1016/j.jag.2012.07.016.
- Kulig B, Skowera B, Klimek-Kopyra A, Kołodziej S, Grygierzec W. 2020. The Use of the WOFOST Model to Simulate Water-Limited Yield of Early Potato Cultivars. *Agronomy* 10: (81) DOI: 10.3390/agronomy10010081.
- Kumar DS, Sitiraju SR, Sharma JR. 2013. Radar Vegetation Index as an Alternative to NDVI for Monitoring of Soyabean and Cotton. *INCA International Congress* 33. Jodhpur.
- Kumari P, Wadood A, Singh RS, Kumar R. 2009. Response of wheat crop to different thermal regimes under the agroclimatic conditions of Jharkhand. *Journal of Agrometeorology* 11: 85-88.

- Kumhálová J, Kumhála F, Kroulík M, Matějková Š. 2011. The impact of topography on soil properties and yield and the effects of weather conditions. *Precision Agriculture* 12:813-830 DOI: 10.1007/s11119-011-9221-x.
- Lancashire PD, Bleiholder H, Van Den Boom T, Langelüddeke P, Stauss R, Weber E, Witzemberger A. 1991. A uniform decimal code for growth stages of crops and weeds. *Annals of Applied Biology* 119:561-601 DOI: 10.1111/j.1744-7348.1991.tb04895.x.
- Lecerf R, Ceglar A, Lopéz-Lozano R, van der Velde M, Baruth B. 2019. Assessing the information in crop model and meteorological indicators to forecast crop yield over Europe. *Agricultural Systems* 168:191-202 DOI: 10.1016/j.agsy.2018.03.002.
- Lee JS, Pottier E. 2009. *Polarimetric SAR Radar Imaging: From Basic to Applications*, CRC Press, Taylor and Francis Group, USA. DOI: 10.1201/9781420054989.
- Li F, Ren J, Wu S, Zhao H, Zhang N. 2021. Comparison of Regional Winter Wheat Mapping Results from Different Similarity Measurement Indicators of NDVI Time Series and Their Optimized Thresholds. *Remote Sensing* 13: (1162) DOI: 10.3390/rs13061162.
- Li H, Liu Q, Chen Z, Huang Ch. 2018. Retrieval of Winter Wheat Leaf Area Index from Chinese GF-1 Satellite Data Using the PROSAIL Model. *Sensors* 18: (1120) DOI: 10.3390/s18041120.
- Li R, Cun-Jun C, Ying-ying D, Feng L, Ji-hua W, Xiao-dong Y, Yu-chun P. 2011. Assimilation of Remote Sensing and Crop Model for LAI Estimation Based on Ensemble Kalman Filter. *Agricultural Sciences in China* 10:1595-1602 DOI: 10.1016/S1671-2927(11)60156-9.
- Li Y, Li M, Li CH, Liu Z. 2020. Forest aboveground biomass estimation using Landsat 8 and Sentinel-1A data with machine learning algorithms. *Scientific Reports* 10: (9952) DOI: 10.1038/s41598-020-67024-3.
- Liu F, Liu X, Zhao L, Ding Ch, Jiang J, Wu L. 2015. The Dynamic Assessment Model for Monitoring Cadmium Stress Levels in Rice Based on the Assimilation of Remote Sensing and the WOFOST Model. *IEEE Journal of Selected Topics in Applied Earth Observations and Remote Sensing* 8:1330-1338 DOI: 10.1109/JSTARS.2014.2371058.
- Liu J, Huang J, Tian L, Ma H, Su W, Wu W, Ramsankaran R, Zhang X, Zhu D. 2014. Regional winter wheat yield prediction by integrating MODIS LAI into the

- WOFOST model with sequential assimilation technique. *Journal of Food, Agriculture & Environment* 12:180-187 DOI: 10.1234/4.2014.4167.
- Lobell DB, Burke MB. 2010. On the use of statistical models to predict crop yield responses to climate change. *Agricultural and Forest Meteorology* 150:443-1452. DOI: 10.1016/j.agrformet.2010.07.008.
- Ma G, Huang J, Wu W, Fan J, Zou J, Wu S. 2013a. Assimilation of MODIS-LAI into the WOFOST model for forecasting regional winter wheat yield. *Mathematical and Computer Modelling* 58:634-643. DOI: 10.1016/j.mcm.2011.10.038.
- Ma H, Huang J, Zhu D, Liu J, Su W, Zhang Ch, Fan J. 2013b. Estimating regional winter wheat yield by assimilation of time series of HJ-1 CCD NDVI into WOFOST-ACRM model with Ensemble Kalman Filter. *Mathematical and Computer Modelling* 58:759-770 DOI: 10.1016/j.mcm.2012.12.028.
- Macelloni G, Paloscia S, Pamploni P, Marliani F, Gai M. 2001. The relationship between the backscattering coefficient and the biomass of narrow and broad leaf crops. *IEEE Transactions on Geoscience and Remote Sensing* 39:873-884 DOI: 10.1109/36.917914.
- Malenovský Z, Rott H, Cihlar J, Schaepman ME, García-Santos G, Fernandes R, Berger M. 2012. Sentinels for science: Potential of Sentinel-1, -2, and -3 missions for scientific observations of ocean, cryosphere, and land. *Remote Sensing Environment* 120:91-101 DOI: 10.1016/j.rse.2011.09.026.
- Mandal D, Bhattacharya A, Kumar V, Ratha D, Dey S, McNairn H, Frery AC, Rao YS. 2019. A Novel Radar Vegetation Index for Compact Polarimetric SAR Data. *IGARSS 2019 - 2019 IEEE International Geoscience and Remote Sensing Symposium*. Yokohama. DOI: 10.1109/IGARSS.2019.8898022.
- Mandal D, Kumar V, Ratha D, Deya S, Bhattacharya A, Lopez-Sanchez JM, McNairn H, Raoa SY. 2020 - a. Dual polarimetric radar vegetation index for crop growth monitoring using sentinel-1 SAR data. *Remote Sensing of Environment* 247: (111954) DOI: 10.1016/j.rse.2020.111954.
- Mandal D, Kumar V, Ratha D, Lopez-Sanchez JM, Bhattacharya A, McNairn H, Rao YS, Ramana KV. 2020 - b. Assessment of rice growth conditions in a semi-arid region of India using the Generalized Radar Vegetation Index derived from RADARSAT-2 polarimetric SAR data. *Remote Sensing of Environment* 237: (111561) DOI: 10.1016/j.rse.2019.111561.

- Mandal D, Ratha D, Bhattacharya A, Kumar V, McNairn H, Rao SY, Frey AC. 2020 - c. A Radar Vegetation Index for Crop Monitoring Using Compact Polarimetric SAR Data. *IEEE Transactions on Geoscience and Remote Sensing* 58:6321-6335 DOI: 10.1109/TGRS.2020.2976661.
- Manjunath KR, Potdar MB, Purohit NL. 2010. Large area operational wheat yield model development and validation based on spectral and meteorological data. *International Journal of Remote Sensing* 23: 3023-3038 DOI: 10.1080/01431160110104692.
- Manzane S, Pôças I, Cunha M. 2018. Retrieval of Maize Leaf Area Index Using Hyperspectral and Multispectral Data. *Remote Sensing* 10: 1942. <https://doi.org/10.3390/rs10121942>
- Maruyama A, Kurose Y, Ohba K. 2010. Modeling of phenological development in winter wheat to estimate the timing of heading and maturity based on daily mean air temperature and photoperiod. *Journal of Agricultural Meteorology* 66:41-50 DOI: 10.2480/agrmet.66.1.7.
- McKinney W, & others. 2010. Data structures for statistical computing in python. In *Proceedings of the 9th Python in Science Conference* 445:51-56 DOI: 10.25080/Majora-92bf1922-00a
- McNairn H, Brisco B. 2004. The application of C-band polarimetric SAR for agriculture: a review. *Canadian Journal of Remote Sensing* 30:525-542 DOI: 10.5589/m03-069.
- McNairn H, Jiao X, Pacheco A, Sinha A, Tan W, Li Y. 2018. Estimating canola phenology using synthetic aperture radar. *Remote Sensing of Environment* 219:196-205 DOI: 10.1016/j.rse.2018.10.012.
- Mirschel W, Schultz A, Wenkel KO. 2004. Crop growth modeling on different spatial scales-A wide spectrum of approaches. *Archives of Agronomy and Soil Science* 50:329-343 DOI: 10.1080/03650340310001634353.
- Mishra SK, Shekh AM, Pandey V, Yadav SB, Patel HR. 2015. Sensitivity analysis of four wheat cultivars to varying photoperiod and temperature at different phenological stages using WOFOST model. *Journal of Agrometeorology* 17: 74-79.
- Mueller-Wilm U. 2020. Sen2Cor Configuration and User Manual. European Space Agency. Available from <http://step.esa.int/thirdparties/sen2cor/2.9.0/docs/S2-PDGS-MPC-L2A-SUM-V2.9.0.pdf> (accessed November 2021).

- Musa ZN, Popescu I, Mynett A. 2015. A review of applications of satellite SAR, optical, altimetry and DEM data for surface water modelling, mapping and parameter estimation. *Hydrology and Earth System Sciences* 19:3755-3769 DOI: 10.5194/hess-19-3755-2015.
- NASA - Earthdata. 2020. What is Synthetic Aperture Radar? NASA – Earthdata. Available from <https://earthdata.nasa.gov/learn/backgrounders/what-is-sar> (accessed November 2021).
- Nagy A, Fehér J, Tamas J. 2018. Wheat and maize yield forecasting for the Tisza river catchment using MODIS NDVI time series and reported crop statistics. *Computers and Electronics in Agriculture* 151:41-49 DOI: 10.1016/j.compag.2018.05.035.
- Nasrallah A, Baghdadi N, Hajj ME, Darwish T, H Belhouchette, Faour G, Darwich S, Mhawej M. 2019. Sentinel-1 data for winter wheat phenology monitoring and mapping. *Remote Sensing* 11: (2228) DOI: 10.3390/rs11192228.
- Nearing GS, Crow WT, Thorp KR, Moran MS, Reichle RH, Gupta HV. 2012. Assimilating remote sensing observations of leaf area index and soil moisture for wheat yield estimates: An observing system simulation experiment. *Water Resources Research* 48 DOI: 10.1029/2011WR011420.
- Ojeda JJ, Volenec JJ, Brouder SM, Caviglia OP, Agnusdei MG. 2017. Evaluation of Agricultural Production Systems Simulator as Yield Predictor of *Panicum virgatum* and *Miscanthus x giganteus* in Several US Environments. *GCB Bioenergy* 9:796-816 DOI: 10.1111/gcbb.12384.
- Omer G, Mutanga O, Abdel-Rahman EM, Adam E. 2016. Empirical Prediction of Leaf Area Index (LAI) of Endangered Tree Species in Intact and Fragmented Indigenous Forests Ecosystems Using WorldView-2 Data and Two Robust Machine Learning Algorithms. *Remote Sensing* 8: (324) DOI: 10.3390/rs8040324.
- Palosuo T, Kersebaum KC, Angulo C, Hlavinka P, Moriondo M, Olesen J, Patil HR, Ruget F, Rumbaurc, Takáč J, Trnka M, Bindii M, Çaldağ B, Ewert F, Ferrise R, Mirschel W, Şaylan L, Šiška B, Rötter R. 2011. Simulation of winter wheat yield and its variability in different climates of Europe: A comparison of eight crop growth models. *European Journal of Agronomy* 35:103-114 DOI: 10.1016/j.eja.2011.05.001.

- Pan H, Chen Zhongxin, de Witt A, Ren J. 2019. Joint Assimilation of Leaf Area Index and Soil Moisture from Sentinel-1 and Sentinel-2 Data into the WOFOST Model for Winter Wheat Yield Estimation. *Sensors* 19: (3161) DOI: 10.3390/s19143161.
- Pan Z, Huang J-F, Wei CH, Zhang HK. 2017. Remote Sensing of Agricultural Disasters Monitoring: Recent Advances. *International Journal of Remote Sensing & Geoscience* 6.
- Pasqualotto N, Delegido J, Wittenberghe SV, Rinaldi M, Moreno J. 2019. Multi-Crop Green LAI Estimation with a New Simple Sentinel-2 LAI Index (SeLI). *Sensors* 19: (904) DOI: 10.3390/s19040904.
- Pedregosa F, Varoquaux G, Gramfort A, Michel V, Thirion B, Grisel O, Blondel M, Prettenhofer P, Weiss R, Dubourg V, Vanderplas J, and Passos A, Cournapeau D, Brucher M, Perrot M, Duchesnay E. 2011. Scikit-learn: Machine Learning in Python. *Journal of Machine Learning Research* 12: 2825-2830.
- Periasamy S. 2018. Significance of dual polarimetric synthetic aperture radar in biomass retrieval: An attempt on Sentinel-1. *Remote Sensing of Environment* 217:537-549 DOI: 10.1016/j.rse.2018.09.003.
- Pohanková E. 2016. Modelování růstu a vývoje ječmene jarního [Dissertation thesis]. Mendel University in Brno, Brno.
- Potin P, Rosich B, Miranda N, Grimont P. 2016. Sentinel-1 Mission Status. *Procedia Computer Science* 100:1297-1304 DOI: 10.1016/j.procs.2016.09.245.
- POWER Project Team. Not dated. POWER Data Methodology. NASA POWER. Available from <https://power.larc.nasa.gov/docs/methodology/> (accessed October 2021).
- Pozníková G. 2016. Comparison of evapotranspiration measurement methods in agricultural landscape [Dissertation thesis]. Mendel University in Brno, Brno.
- Pushpalatha R, Kutty G, Gangadharan B. 2021. Sensitivity analysis of WOFOST for yield simulation of cassava over the major growing areas of India. *Journal of Agrometeorology* 23:375-380 DOI: 10.54386/jam.v23i4.140.
- Probst P, Wright MN, Boulesteix AL. 2018. Hyperparameters and tuning strategies for random forest. *Wiley Interdisciplinary Reviews: Data Mining and Knowledge Discovery* 9: (e1301) DOI: 10.1002/widm.1301.
- Qader SH, Dash J, Atkinson PM. 2018. Forecasting wheat and barley crop production in arid and semi-arid regions using remotely sensed primary productivity and crop

- phenology: A case study in Iraq. *Science of the Total Environment* 613-614: 250-262 DOI: 10.1016/j.scitotenv.2017.09.057.
- Qian B, De Jong R, Warren R, Chipanshi A, Hill H. 2009. Statistical spring wheat yield forecasting for the Canadian prairie provinces. *Agricultural and Forest Meteorology* 149:1022-1031 DOI: 10.1016/j.agrformet.2008.12.006.
- Raja R, Nayak AK, Panda BB. 2014. Monitoring of meteorological drought and its impact on rice (*Oryza sativa* L.) productivity in Odisha using Standardized Precipitation Index. *Archives of Agronomy and Soil Science* 60:1701-1715. DOI: 10.1080/03650340.2014.912033.
- Reinds GJ, de Koning GHJ, Bulens JD. 1992. Crop production potential of rural areas within the European Communities 111: Soils, Climate and Administrative Regions. Netherlands Scientific Council for Government Policy.
- Renton M, Hanan J, Burrage K. 2005. Using the canonical modelling approach to simplify the simulation of function in functional-structural plant models. *New Phytologist* 166:845-857 DOI: 10.1111/j.1469-8137.2005.01330.x.
- Rodrigues GC, Braga RP. 2021. Evaluation of NASA POWER Reanalysis Products to Estimate Daily Weather Variables in a Hot Summer Mediterranean Climate. *Agronomy* 11: (1207) DOI: 10.3390/agronomy11061207.
- Robertson LD, Davidson A, McNairn H, Hosseini M, Mitchell S, de Abelleira D, Verón S, Cosh MH. 2020. Synthetic Aperture Radar (SAR) image processing for operational space-based agriculture mapping. *International Journal of Remote Sensing* 41:7112-7144 DOI: 10.1080/01431161.2020.1754494.
- Rouse J, Haas R, Schell JA, Deering D. 1974. Monitoring vegetation systems in the Great Plains with ERTS. In *Proceedings Third ERTS-1 Symposium*, NASA Goddard, NASA SP-351: 309-317.
- Rötter RP, Palosuo T, Kersebaum KC, Angulo C, Bindi M, Ewert F, Ferrise R, Hlavinka P, Moriondo M, Nendel C, Olesen JE, Patil RH, Ruget F, Takáč J, Trnka M. 2012. Simulation of spring barley yield in different climatic zones of Northern and Central Europe: A comparison of nine crop models. *Field Crops Research* 133:23-36 DOI: 10.1016/j.fcr.2012.03.016.
- Sánchez N, Lopez-Sanchez JM, Arias-Pérez B, Valcarce-Diñeiro R, Martínez-Fernández JM, Calvo-Heras J, Camps A, González-Zamora A, Vicente-Guijalba F. 2016. New microwave-based missions applications for rainfed crops

- characterization. *The International Archives of the Photogrammetry, Remote Sensing and Spatial Information Sciences* XLI-B8:101-107 DOI: 10.5194/isprs-archives-XLI-B1-101-2016.
- Savitzky A, Golay MJE. 1964. Smoothing and Differentiation of Data by Simplified Least Squares Procedures. *Analytical Chemistry* 36: 1627-1639. DOI: 10.1021/ac60214a047.
- Sayyahi H, Egdernezhad A, Ebrahimipak N. 2020. Evaluation of AquaCrop and WOFOST for Simulation of Sugar Beet Yield and Water Productivity under Different Irrigation Intervals and Fertilizer Stress. *Iranian Journal of Soil and Water Research* 51:2593-2605 DOI: 10.22059/ijswr.2020.300418.668568.
- Seabold S, Perktold J. 2010. statsmodels: Econometric and statistical modeling with python. In 9th Python in Science Conference.
- Selvaraj S, Haldar Dipanwita, Srivastava HS. 2021. Condition assessment of pearl millet/ bajra crop in different vigour zones using Radar Vegetation Index. *Spatial Information Research* 29:631-643 DOI: 10.1007/s41324-021-00380-y.
- Shuai X, Zhixin Q, Xia L, Gar-On Yeh A. 2019. Investigation of the effect of the incidence angle on land cover classification using fully polarimetric SAR images. *International Journal of Remote Sensing* 40:1576-1593 DOI: 10.1080/01431161.2018.1528021.
- Sibanda M, Gumende N, Mutanga O. 2021. Estimating leaf area index of the Yellowwood tree (*Podocarpus* spp.) in an indigenous Southern African Forest, using Sentinel 2 Multispectral Instrument data and the Random Forest regression ensemble. *Geocarto International*. DOI: 10.1080/10106049.2021.1959654.
- Silvestro PC, Pignatii S, Pascucci S, Yang H, Li Z, Yang G, Huang W, Casa R. 2017. Estimating Wheat Yield in China at the Field and District Scale from Assimilation of Satellite Data into the Aquacrop and Simple Algorithm for Yield (SAFY) Models. *Remote sensing* 9: (509) DOI: 10.3390/rs9050509.
- Soudani K, Delpierre N, Berveiller D, Hmimina G, Vincent G, Morfin A, Dufrêne É. 2021. Potential of C-band Synthetic Aperture Radar Sentinel-1 time-series for the monitoring of phenological cycles in a deciduous forest. *International Journal of Applied Earth Observation and Geoinformation* 104: (102505) DOI: 10.1016/j.jag.2021.102505.

- Sparks AH. 2018. nasapower: A NASA POWER Global Meteorology, Surface Solar Energy and Climatology Data Client for R. *Journal of Open Source Software* 3: (1035) DOI: 10.21105/joss.01035.
- Specka X, Nendel C, Wieland R. 2015. Analysing the parameter sensitivity of the agro-ecosystem model MONICA for different crops. *European Journal of Agronomy* 71:73-87 DOI: 10.1016/j.eja.2015.08.004.
- Srivastava PK, O'Neill P, Cosh M, Lang R, Joseph A. 2015. Evaluation of radar vegetation indices for vegetation water content estimation using data from a ground-based SMAP simulator. *IEEE International Geoscience and Remote Sensing Symposium (IGARSS)*. Milan. DOI: 10.1109/IGARSS.2015.7326012.
- Stankevich SA, Kozlova AA, Piestova IO, Lubskyi MS. 2017. Leaf area index estimation of forest using sentinel-1 C-band SAR data. *IEEE Microwaves, Radar and Remote Sensing Symposium (MRRS)*. Kiev, Ukraine. DOI: 10.1109/MRRS.2017.8075075.
- STEP - Science toolbox exploitation platform. Not dated. SNAP - Sentinel Application Platform. European Space Agency. Available from <http://step.esa.int/main/toolboxes/snap/> (accessed October 2021).
- Supit I, Hoojer AA, van Diepen CA. 1994. System description of the Wofost 6.0 crop simulation model implemented in CGMS. Volume 1: Theory and Algorithms. Office for the Official Publications of the European Communities. Accessed from https://www.researchgate.net/publication/282287246_System_description_of_the_Wofost_60_crop_simulation_model_implemented_in_CGMS_Volume_1_Theory_and_Algorithms (accessed November 2021).
- Szigarski C, Jagdhuber T, Baur M, Thiel C, Parrens M, Wigneron JP, Piles M, Entekhabi D. 2018. Analysis of the Radar Vegetation Index and Potential Improvements. *Remote Sensing* 10: 1776.
- Tao L, Li J, Jiang J, Chen X. 2016. Leaf Area Index Inversion of Winter Wheat Using Modified Water-Cloud Model. *Geoscience and Remote Sensing Letters*: 13.
- Tillack A, Clasen A, Kleinschmit B, Förster M. 2014. Estimation of the seasonal leaf area index in an alluvial forest using high-resolution satellite-based vegetation indices. *Remote Sensing of Environment* 141: 52 – 63. <https://doi.org/10.1016/j.rse.2013.10.018>

- Tripathy DS, Prusty BR. 2021. Forecasting of renewable generation for applications in smart grid power systems. Pages 265-298 in *Advances in Smart Grid Power System 265-298. Network, Control and Security*. DOI: 10.1016/B978-0-12-824337-4.00010-2.
- Tripathi MA, Pohanková E, Fischer M, Orság M, Trnka M, Klem K, Marek MV. 2018. The Evaluation of Radiation Use Efficiency and Leaf Area Index Development for the Estimation of Biomass Accumulation in Short Rotation Poplar and Annual Field Crops. *Forests* 9: (168) DOI: 10.3390/f9040168.
- Tripathi MA, Pohanková E, Trnka M. 2017. Comparison of leaf area index dynamics and radiation use efficiency of C3 crops in the Czech Republic. conference: Quo vaditis agriculture, forestry and society under global change? Brno, Czech Republic.
- Trudel M, Charbonneau F. 2012. Using RADARSAT-2 polarimetric and ENVISAT-ASAR dual-polarization data for estimating soil moisture over agricultural fields. *Canadian Journal of Remote Sensing* 38: 514-527. <http://dx.doi.org/10.5589/m12-043>
- Tupin F, Inglada J, Nicolas J-M. 2014. *Remote Sensing Imagery*. John Wiley & Sons, Hoboken, USA. DOI: 10.1002/9781118899106.
- van der Goot E, Supit I, Boogaard HL, van Diepen CA, Micale F, Orlandi S, Otten H, Geuze M, Schulze D. 2013. *Methodology of The Mars Crop Yield Forecasting System Vol.1: Meteorological Data Collection, Processing and Analysis*. Available from https://www.researchgate.net/publication/40795412_Methodology_of_the_MARS_crop_yield_forecasting_system_Vol_4_statistical_data_collection_processing_and_analysis (accessed October 2021).
- Van der Velde M, Baruth B, Bussay A, Ceglar A, Condado SG, Karetos S, Lecerf R, Lopez-Lozano R, Maiorano A, Nisini L, Seguini L, van den Berg M. 2018. n-season performance of European Union wheat forecasts during extreme impacts. *Scientific Reports* 8: (15420) DOI: 10.1038/s41598-018-33688-1.
- Van der Velde M, Nisini L. 2019. Performance of the MARS-crop yield forecasting system for the European Union: Assessing accuracy, in-season, and year-to-year improvements from 1993 to 2015. *Agricultural Systems* 168:203-212 DOI: 10.1016/j.agsy.2018.06.009.

- van Diepen CA, Boogaard HL, Supit I, Lazar C, Orlandi S, van der Goot E, Schapendonk A. 2004. Methodology of the MARS crop yield forecasting system. Vol. 2 agrometeorological data collection, processing and analysis. Available from: https://www.researchgate.net/publication/40795411_Methodology_of_the_MARS_crop_yield_forecasting_system_Vol_2_agrometeorological_data_collection_processing_and_analysis (accessed October 2021).
- van Diepen CA, Wolf J, van Keulen H, Rappoldt C. 1989. WOFOST: a simulation model of crop production. *Soil Use and Management* 5:16-24 DOI: 10.1111/j.1475-2743.1989.tb00755.x.
- van Ittersum MK, Rabbinge R. 1997. Concepts in production ecology for analysis and quantification of agricultural input-output combinations. *Field Crops Research* 52:197-208 DOI: 10.1016/S0378-4290(97)00037-3.
- van Kraalingen DWG, Stol W, Uithol PWJ, Verbeek MGM. 1997. User manual of CABO/TPE Weather System. Department of Theoretical Production Ecology, Wageningen Agricultural University. Available from <https://edepot.wur.nl/43010> (accessed October 2021).
- Vazquez-Cruz MA, Torres-Pacheco I, Miranda-Lopez R, Cornejo-Perez O, Osornio-Ríos AR, Romero-Troncoso RDJ, Guevara-Gonzales RG. 2010. Potential of mathematical modeling in fruit quality. *African Journal of Biotechnology* 9:260-267.
- Virtanen P, Gommers R, Oliphant TE, Haberland M, Reddy T, Cournapeau D, Burovski E, Peterson P, Weckesser W, Bright W, Walt SJ, Brett M, Wilson J, Millman KJ, Mayorov N, Nelson ARJ, Jones E, Kern R, Larson E, Carey CJ, Polat I, Feng Y, Moore EW, VanderPlas J, Laxalde D, Perktold J, Cimrman R, Henriksen I, Quintero EA, Harris CHR, Archibald AM, Ribeiro AH, Pedregosa F, Mulbregt P, SciPy 1.0 Contributors. 2020. SciPy 1.0: Fundamental Algorithms for Scientific Computing in Python. *Nature Methods* 17:261-272 DOI: 10.1038/s41592-019-0686-2.
- Vreugdenhil M, Wagner W, Bauer-Marschallinger B, Pfeil I, Teubner I, Rüdiger Ch, Strauss P. 2018. Sensitivity of Sentinel-1 Backscatter to Vegetation Dynamics: An Austrian Case Study. *Remote Sensing* 10: (1396) DOI: 10.3390/rs10091396.
- Wageningen Environmental Research. Not dated. Principles of WOFOST. Wageningen University & Research. Available from <https://www.wur.nl/en/Research-Results/Research-Institutes/Environmental-Research/Facilities-Tools/Software->

- models-and-databases/WOFOST/Principles-of-WOFOST.htm (accessed October 2021).
- Wang H, Magagi R, Goïta K, Trudel M, McNairn H, Powers J. Crop phenology retrieval via polarimetric SAR decomposition and Random Forest algorithm. *Remote Sensing of Environment* 231: (111234) DOI: 10.1016/j.rse.2019.111234.
- Wang J, Li X, Lu L, Fang F. 2013. Parameter sensitivity analysis of crop growth models based on the extended Fourier Amplitude Sensitivity Test method. *Environmental Modelling & Software* 48:171-182 DOI: 10.1016/j.envsoft.2013.06.007.
- Wang J, Xiao X, Bajgain R, Starks P, Steiner J, Doughty RB, Chang Q. 2019. Estimating leaf area index and aboveground biomass of grazing pastures using Sentinel-1, Sentinel-2 and Landsat images. *ISPRS Journal of Photogrammetry and Remote Sensing* 154:189-201 DOI: 10.1016/j.isprsjprs.2019.06.007.
- Wang L, Huang J, Gao P, Wu H. 2017. Estimating winter wheat yield by assimilation of MODIS LAI into WOFOST model with Ensemble Kalman Filter. 6th International Conference on Agro-Geoinformatics. Fairfax. DOI: 10.1109/Agro-Geoinformatics.2017.8047023
- Wang L, Zhou X, Zhu X, Dong Z, Guo W. 2016. Estimation of biomass in wheat using random forest regression algorithm and remote sensing data. *The Crop Journal* 4:212-219 DOI: 10.1016/j.cj.2016.01.008.
- Wang N, Reidsma P, Pronk AA, de Wit AJW, van Ittersmus MK. 2018. The scope for increasing potato production in China. *European Journal of Agronomy* 101:20-29 DOI: 10.1016/j.eja.2018.07.002.
- Wart J, Grassini P, Cassman KG. 2013. Impact of derived global weather data on simulated crop yields. *Global Change Biology* 19:3822-3834 DOI: 10.1111/gcb.12302.
- Wart J, Grassiny P, Yang H, Claessens L, Jarvis A, Cassman K. 2015. Creating long-term weather data from thin air for crop simulation modelling. *Agricultural and Forest Meteorology*, 209-210:49-58 DOI: 10.1016/j.agrformet.2015.02.020.
- Weiss M, Baret F. 2016. S2ToolBox Level 2 products: LAI, FAPAR, FCOVER. European Space Agency. Available from https://step.esa.int/docs/extra/ATBD_S2ToolBox_L2B_V1.1.pdf (accessed October 2021).

- Weiss M, Baret F, Smith GJ, Jonckheere I, Coppin P. 2004. Review of methods for in situ leaf area index (LAI) determination Part II. Estimation of LAI, errors and sampling. *Agricultural and Forest Meteorology* 121:37-53 DOI: 10.1016/j.agrformet.2003.08.001.
- Wenjiao S, Fulu T, Zhao Z. 2013. A review on statistical models for identifying climate contributions to crop yields. *Journal of Geographical Sciences* 23:567-576 DOI: 10.1007/s11442-013-1029-3.
- White JW, Hoogenboom G, Stackhouse PW, Hoell JM. 2008. Evaluation of NASA satellite- and assimilation model-derived long-term daily temperature data over the continental US. *Agricultural and Forest Meteorology* 148:1574-1584. DOI: 10.1016/j.agrformet.2008.05.017.
- Wimmerová M, Pohanková E, Kersebaum KC, Trnka M, Žalud Z, Hlavinka P. 2016. Assessing the impact of drought stress on winter wheat canopy by Hermes crop growth model. Conference: MendelNet 2016. Brno, the Czech Republic.
- Wohlstadter M, Shoaib L, Posey J, Welsh J, Fishman J. 2016. A Python toolkit for visualizing greenhouse gas emissions at sub-county scales. *Environmental Modelling & Software* 83:237-244 DOI: 10.1016/j.envsoft.2016.05.016.
- Wolf J, de Wit A. 2010. Calibration of WOFOST crop growth simulation model for use within CGMS. *Alterra, Wageningen University & Research Centre* 1-38.
- Wu S, Huang J, Liu X, Fan J, Ma G, Zou J. 2011. Assimilating MODIS-LAI into Crop Growth Model with EnKF to Predict Regional Crop Yield. *International Conference on Computer and Computing Technologies in Agriculture* 5: 410-418. Beijing, China. Available from <https://dl.ifip.org/db/conf/ifip12/ccta2011-3/WuHLMZ11.pdf> (accessed October 2021).
- Wu Y, Xu W, Huang H, Huang J, Yin F, Ma H, Zhuo W, Gao X, Shen Q, Wang X. 2020. Winter Wheat Yield Estimation at the Field Scale by Assimilating Sentinel-2 LAI into Crop Growth Model. *IGARSS 2020 - 2020 IEEE International Geoscience and Remote Sensing Symposium. Waikoloa.* DOI: 10.1109/IGARSS39084.2020.9323941.
- Xue J, Su B. 2017. Significant Remote Sensing Vegetation Indices: A Review of Developments and Applications. *Journal of Sensors* 2017: (1353691) DOI: 10.1155/2017/1353691.

- Yan Y. 2015. Application of SWAP-WOFOST to evaluate the influence of water and oxygen stress on potato yield in a Dutch farm [MSc. Thesis]. Wageningen University, Wageningen. Available from <https://edepot.wur.nl/410528> (accessed October 2021).
- Yadav VP, Prasad R, Bala R, Srivastava PK, Vanama VSK. 2021. Appraisal of dual polarimetric radar vegetation index in first order microwave scattering algorithm using sentinel – 1A (C - band) and ALOS - 2 (L - band) SAR data. Geocarto International. DOI: 10.1080/10106049.2021.1933209.
- Yamaguchi T, Tanaka Y, Imachi Y, Yamashita M, Katsura K. Feasibility of Combining Deep Learning and RGB Images Obtained by Unmanned Aerial Vehicle for Leaf Area Index Estimation in Rice. *Remote Sensing* 13: (84) DOI: 10.3390/rs13010084.
- Yesilkoy S, Şaylan L, Akatas N, Bakanogulları F, B Çaldağ, Aslan T. 2015. Variation of albedo during the growing period of different winter wheat cultivars. Conference: 2nd International Conference/Symposium for Agriculture and Food. Ohrid.
- Zandler H, Senftl T, Vanselow KA. 2020. Reanalysis datasets outperform other gridded climate products in vegetation change analysis in peripheral conservation areas of Central Asia. *Scientific Reports* 10: (22446) DOI: 10.1038/s41598-020-79480-y
- Zhao Y, Chen S, Shen S. 2013. Assimilating remote sensing information with crop model using Ensemble Kalman Filter for improving LAI monitoring and yield estimation. *Ecological Modelling* 270:30-42 DOI: 10.1016/j.ecolmodel.2013.08.016.
- Zhang X, He B, Quan X. 2016. Assimilation of 30m resolution LAI into crop growth model for improving LAI estimation in plateau grassland. 2016 IEEE International Geoscience and Remote Sensing Symposium (IGARSS). Beijing, China. DOI: 10.1109/IGARSS.2016.7729329.
- Zhang X, Zhang M, Zheng Y, Wu B. 2016. Crop Mapping Using PROBA-V Time Series Data at the Yucheng and Hongxing Farm in China. *Remote sensing* 8: (915) DOI: 10.3390/rs8110915.
- Zhang Z, Moore JC. 2015. Data Assimilation. Pages 291-311 in *Mathematical and Physical Fundamentals of Climate Change*. Elsevier. DOI: 10.1016/B978-0-12-800066-3.00009-7.
- Zheng G, Moskal LM. 2009. Retrieving Leaf Area Index (LAI) Using Remote Sensing: Theories, Methods and Sensors. *Sensors* 9:2719-2745 DOI: 10.3390/s90402719.

- Zhu J, Zeng W, Ma T, Lei G, Zha Y, Fang Y, Wu J, Huang J. 2018. Testing and Improving the WOFOST Model for Sunflower Simulation on Saline Soils of Inner Mongolia, China. *Agronomy* 8:(172) DOI: 10.3390/agronomy8090172.
- Zhu Y, Feng Z, Lu J, Liu J. 2020. Estimation of Forest Biomass in Beijing (China) Using Multisource Remote Sensing and Forest Inventory Data. *Forests* 11: (163) DOI: 10.3390/f11020163.
- Zhuo W, Huang J, Li L, Huang R, Gao X, Zhang X, Zhu D. 2018. Assimilating SAR and Optical Remote Sensing Data into WOFOST Model for Improving Winter Wheat Yield Estimation. 2018 7th International Conference on Agro-geoinformatics (Agro-geoinformatics). Hangzhou, China. DOI: 10.1109/Agro-Geoinformatics.2018.8476074
- Zhuo Wen, Huang J, Li L, Zhang X, Ma H, Gao X, Huang H, Xu B, Xiao X. 2019. Assimilating Soil Moisture Retrieved from Sentinel-1 and Sentinel-2 Data into WOFOST Model to Improve Winter Wheat Yield Estimation. *Remote Sensing* 11: (1618) DOI: <https://doi.org/10.3390/rs11131618>.

10. Author Bibliography

Tůma L, Kumhálová J, Kumhála F, Krepl V. 2021. The noise-reduction potential of Radar Vegetation Index for crop management in the Czech Republic. Precision Agriculture. DOI: 10.1007/s11119-021-09844-5.

11. Annex

List of Figures:

Annex - Fig. I. Phenological metrics derived from a smoothed curve (dark thick curve) of a timeseries of photosynthetically active vegetation (PV) cover fractions (irregular gray line). (Source: Chang et al. 2013)..... II

Annex - Fig. II. Vegetation phenology curve and metrics derived from enhanced AVHRR imagery. (Source: Griffith et al. 2002) II

Annex - Fig. III. Graph of normalized difference vegetation index (NDVI) and BBCH scale dependency in the case of winter wheat. (Source: Domínguez et al. 2015)..... III

Annex - Fig. IV. Leaf Area Index measurements of winter wheat. (Source: Yesilkoy et al. 2015)III

Annex - Fig. V. Five initial variables and parameters for Ensemble model treated as Gaussian random variables with a mean equal to a calibrated value IV

Annex - Fig. VI. Graph of normalized difference vegetation index (NDVI) and BBCH scale dependency in the case of winter wheat. V

List of Tables:

Annex - Table I. Leaf Area Index results of wheat fields – descriptive statistics. VI

Annex - Table II. Unfiltered RVI products - 2016 VII

Annex - Table III. Filtered RVI products - 2016..... VIII

Annex - Table IV. Unfiltered RVI products - 2017 IX

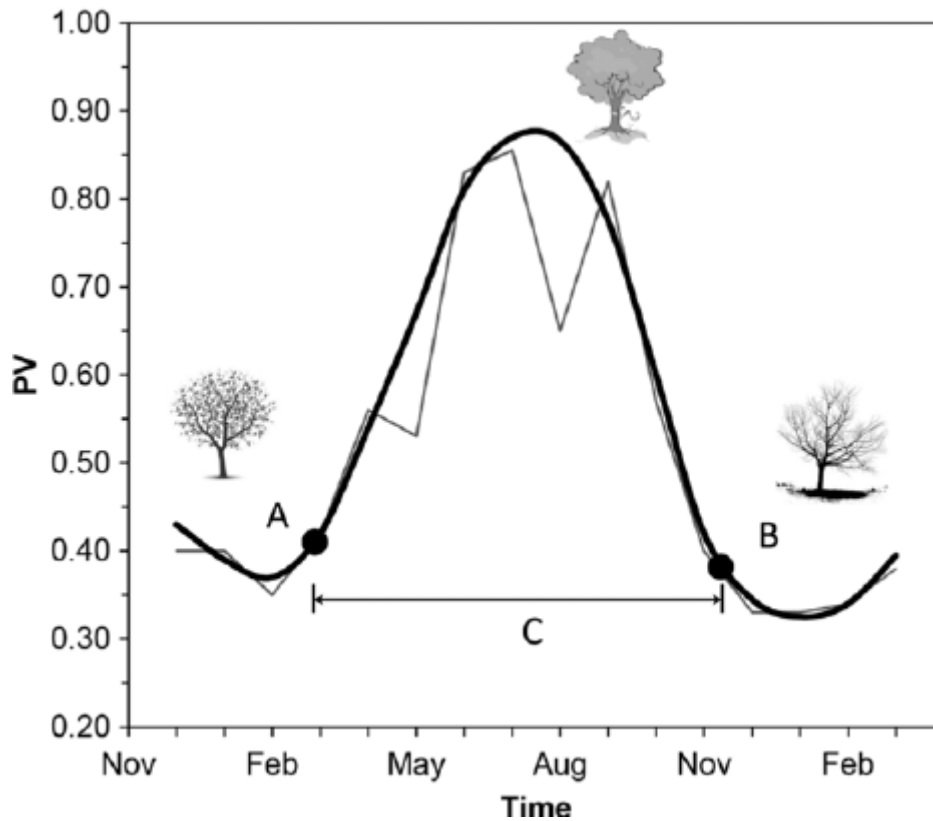
Annex - Table V. Filtered RVI products - 2017..... XI

Annex - Table VI. Unfiltered RVI products – 2018..... XIII

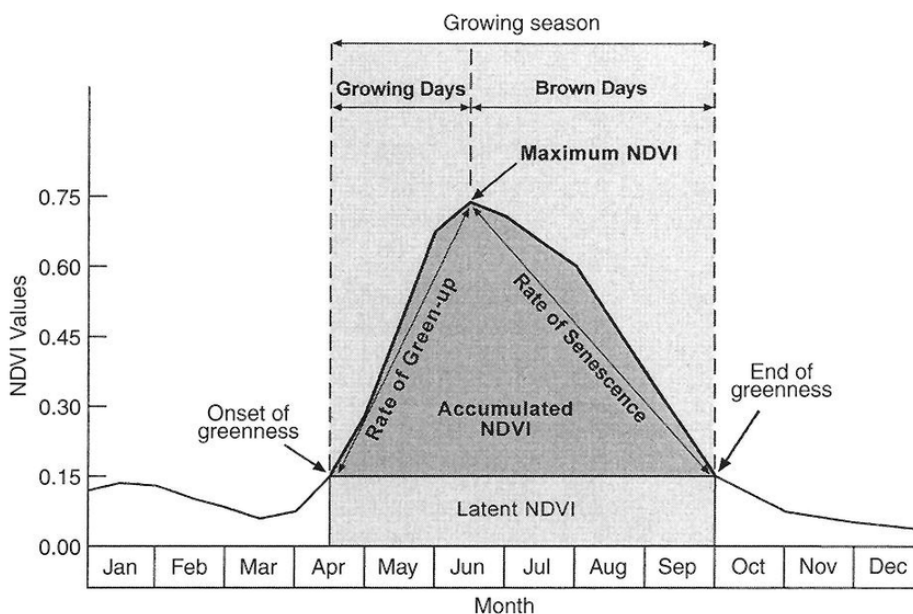
Annex - Table VII. Filtered RVI products – 2018 XV

Annex - Table VIII. Unfiltered RVI products – 2019 XVII

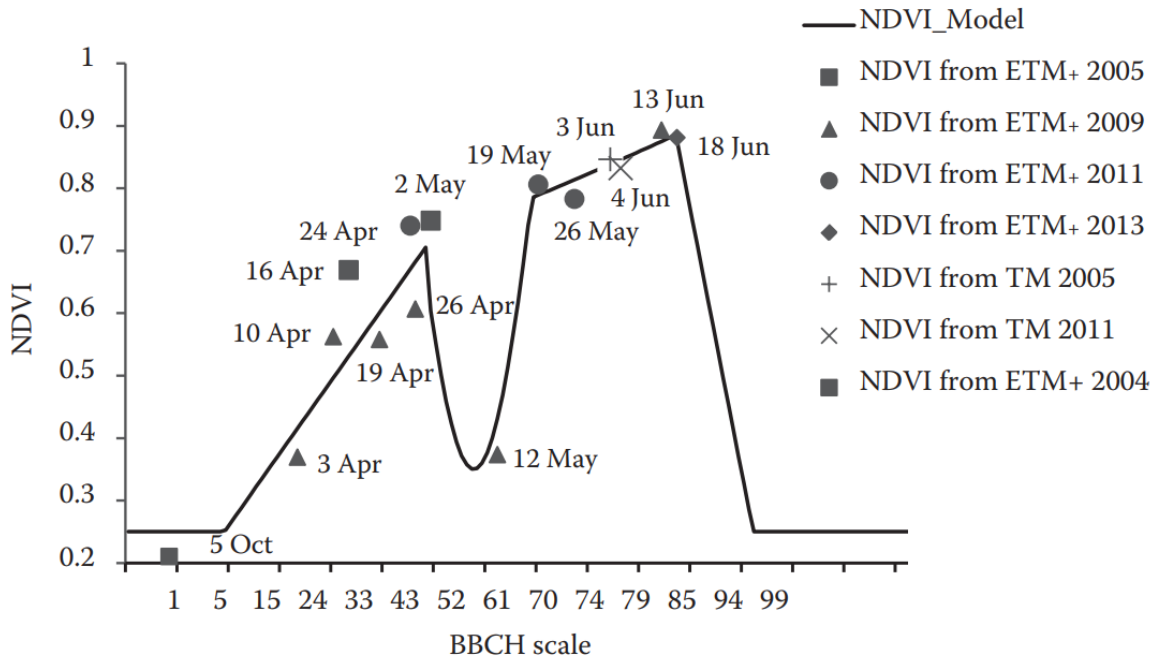
Annex - Table IX. Filtered RVI products – 2019..... XIX



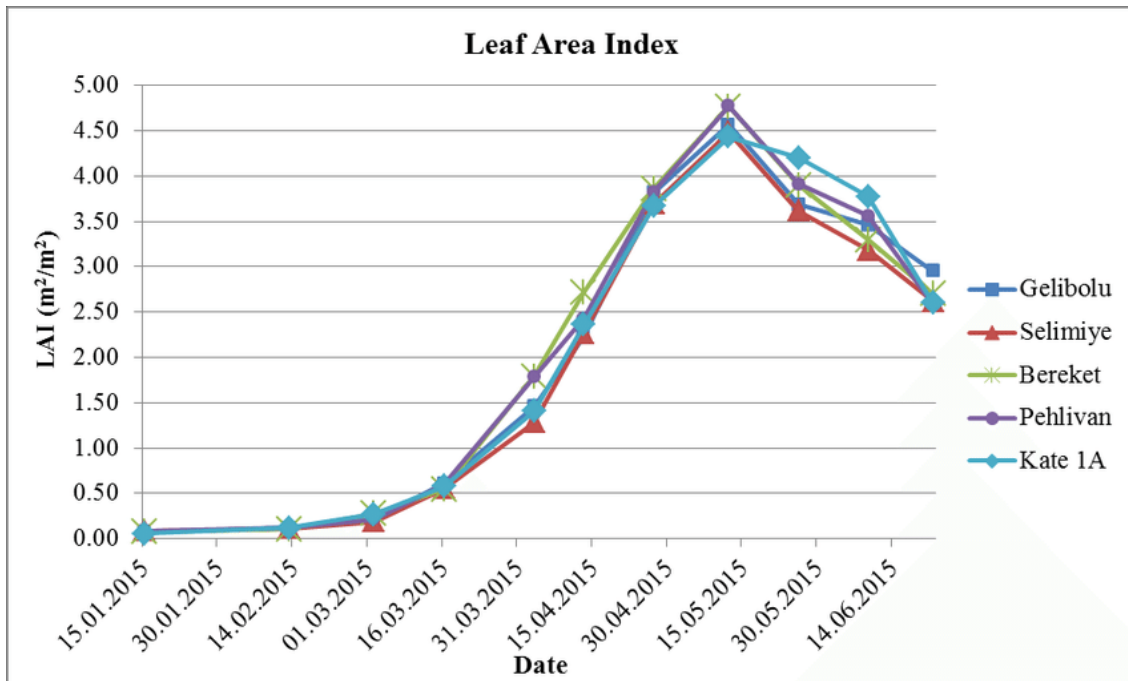
Annex - Fig. I. Phenological metrics derived from a smoothed curve (dark thick curve) of a timeseries of photosynthetically active vegetation (PV) cover fractions (irregular gray line).
 (Source: Chang et al. 2013)



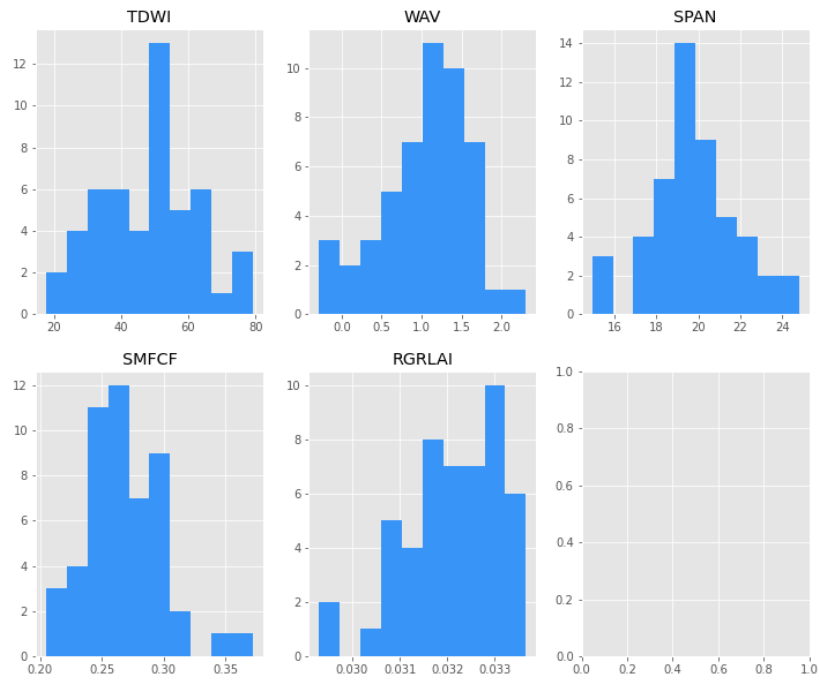
Annex - Fig. II. Vegetation phenology curve and metrics derived from enhanced AVHRR imagery. (Source: Griffith et al. 2002)



Annex - Fig. III. Graph of normalized difference vegetation index (NDVI) and BBCH scale dependency in the case of winter wheat. (Source: Domínguez et al. 2015)



Annex - Fig. IV. Leaf Area Index measurements of winter wheat. (Source: Yesilkoy et al. 2015)



Annex - Fig. V. Five initial variables and parameters for Ensemble model treated as Gaussian random variables with a mean equal to a calibrated value; TDWI - The initial total crop dry weight, WAV - initial soil water content, SPAN - life span of leaves growing at 35 Celsius, RGRLAI - maximum relative increase in LAI, SMFCF - the field capacity of the soil.

Annex - Table I. Leaf Area Index results of wheat fields – descriptive statistics.

date	Mean	Max	Min	Median	St_dev
2016-03-17	0.70	2.01	0.26	0.67	0.23
2016-03-27	0.91	2.52	0.21	0.85	0.28
2016-05-23	5.35	6.79	0.07	5.37	0.68
2017-04-01	0.75	2.88	0.15	0.64	0.45
2017-05-11	3.63	6.04	0.20	4.02	1.28
2017-05-18	4.69	7.15	0.00	5.10	1.49
2017-05-28	5.50	6.94	0.26	5.69	0.88
2017-06-20	4.00	7.03	0.33	4.26	0.93
2018-05-13	4.62	6.14	0.00	4.77	0.75
2018-05-31	3.60	5.56	0.53	3.76	0.87
2019-04-01	2.34	4.55	0.19	2.43	0.99
2019-04-16	3.34	5.11	0.29	3.58	1.10
2019-04-21	3.54	5.40	0.24	3.87	1.13
2019-05-01	3.96	6.17	0.24	4.24	1.16
2019-05-31	3.93	5.45	0.30	4.02	0.58
2019-06-12	3.91	5.31	0.63	4.04	0.77
2019-06-30	1.80	4.54	0.31	1.73	0.45
2019-07-25	0.30	3.82	0.19	0.25	0.18

Annex - Table II. Unfiltered RVI products - 2016

date	Mean	Max	Min	Median	St_dev
2016-03-01	0.39	1.66	0.02	0.38	0.15
2016-03-06	0.39	1.80	0.00	0.39	0.15
2016-03-09	0.32	1.66	0.08	0.31	0.11
2016-03-13	0.31	2.48	0.01	0.30	0.12
2016-03-18	0.32	1.31	0.01	0.31	0.12
2016-03-21	0.35	1.20	0.08	0.33	0.12
2016-03-25	0.31	1.44	0.02	0.29	0.12
2016-03-30	0.41	1.25	0.01	0.40	0.15
2016-04-02	0.41	2.36	0.08	0.39	0.14
2016-04-06	0.44	1.29	0.11	0.41	0.16
2016-04-11	0.50	1.68	0.01	0.50	0.18
2016-04-14	0.64	2.24	0.07	0.62	0.18
2016-04-18	0.74	1.72	0.09	0.72	0.20
2016-04-23	0.83	1.81	0.15	0.82	0.23
2016-04-26	0.82	1.76	0.10	0.81	0.21
2016-04-30	0.67	1.52	0.14	0.65	0.18
2016-05-05	1.06	2.13	0.16	1.05	0.23
2016-05-08	1.04	2.06	0.15	1.02	0.27
2016-05-12	0.62	1.81	0.15	0.59	0.19
2016-05-17	1.09	2.38	0.28	1.05	0.34
2016-05-20	0.91	2.75	0.20	0.87	0.31
2016-05-24	0.71	2.21	0.17	0.69	0.25
2016-05-29	0.91	2.01	0.19	0.89	0.24
2016-06-01	0.82	2.19	0.12	0.77	0.29
2016-06-05	0.67	1.71	0.21	0.66	0.16
2016-06-10	0.86	1.77	0.28	0.83	0.21
2016-06-13	0.71	1.96	0.08	0.68	0.24
2016-06-29	0.63	1.49	0.15	0.61	0.18
2016-07-04	1.00	2.15	0.36	0.98	0.20
2016-07-07	0.95	1.97	0.38	0.93	0.21
2016-07-11	0.75	1.60	0.22	0.73	0.20
2016-07-16	1.07	1.93	0.23	1.07	0.21
2016-07-19	1.09	2.55	0.20	1.08	0.24
2016-07-23	0.81	1.77	0.17	0.80	0.22
2016-07-28	0.86	2.53	0.29	0.85	0.19
2016-07-31	1.05	2.63	0.20	1.04	0.21

Annex - Table III. Filtered RVI products - 2016

date	Mean	Max	Min	Median	St_dev
2016-03-01	0.40	1.56	-0.02	0.40	0.15
2016-03-06	0.37	1.30	-0.01	0.36	0.12
2016-03-09	0.34	1.44	0.02	0.34	0.11
2016-03-13	0.33	1.38	0.06	0.33	0.10
2016-03-18	0.32	1.23	0.06	0.32	0.10
2016-03-21	0.32	1.06	0.06	0.32	0.10
2016-03-25	0.34	1.16	0.08	0.33	0.10
2016-03-30	0.37	1.22	0.10	0.36	0.11
2016-04-02	0.41	1.22	0.07	0.40	0.12
2016-04-06	0.47	1.18	0.07	0.46	0.13
2016-04-11	0.54	1.11	0.10	0.54	0.14
2016-04-14	0.62	1.14	0.17	0.62	0.13
2016-04-18	0.69	1.15	0.21	0.70	0.13
2016-04-23	0.77	1.14	0.21	0.77	0.13
2016-04-26	0.83	1.25	0.20	0.83	0.12
2016-04-30	0.88	1.34	0.22	0.87	0.13
2016-05-05	0.91	1.38	0.28	0.90	0.14
2016-05-08	0.92	1.45	0.33	0.91	0.17
2016-05-12	0.92	1.54	0.37	0.92	0.20
2016-05-17	0.91	1.55	0.39	0.90	0.22
2016-05-20	0.88	1.48	0.42	0.86	0.21
2016-05-24	0.84	1.40	0.38	0.82	0.19
2016-05-29	0.79	1.40	0.38	0.78	0.16
2016-06-01	0.76	1.36	0.41	0.75	0.13
2016-06-05	0.74	1.39	0.44	0.74	0.10
2016-06-10	0.74	1.42	0.43	0.74	0.10
2016-06-13	0.77	1.40	0.44	0.76	0.11
2016-06-29	0.81	1.31	0.47	0.80	0.12
2016-07-04	0.86	1.28	0.53	0.86	0.13
2016-07-07	0.91	1.35	0.57	0.91	0.12
2016-07-11	0.95	1.42	0.54	0.94	0.12
2016-07-16	0.96	1.49	0.51	0.96	0.12
2016-07-19	0.94	1.48	0.44	0.95	0.14
2016-07-23	0.91	1.51	0.40	0.92	0.15
2016-07-28	0.91	1.67	0.45	0.91	0.14
2016-07-31	1.02	2.52	0.31	1.01	0.20

Annex - Table IV. Unfiltered RVI products - 2017

date	Mean	Max	Min	Median	St_dev
2017-03-01	0.31	1.06	0.02	0.30	0.13
2017-03-02	0.30	1.58	0.03	0.29	0.11
2017-03-04	0.28	1.95	0.05	0.26	0.11
2017-03-07	0.34	1.29	0.02	0.32	0.14
2017-03-08	0.23	1.31	0.02	0.21	0.10
2017-03-10	0.34	1.95	0.08	0.33	0.11
2017-03-13	0.28	1.95	0.01	0.27	0.13
2017-03-14	0.24	1.57	0.02	0.21	0.10
2017-03-16	0.27	2.18	0.05	0.25	0.11
2017-03-19	0.32	1.93	0.02	0.31	0.13
2017-03-20	0.30	1.32	0.01	0.28	0.12
2017-03-22	0.33	1.77	0.07	0.32	0.10
2017-03-25	0.33	1.43	0.02	0.32	0.13
2017-03-26	0.27	1.69	0.03	0.25	0.11
2017-03-28	0.34	1.94	0.06	0.32	0.12
2017-03-31	0.40	1.43	0.04	0.39	0.15
2017-04-01	0.35	1.86	0.03	0.34	0.13
2017-04-03	0.49	1.92	0.05	0.48	0.16
2017-04-06	0.43	1.69	0.01	0.41	0.17
2017-04-07	0.51	1.47	0.05	0.50	0.16
2017-04-09	0.48	1.74	0.04	0.46	0.17
2017-04-12	0.46	1.34	0.01	0.45	0.17
2017-04-13	0.55	1.66	0.06	0.55	0.20
2017-04-15	0.60	1.76	0.06	0.60	0.19
2017-04-18	0.62	1.66	0.02	0.62	0.22
2017-04-19	0.51	1.63	0.06	0.51	0.19
2017-04-21	0.60	2.03	0.07	0.60	0.21
2017-04-24	0.57	1.50	0.04	0.56	0.20
2017-04-25	0.53	1.83	0.07	0.52	0.17
2017-04-27	0.72	1.98	0.10	0.72	0.21
2017-04-30	0.62	1.61	0.01	0.63	0.22
2017-05-01	0.65	2.02	0.07	0.66	0.22
2017-05-03	0.75	2.24	0.07	0.76	0.26
2017-05-06	0.86	1.95	0.02	0.90	0.27
2017-05-07	0.72	1.81	0.12	0.72	0.23
2017-05-09	0.93	1.85	0.12	0.95	0.29
2017-05-12	0.88	2.05	0.06	0.89	0.28
2017-05-13	0.79	1.91	0.15	0.79	0.22
2017-05-15	0.94	2.54	0.16	0.93	0.24
2017-05-18	0.90	1.73	0.06	0.89	0.21
2017-05-19	0.68	1.85	0.15	0.64	0.20
2017-05-21	0.86	1.86	0.26	0.84	0.23
2017-05-24	0.82	1.87	0.04	0.80	0.23

Table IV. (continued)

date	Mean	Max	Min	Median	St_dev
2017-05-25	0.70	1.97	0.01	0.67	0.24
2017-05-27	0.81	1.94	0.20	0.78	0.25
2017-05-30	0.88	1.99	0.10	0.85	0.25
2017-05-31	0.65	1.43	0.05	0.63	0.18
2017-06-02	0.81	1.94	0.26	0.79	0.21
2017-06-05	0.79	2.03	0.09	0.76	0.22
2017-06-06	0.64	1.80	0.21	0.62	0.19
2017-06-08	0.74	1.99	0.27	0.71	0.20
2017-06-11	0.94	1.89	0.07	0.93	0.20
2017-06-12	0.67	2.53	0.19	0.64	0.19
2017-06-14	0.83	2.11	0.25	0.81	0.21
2017-06-17	0.92	1.81	0.08	0.91	0.20
2017-06-18	0.77	1.73	0.07	0.77	0.22
2017-06-20	0.86	1.90	0.23	0.85	0.21
2017-06-23	1.00	1.80	0.14	1.00	0.18
2017-06-24	0.75	1.64	0.21	0.75	0.22
2017-06-26	0.89	1.65	0.33	0.88	0.18
2017-06-29	1.00	1.82	0.34	0.99	0.20
2017-06-30	0.80	1.53	0.29	0.79	0.17
2017-07-02	0.87	1.86	0.23	0.86	0.20
2017-07-05	0.95	1.74	0.38	0.94	0.17
2017-07-06	0.82	2.35	0.22	0.82	0.19
2017-07-08	0.95	1.65	0.33	0.94	0.18
2017-07-11	1.05	1.91	0.27	1.04	0.19
2017-07-12	0.87	2.26	0.33	0.86	0.18
2017-07-17	1.00	1.95	0.33	0.98	0.19
2017-07-20	0.86	1.64	0.26	0.86	0.18
2017-07-23	1.04	2.29	0.24	1.03	0.19
2017-07-24	0.82	2.59	0.26	0.81	0.16
2017-07-26	0.84	1.77	0.28	0.82	0.22
2017-07-29	0.70	1.55	0.15	0.69	0.18
2017-07-30	0.59	1.78	0.16	0.57	0.17

Annex - Table V. Filtered RVI products - 2017

date	Mean	Max	Min	Median	St_dev
2017-03-01	0.31	1.06	0.02	0.30	0.13
2017-03-02	0.30	1.01	0.07	0.29	0.10
2017-03-04	0.30	1.14	0.08	0.29	0.10
2017-03-07	0.29	1.03	0.08	0.28	0.09
2017-03-08	0.29	0.98	0.07	0.28	0.09
2017-03-10	0.29	1.02	0.08	0.28	0.09
2017-03-13	0.28	1.02	0.08	0.28	0.09
2017-03-14	0.28	0.98	0.08	0.28	0.09
2017-03-16	0.28	0.94	0.08	0.27	0.09
2017-03-19	0.29	1.00	0.08	0.28	0.09
2017-03-20	0.29	1.06	0.09	0.28	0.09
2017-03-22	0.30	1.07	0.09	0.29	0.09
2017-03-25	0.31	1.01	0.09	0.31	0.09
2017-03-26	0.33	0.94	0.10	0.33	0.09
2017-03-28	0.35	0.97	0.10	0.35	0.10
2017-03-31	0.37	0.96	0.10	0.37	0.10
2017-04-01	0.40	0.98	0.11	0.39	0.11
2017-04-03	0.42	1.05	0.11	0.42	0.12
2017-04-06	0.44	1.12	0.11	0.44	0.12
2017-04-07	0.48	1.18	0.12	0.49	0.14
2017-04-09	0.50	1.17	0.12	0.52	0.15
2017-04-12	0.53	1.18	0.14	0.55	0.15
2017-04-13	0.55	1.13	0.16	0.57	0.16
2017-04-15	0.55	1.08	0.15	0.58	0.16
2017-04-18	0.55	1.13	0.15	0.57	0.16
2017-04-19	0.57	1.14	0.18	0.58	0.16
2017-04-21	0.57	1.18	0.16	0.58	0.16
2017-04-24	0.58	1.18	0.16	0.59	0.16
2017-04-25	0.60	1.19	0.18	0.62	0.16
2017-04-27	0.62	1.15	0.19	0.64	0.17
2017-04-30	0.65	1.10	0.18	0.67	0.17
2017-05-01	0.70	1.12	0.16	0.73	0.19
2017-05-03	0.74	1.17	0.14	0.78	0.20
2017-05-06	0.79	1.22	0.15	0.83	0.21
2017-05-07	0.83	1.29	0.13	0.88	0.21
2017-05-09	0.87	1.34	0.18	0.91	0.20
2017-05-12	0.86	1.31	0.27	0.89	0.18
2017-05-13	0.87	1.30	0.28	0.88	0.17
2017-05-15	0.86	1.35	0.23	0.86	0.16
2017-05-18	0.84	1.36	0.23	0.84	0.15
2017-05-19	0.83	1.39	0.21	0.82	0.15
2017-05-21	0.81	1.44	0.19	0.80	0.16
2017-05-24	0.79	1.42	0.23	0.78	0.17

Table V. (continued)

Date	Mean	Max	Min	Median	St_dev
2017-05-25	0.78	1.42	0.21	0.77	0.17
2017-05-27	0.77	1.41	0.20	0.77	0.17
2017-05-30	0.76	1.40	0.22	0.76	0.17
2017-05-31	0.76	1.43	0.22	0.76	0.15
2017-06-02	0.76	1.40	0.25	0.75	0.14
2017-06-05	0.75	1.33	0.27	0.75	0.13
2017-06-06	0.76	1.28	0.27	0.75	0.12
2017-06-08	0.76	1.31	0.26	0.75	0.12
2017-06-11	0.77	1.39	0.26	0.76	0.12
2017-06-12	0.79	1.41	0.23	0.79	0.11
2017-06-14	0.81	1.37	0.25	0.81	0.12
2017-06-17	0.85	1.36	0.25	0.86	0.12
2017-06-18	0.86	1.29	0.25	0.87	0.12
2017-06-20	0.87	1.25	0.29	0.88	0.13
2017-06-23	0.88	1.33	0.36	0.89	0.13
2017-06-24	0.88	1.31	0.41	0.90	0.13
2017-06-26	0.89	1.28	0.46	0.90	0.12
2017-06-29	0.89	1.28	0.49	0.89	0.11
2017-06-30	0.89	1.24	0.51	0.89	0.10
2017-07-02	0.89	1.25	0.53	0.89	0.10
2017-07-05	0.90	1.33	0.55	0.90	0.10
2017-07-06	0.91	1.38	0.57	0.90	0.09
2017-07-08	0.92	1.43	0.58	0.92	0.09
2017-07-11	0.94	1.48	0.60	0.94	0.09
2017-07-12	0.95	1.49	0.63	0.95	0.09
2017-07-17	0.96	1.44	0.55	0.96	0.10
2017-07-20	0.96	1.46	0.47	0.96	0.10
2017-07-23	0.93	1.40	0.41	0.93	0.11
2017-07-24	0.88	1.31	0.38	0.88	0.13
2017-07-26	0.81	1.31	0.30	0.80	0.15
2017-07-29	0.70	1.35	0.22	0.70	0.15
2017-07-30	0.59	1.74	0.18	0.58	0.17

Annex - Table VI. Unfiltered RVI products – 2018

date	Mean	Max	Min	Median	St_dev
2018-03-02	0.25	1.01	0.01	0.24	0.11
2018-03-03	0.25	1.41	0.04	0.24	0.07
2018-03-05	0.28	1.21	0.08	0.26	0.10
2018-03-08	0.32	1.70	0.02	0.30	0.15
2018-03-09	0.26	1.57	0.00	0.24	0.11
2018-03-14	0.22	1.18	0.00	0.21	0.12
2018-03-17	0.24	1.38	0.05	0.23	0.09
2018-03-20	0.27	1.45	0.02	0.26	0.11
2018-03-21	0.28	0.91	0.02	0.27	0.09
2018-03-23	0.27	1.21	0.09	0.26	0.10
2018-03-26	0.22	1.08	0.01	0.21	0.11
2018-03-27	0.28	1.91	0.01	0.26	0.12
2018-03-29	0.25	1.14	0.04	0.23	0.10
2018-04-01	0.28	1.14	0.01	0.26	0.13
2018-04-02	0.30	1.48	0.01	0.28	0.10
2018-04-04	0.43	1.55	0.16	0.42	0.13
2018-04-07	0.25	1.25	0.01	0.24	0.13
2018-04-08	0.49	1.88	0.01	0.47	0.16
2018-04-10	0.45	1.53	0.17	0.43	0.12
2018-04-13	0.40	1.64	0.01	0.38	0.17
2018-04-14	0.41	1.31	0.02	0.39	0.14
2018-04-16	0.57	2.03	0.13	0.56	0.15
2018-04-19	0.46	1.84	0.01	0.44	0.18
2018-04-20	0.52	1.43	0.01	0.50	0.14
2018-04-22	0.66	1.70	0.25	0.64	0.17
2018-04-25	0.71	1.94	0.01	0.71	0.19
2018-04-26	0.59	1.35	0.01	0.57	0.15
2018-04-28	0.61	1.55	0.22	0.59	0.15
2018-05-01	0.66	1.67	0.05	0.65	0.18
2018-05-02	0.65	1.37	0.01	0.64	0.15
2018-05-04	0.66	1.58	0.23	0.64	0.17
2018-05-07	0.74	2.15	0.05	0.73	0.18
2018-05-08	0.57	1.35	0.05	0.56	0.15
2018-05-10	0.70	1.73	0.23	0.68	0.16
2018-05-13	0.79	1.64	0.04	0.78	0.19
2018-05-14	0.77	1.85	0.02	0.76	0.21
2018-05-16	0.90	1.94	0.21	0.88	0.22
2018-05-19	1.00	2.05	0.04	1.00	0.24
2018-05-20	0.85	2.02	0.08	0.83	0.22
2018-05-22	1.01	2.23	0.25	1.00	0.23
2018-05-25	1.00	2.31	0.07	0.98	0.23
2018-05-26	0.85	1.82	0.04	0.83	0.19
2018-05-28	0.81	1.83	0.30	0.77	0.21

Table VI. (continued)

date	Mean	Max	Min	Median	St_dev
2018-05-31	0.97	2.33	0.05	0.95	0.23
2018-06-01	0.70	1.77	0.03	0.68	0.18
2018-06-03	0.84	1.74	0.25	0.82	0.19
2018-06-06	0.87	1.95	0.09	0.85	0.22
2018-06-07	0.69	1.68	0.04	0.68	0.17
2018-06-09	0.74	1.77	0.27	0.72	0.19
2018-06-12	1.00	2.06	0.14	0.99	0.23
2018-06-13	0.77	1.90	0.04	0.74	0.22
2018-06-15	0.80	1.63	0.32	0.79	0.18
2018-06-18	0.81	1.81	0.10	0.80	0.19
2018-06-19	0.64	1.63	0.06	0.62	0.15
2018-06-21	0.74	1.64	0.25	0.73	0.18
2018-06-24	0.99	1.89	0.18	0.99	0.20
2018-06-25	0.73	1.64	0.14	0.71	0.19
2018-06-27	0.92	1.79	0.17	0.91	0.21
2018-06-30	0.84	1.70	0.05	0.84	0.24
2018-06-30	0.84	1.69	0.05	0.85	0.24
2018-07-01	0.70	1.99	0.08	0.69	0.18
2018-07-03	0.64	1.48	0.14	0.62	0.17
2018-07-07	0.58	1.39	0.17	0.57	0.13
2018-07-09	0.60	1.48	0.26	0.57	0.14
2018-07-12	0.49	1.32	0.08	0.47	0.18
2018-07-15	0.44	1.32	0.20	0.42	0.11
2018-07-18	0.36	1.28	0.03	0.33	0.16
2018-07-21	0.45	1.44	0.14	0.43	0.12
2018-07-24	0.32	1.29	0.03	0.30	0.14
2018-07-25	0.60	1.69	0.10	0.58	0.19
2018-07-27	0.34	1.50	0.12	0.32	0.12
2018-07-30	0.31	1.18	0.03	0.29	0.14
2018-07-31	0.52	1.41	0.06	0.49	0.19

Annex - Table VII. Filtered RVI products – 2018

date	Mean	Max	Min	Median	St_dev
2018-03-02	0.26	0.80	0.04	0.25	0.09
2018-03-03	0.26	0.88	0.08	0.24	0.09
2018-03-05	0.26	0.89	0.07	0.25	0.09
2018-03-08	0.27	0.93	0.09	0.26	0.09
2018-03-09	0.27	0.88	0.11	0.26	0.08
2018-03-14	0.27	0.83	0.08	0.26	0.08
2018-03-17	0.27	0.85	0.06	0.26	0.08
2018-03-20	0.26	0.84	0.06	0.25	0.08
2018-03-21	0.26	0.82	0.06	0.25	0.07
2018-03-23	0.25	0.79	0.08	0.24	0.08
2018-03-26	0.25	0.75	0.08	0.24	0.08
2018-03-27	0.26	0.75	0.09	0.24	0.08
2018-03-29	0.27	0.79	0.09	0.25	0.09
2018-04-01	0.28	0.83	0.10	0.27	0.09
2018-04-02	0.31	0.88	0.12	0.29	0.09
2018-04-04	0.33	0.92	0.14	0.32	0.09
2018-04-07	0.36	0.96	0.16	0.35	0.09
2018-04-08	0.39	0.99	0.17	0.39	0.09
2018-04-10	0.43	1.01	0.16	0.42	0.09
2018-04-13	0.46	1.01	0.15	0.46	0.09
2018-04-14	0.49	1.01	0.15	0.49	0.09
2018-04-16	0.52	1.00	0.15	0.52	0.10
2018-04-19	0.54	1.05	0.15	0.54	0.10
2018-04-20	0.57	1.13	0.16	0.57	0.10
2018-04-22	0.59	1.20	0.15	0.59	0.09
2018-04-25	0.60	1.29	0.13	0.60	0.09
2018-04-26	0.61	1.32	0.15	0.61	0.09
2018-04-28	0.62	1.32	0.13	0.62	0.09
2018-05-01	0.62	1.28	0.16	0.62	0.08
2018-05-02	0.64	1.21	0.19	0.64	0.08
2018-05-04	0.66	1.13	0.20	0.66	0.08
2018-05-07	0.69	1.07	0.24	0.68	0.08
2018-05-08	0.72	1.06	0.26	0.72	0.09
2018-05-10	0.76	1.11	0.30	0.76	0.10
2018-05-13	0.79	1.14	0.33	0.78	0.10
2018-05-14	0.82	1.18	0.34	0.82	0.11
2018-05-16	0.85	1.20	0.33	0.85	0.11
2018-05-19	0.88	1.23	0.35	0.88	0.11
2018-05-20	0.89	1.23	0.34	0.89	0.11
2018-05-22	0.92	1.28	0.32	0.91	0.11
2018-05-25	0.92	1.30	0.31	0.92	0.10
2018-05-26	0.92	1.31	0.29	0.92	0.10
2018-05-28	0.90	1.30	0.28	0.90	0.10

Table VII. (continued)

date	Mean	Max	Min	Median	St_dev
2018-05-31	0.88	1.25	0.30	0.88	0.10
2018-06-01	0.85	1.20	0.29	0.85	0.10
2018-06-03	0.82	1.22	0.32	0.82	0.10
2018-06-06	0.80	1.24	0.35	0.80	0.11
2018-06-07	0.79	1.24	0.36	0.78	0.11
2018-06-09	0.76	1.22	0.37	0.75	0.12
2018-06-12	0.76	1.20	0.38	0.75	0.12
2018-06-13	0.78	1.24	0.34	0.77	0.12
2018-06-15	0.80	1.24	0.35	0.79	0.11
2018-06-18	0.81	1.23	0.37	0.80	0.11
2018-06-19	0.83	1.31	0.33	0.83	0.10
2018-06-21	0.84	1.34	0.33	0.84	0.10
2018-06-24	0.84	1.34	0.31	0.84	0.11
2018-06-25	0.84	1.34	0.25	0.84	0.11
2018-06-27	0.82	1.30	0.26	0.83	0.11
2018-06-30	0.79	1.23	0.30	0.80	0.12
2018-06-30	0.77	1.15	0.27	0.78	0.11
2018-07-01	0.72	1.08	0.30	0.73	0.11
2018-07-03	0.67	1.04	0.35	0.67	0.11
2018-07-07	0.62	1.04	0.33	0.62	0.10
2018-07-09	0.56	1.01	0.30	0.56	0.09
2018-07-12	0.51	1.01	0.27	0.51	0.09
2018-07-15	0.47	1.00	0.24	0.47	0.09
2018-07-18	0.44	0.99	0.23	0.43	0.09
2018-07-21	0.42	0.98	0.22	0.41	0.09
2018-07-24	0.41	0.96	0.20	0.39	0.09
2018-07-25	0.41	0.94	0.20	0.39	0.09
2018-07-27	0.41	0.93	0.20	0.40	0.09
2018-07-30	0.43	0.90	0.20	0.42	0.09
2018-07-31	0.45	0.89	0.21	0.44	0.09

Annex - Table VIII. Unfiltered RVI products – 2019

date	Mean	Max	Min	Median	St_dev
2019-03-03	0.46	1.83	0.01	0.46	0.22
2019-03-04	0.32	1.14	0.02	0.30	0.14
2019-03-06	0.34	1.16	0.08	0.32	0.13
2019-03-09	0.37	1.79	0.01	0.35	0.15
2019-03-10	0.34	1.49	0.02	0.32	0.13
2019-03-12	0.34	2.18	0.04	0.32	0.14
2019-03-15	0.46	1.70	0.02	0.45	0.17
2019-03-16	0.36	1.19	0.05	0.34	0.15
2019-03-18	0.34	1.19	0.06	0.32	0.14
2019-03-21	0.27	1.33	0.01	0.26	0.10
2019-03-22	0.35	1.39	0.05	0.34	0.10
2019-03-24	0.43	1.69	0.08	0.41	0.16
2019-03-27	0.44	1.75	0.04	0.43	0.16
2019-03-28	0.52	1.33	0.08	0.51	0.19
2019-03-30	0.46	1.56	0.11	0.45	0.16
2019-04-02	0.43	2.22	0.05	0.41	0.14
2019-04-03	0.48	1.79	0.07	0.47	0.13
2019-04-05	0.57	1.50	0.18	0.56	0.18
2019-04-08	0.62	1.37	0.06	0.60	0.18
2019-04-09	0.51	1.57	0.01	0.49	0.15
2019-04-11	0.57	1.38	0.01	0.54	0.18
2019-04-14	0.74	1.61	0.04	0.73	0.19
2019-04-15	0.66	2.18	0.15	0.62	0.25
2019-04-17	0.64	1.70	0.12	0.61	0.20
2019-04-20	0.68	1.59	0.08	0.67	0.18
2019-04-21	0.64	1.73	0.15	0.61	0.18
2019-04-23	0.73	2.04	0.19	0.72	0.20
2019-04-26	0.75	2.24	0.14	0.74	0.19
2019-04-27	0.83	2.07	0.27	0.81	0.22
2019-04-29	0.79	1.88	0.10	0.78	0.19
2019-05-02	0.83	2.11	0.06	0.82	0.21
2019-05-03	0.79	1.92	0.06	0.77	0.20
2019-05-05	0.84	1.77	0.16	0.82	0.22
2019-05-08	0.90	2.00	0.06	0.88	0.25
2019-05-09	0.85	2.33	0.07	0.82	0.24
2019-05-11	1.03	2.27	0.19	1.01	0.28
2019-05-14	1.01	2.19	0.06	1.00	0.26
2019-05-15	1.03	2.35	0.16	1.00	0.31
2019-05-17	1.06	2.35	0.27	1.04	0.29
2019-05-20	1.05	2.21	0.01	1.03	0.27
2019-05-21	1.02	2.40	0.17	0.94	0.37
2019-05-23	1.02	2.16	0.17	1.01	0.29
2019-05-26	1.09	2.20	0.19	1.09	0.29

Table VIII. (continued)

date	Mean	Max	Min	Median	St_dev
2019-05-27	1.16	2.46	0.18	1.18	0.35
2019-05-29	1.02	2.15	0.25	0.98	0.32
2019-06-01	1.00	2.23	0.19	0.98	0.27
2019-06-02	0.90	2.20	0.14	0.86	0.32
2019-06-04	0.81	1.90	-0.60	0.79	0.20
2019-06-07	0.82	1.97	0.25	0.80	0.20
2019-06-08	0.66	2.10	0.21	0.64	0.18
2019-06-10	0.70	1.86	0.20	0.67	0.17
2019-06-13	0.84	1.80	0.22	0.82	0.20
2019-06-14	0.54	1.53	0.17	0.50	0.17
2019-06-16	0.72	1.67	0.24	0.69	0.20
2019-06-25	0.81	1.68	0.24	0.80	0.18
2019-06-26	0.59	1.79	0.13	0.57	0.16
2019-06-28	0.70	1.68	0.26	0.68	0.17
2019-07-01	0.78	1.65	0.26	0.76	0.18
2019-07-04	0.73	1.74	0.27	0.71	0.19
2019-07-07	0.83	1.90	0.27	0.82	0.20
2019-07-08	0.62	1.63	0.08	0.61	0.16
2019-07-10	0.65	1.83	0.16	0.62	0.19
2019-07-13	0.85	1.62	0.24	0.84	0.19
2019-07-14	0.76	2.14	0.23	0.74	0.18
2019-07-16	0.79	2.10	0.19	0.78	0.22
2019-07-19	0.70	2.32	0.04	0.69	0.19
2019-07-20	0.75	2.01	0.16	0.74	0.18
2019-07-22	0.52	1.50	0.12	0.49	0.17
2019-07-25	0.47	1.58	0.04	0.45	0.15
2019-07-26	0.51	2.08	0.18	0.49	0.13
2019-07-28	0.49	1.57	0.08	0.47	0.13
2019-07-31	0.42	1.67	0.02	0.39	0.16

Annex - Table IX. Filtered RVI products – 2019

date	Mean	Max	Min	Median	St_dev
2019-03-03	0.43	1.56	0.01	0.42	0.20
2019-03-04	0.38	1.13	0.10	0.38	0.13
2019-03-06	0.35	1.09	0.12	0.34	0.12
2019-03-09	0.35	1.04	0.13	0.33	0.11
2019-03-10	0.34	0.93	0.13	0.33	0.11
2019-03-12	0.35	0.93	0.12	0.34	0.11
2019-03-15	0.35	0.91	0.12	0.35	0.11
2019-03-16	0.36	0.87	0.12	0.36	0.11
2019-03-18	0.37	0.83	0.13	0.37	0.11
2019-03-21	0.38	0.81	0.14	0.38	0.11
2019-03-22	0.39	0.81	0.16	0.40	0.11
2019-03-24	0.40	0.86	0.17	0.41	0.10
2019-03-27	0.42	0.89	0.18	0.42	0.10
2019-03-28	0.44	0.92	0.19	0.44	0.11
2019-03-30	0.46	0.95	0.21	0.46	0.11
2019-04-02	0.48	0.97	0.23	0.49	0.11
2019-04-03	0.51	1.01	0.25	0.51	0.11
2019-04-05	0.53	1.05	0.26	0.53	0.12
2019-04-08	0.56	1.07	0.27	0.55	0.12
2019-04-09	0.58	1.08	0.28	0.58	0.13
2019-04-11	0.61	1.07	0.29	0.60	0.13
2019-04-14	0.63	1.06	0.31	0.62	0.13
2019-04-15	0.65	1.07	0.33	0.64	0.13
2019-04-17	0.67	1.12	0.34	0.66	0.12
2019-04-20	0.68	1.14	0.34	0.68	0.12
2019-04-21	0.70	1.17	0.33	0.70	0.11
2019-04-23	0.72	1.17	0.34	0.73	0.11
2019-04-26	0.74	1.15	0.34	0.75	0.12
2019-04-27	0.77	1.19	0.37	0.78	0.12
2019-04-29	0.80	1.21	0.40	0.80	0.12
2019-05-02	0.81	1.21	0.39	0.81	0.12
2019-05-03	0.83	1.25	0.39	0.83	0.12
2019-05-05	0.86	1.30	0.35	0.86	0.13
2019-05-08	0.88	1.33	0.32	0.88	0.14
2019-05-09	0.92	1.39	0.33	0.92	0.15
2019-05-11	0.97	1.50	0.35	0.96	0.17
2019-05-14	1.00	1.59	0.36	0.99	0.19
2019-05-15	1.03	1.65	0.39	1.02	0.21
2019-05-17	1.05	1.66	0.39	1.04	0.22
2019-05-20	1.07	1.70	0.40	1.06	0.23
2019-05-21	1.09	1.72	0.40	1.08	0.24
2019-05-23	1.08	1.68	0.37	1.07	0.24
2019-05-26	1.06	1.65	0.38	1.06	0.23

Table IX. (continued)

date	Mean	Max	Min	Median	St_dev
2019-05-27	1.04	1.59	0.38	1.04	0.22
2019-05-29	1.00	1.52	0.37	1.00	0.20
2019-06-01	0.95	1.40	0.40	0.96	0.17
2019-06-02	0.91	1.29	0.40	0.92	0.14
2019-06-04	0.86	1.27	0.40	0.87	0.12
2019-06-07	0.81	1.21	0.36	0.82	0.10
2019-06-08	0.77	1.22	0.40	0.77	0.09
2019-06-10	0.74	1.23	0.38	0.73	0.09
2019-06-13	0.71	1.23	0.39	0.70	0.10
2019-06-14	0.68	1.23	0.43	0.67	0.10
2019-06-16	0.66	1.18	0.39	0.64	0.11
2019-06-25	0.66	1.15	0.36	0.64	0.10
2019-06-26	0.68	1.14	0.39	0.67	0.10
2019-06-28	0.72	1.13	0.42	0.71	0.09
2019-07-01	0.74	1.11	0.43	0.73	0.08
2019-07-04	0.76	1.15	0.39	0.75	0.08
2019-07-07	0.77	1.14	0.35	0.77	0.09
2019-07-08	0.77	1.18	0.34	0.77	0.09
2019-07-10	0.76	1.18	0.31	0.76	0.09
2019-07-13	0.74	1.18	0.28	0.74	0.10
2019-07-14	0.71	1.16	0.28	0.71	0.10
2019-07-16	0.68	1.18	0.25	0.68	0.10
2019-07-19	0.66	1.18	0.23	0.66	0.09
2019-07-20	0.64	1.18	0.23	0.64	0.09
2019-07-22	0.62	1.15	0.23	0.61	0.08
2019-07-25	0.60	1.09	0.25	0.59	0.08
2019-07-26	0.58	1.15	0.27	0.58	0.08
2019-07-28	0.56	1.19	0.29	0.56	0.08
2019-07-31	0.55	1.21	0.29	0.54	0.08